

MICROWAVE CAVITIES FOR
AXION DARK MATTER DETECTORS

By

IAN P. STERN

A DISSERTATION PRESENTED TO THE GRADUATE SCHOOL
OF THE UNIVERSITY OF FLORIDA IN PARTIAL FULFILLMENT
OF THE REQUIREMENTS FOR THE DEGREE OF
DOCTOR OF PHILOSOPHY

UNIVERSITY OF FLORIDA

2017

© 2017 Ian P. Stern

To Mom-mom and Pop-pop, who were unable to witness this moment in my life

ACKNOWLEDGMENTS

I wish to thank my advisor, Dr. David Tanner, and Dr. Pierre Sikivie and Dr. Neil Sullivan for years of guidance, assistance, teaching, mentoring, and enabling this research to transpire. I thank Dr. Christopher Stanton for being an outside observer and a constant check on the technical worth of my work. I also thank my external committee member, Dr. Carl Crane, for his years of support during my engineering studies and throughout my engineering career leading up to my Ph.D. program; without you, I could have never made the successful leap into physics.

I especially thank Martyna Levay for years of emotional support and dedication, including uncountable hours of proofreading, keeping me focused and on track, helping me with planning and organizing, and putting up with more than she should have had to. I thank my fellow graduate students Manish Amin, Alex Markoff, Nilanjan Banik, and Chad Hopkins for their friendship and assistance with passing my classes.

I would like to thank Dr. Gp Carosi and Dr. Gray Rybka for being role models as superior young scientists, and Dr. Lesley Rosenberg for his leadership on ADMX. I acknowledge my ADMX collaborators Christian Boutan, Jim Sloan, and all the others for assisting me through difficult technical challenges in my investigations. I thank the staff at the University of Florida Department of Physics, especially Marc Link, Bill Malphurs, Pete Axson, Greg Labbe, Clint Collins, Pam Marlin, and Janet Germany, for years of support. I thank Byron Knight for his ongoing mentorship, wisdom, and encouragement.

Finally, I wish to thank my mother for birthing me, feeding me, giving me a home, raising me, nurturing me, encouraging me, and always believing in me. It is without doubt that I could have never accomplished anything without you.

I acknowledge funding support by the U.S. Department of Defense through the National Defense Science and Engineering Graduate Fellowship Program, the National Aeronautics and Space Administration through the Florida Space Research Program, and the Armed Forces Communications and Electronics Association through the Intelligence Studies Scholarship award, as well as the Department of Energy through the Axion Dark Matter eXperiment under Grant No. DE-SC0010280.

TABLE OF CONTENTS

	<u>page</u>
ACKNOWLEDGMENTS.....	4
LIST OF TABLES.....	8
LIST OF FIGURES.....	9
ABSTRACT	14
CHAPTER	
1 INTRODUCTION	16
2 BACKGROUND	20
2.1 Axion Particle	20
2.2 Dark Matter	22
2.3 CDM Axions	31
2.4 Axion Haloscope Detectors	38
3 MICROWAVE CAVITIES FOR AXION HALOSCOPE DETECTORS	50
3.1 Microwave Cavity Theory	50
3.2 Symmetry Breaking.....	61
3.3 Mode Identification Methods	91
3.4 High-Frequency Cavities.....	100
3.5 Superconducting Hybrid Cavities	118
4 12-VANE CAVITY PROTOTYPE	123
4.1 Design.....	123
4.2 Fabrication	134
4.3 Test Apparatus.....	140
4.4 Test Results	146
5 IN-SITU MODE TEST	166
5.1 Test Methods	166
5.2 Test Results	172
6 CONCLUSION.....	185
6.1 Future Work	185
6.2 Summary.....	190
LIST OF REFERENCES	194

BIOGRAPHICAL SKETCH..... 201

LIST OF TABLES

<u>Table</u>		<u>page</u>
3-1	Configuration of cavities with the highest scan rates from the periodic array study.....	115
4-1	Quality factors of the 12-vane prototype for different channels during testing..	164
5-1	Predicted combined power variables of modes shown in Fig. 5-2.....	170
5-2	Results of the empty cavity in-situ mode test.....	175
5-3	Results of the 2-rod cavity in-situ mode test in the minimum TM_{010} frequency configuration.....	179
5-4	Results of the 2-rod cavity in-situ mode test in the maximum TM_{010} frequency configuration.....	181
5-5	Results of the 2-rod cavity in-situ mode test in the mid-range TM_{010} frequency configuration.....	182
5-6	Results of the 12-vane prototype in-situ mode test.....	184

LIST OF FIGURES

<u>Figure</u>	<u>page</u>
2-1 Baryonic matter observed in the coma cluster	23
2-2 Rotation curve of Galaxy M33	23
2-3 Rotation curve of nearby galaxies	24
2-4 Gravitational lensing of the Abell 2218 galaxy cluster	25
2-5 Observations from the Bullet Cluster	26
2-6 Limits on percent of baryons in the universe from nucleosynthesis.....	27
2-7 Cosmic microwave background measurements from Planck	28
2-8 Power spectrum of the cosmic microwave background measurements	28
2-9 Predicted scales of cosmic structure observations using the Λ CDM model	29
2-10 Visualization of current theories of dark matter.....	30
2-11 Feynman Diagram of Axion-photon Interaction	34
2-12 Axion exclusion plot near the CDM axions mass range.....	36
2-13 Local kinetic energy distribution of galactic axions	39
2-14 Schematic of mechanical tuning of haloscope cavities.....	41
2-15 Graphic representation of a haloscope detector using a solenoid magnet and a cylindrical microwave cavity, and an anticipated detection signal of CDM axions	46
2-16 Schematic of ADMX receiver chain and photograph of the inside of the ADMX microwave cavity.....	47
2-17 Axion exclusion plot showing published results of ADMX.....	48
3-1 Cross-sectional images of the E_z field in an empty cylindrical cavity	53
3-2 Cross-sectional images of the E_z field in a cylindrical cavity with a coaxial conducting rod	56
3-3 Cross-sectional images of the E_z field in a cylindrical cavity with a coaxial dielectric rod	57

3-4	Antenna coupled to a cavity through a wall or endplate	59
3-5	Cross-sectional images of the E_z field in a cylindrical cavity with an offset conducting rod	63
3-6	Example of the electric field of the TM_{010} mode inside a tuned cylindrical cavity depicting the curvature of the field.....	63
3-7	Plot of the TM_{010} frequency and form factor as a function of tuning rod displacement for a circular cylindrical cavity	65
3-8	Cross-sectional images of the E_z field for the TM_{010} mode in a cylindrical cavity with multiple conducting rods	66
3-9	Cross-sectional images of the E_z field for the TM_{110} modes in a cylindrical cavity with two conducting rods	68
3-10	Cross-sectional images of the E_z field for higher-order modes in a cylindrical cavity with two conducting rods	68
3-11	Cross-sectional images of the E_z field for modes in a cylindrical cavity with two conducting rods.....	70
3-12	Cross-sectional images of the E_z field in a cylindrical cavity with an offset dielectric rod	70
3-13	Plot of a TM_{010} mode crossing during frequency tuning with a conducting rod for a circular cylindrical cavity	72
3-14	Cross-sectional images of $ \mathbf{E} $ of the TM_{010} mode in a coaxial cavity	74
3-15	Plots of mode repulsion and search mode form factor for a circular cylindrical cavity with a discontinuous conducting tuning rod	76
3-16	Plots showing the hole in the frequency search spectrum produced by longitudinal symmetry breaking	80
3-17	Plot of hole in frequency search spectrum as a function of rod-end gap size	81
3-18	Cross-sectional images of $ \mathbf{E} $ with E vectors of the hybrid modes and the TE_{215} mode at the point of maximum mode repulsion in a cylinder cavity	83
3-19	Plot showing mode crowding due to increased mechanical gap at the rod- ends	85
3-20	Cross-sectional images of $ \mathbf{E} $ of the TM_{010} mode in a tuned cavity with a rod tilt (angular misalignment)	87

3-21	Plots of mode repulsion and search mode form factor for a circular cylindrical cavity with a tilted conducting tuning rod	88
3-22	Plots of frequency and search mode form factor for a circular cylindrical cavity with a conducting tuning rod tilted 1.80°	90
3-23	Example of frequency predictions from ADMX	93
3-24	Example of a TM_{010} mode map from ADMX	95
3-25	Example of a TM_{020} mode map without predictions from ADMX.....	96
3-26	Schematic of bead-pull test and test results from a bead-pull test.....	99
3-27	Plot of frequency range and form factor for a circular cylindrical cavity with a conducting tuning rod at varying diameters	102
3-28	Schematic of a 6-cavity packing	105
3-29	Photograph of the inside of a 2-cell partitioned cavity	106
3-30	Cross-sectional images of the E_z field of the TM_{110} modes in a 8-cell partitioned cylindrical cavity	107
3-31	Plot of effective volume verses TM_{010} frequency for power combined cavities.....	108
3-32	Plot of form factor verses frequency for the three lowest search modes of ADMX	111
3-33	Geometry of example cavities from periodic array study	113
3-34	Cross-sectional images of the E_z field for the TM_{010} mode in periodic arrays ...	114
3-35	Cross-sectional images of the E_z field for the TM_{010} mode in a 19-rod periodic array cavity	117
3-36	Schematic of perpendicular magnetic fields in superconducting hybrid cavities	122
4-1	Schematic of a cross-section through the x - y plane of the 12-vane prototype..	124
4-2	Plot of C_{010} verse f_{010} for the 12-vane cavity	125
4-3	Frequency predictions for the 12-vane prototype from a 2-dimensional analysis	126
4-4	Cross-sectional images of the E_z field for the TM_{010} mode of the 12-vane prototype design with bottom antenna positions overlaid	127

4-5	CAD models of the 12-vane prototype.....	128
4-6	FEMs of the 12-vane prototype	129
4-7	Cross-sectional images of $ \mathbf{E} $ of the TM_{010} mode in 12-vane prototype as resolved by FEM simulation.....	130
4-8	Cross-sectional images of $ \mathbf{E} $ of the TM_{010} mode in the 12-vane prototype as resolved by the complex FEM simulation	131
4-9	Plot of the results from a convergence study for the complex 12-vane FEM model	132
4-10	Frequency predictions for the 12-vane prototype from complex FEM simulations.....	133
4-11	Select views from fabrication drawings of the 12-vane prototype	135
4-12	Plot of a generic electropolishing current density curve.....	136
4-13	Photograph of four vanes partly assembled	137
4-14	Photograph of prototype vanes assembled to the cross bracket and the bottom-plate.....	138
4-15	Photograph of prototype assembly with the top-plate removed	139
4-16	Photograph of 12-vane prototype assembly	140
4-17	Schematic of 12-vane prototype test apparatus	141
4-18	Photograph of the gearbox for the 12-vane prototype	143
4-19	Photograph the 12-vane cavity cryostat insert.....	145
4-20	Photograph the 12-vane cavity test apparatus	146
4-21	Cross-sectional images of the E_z field of the TM_{010} mode in the 4-vane cavity with bottom antenna positions overlaid.....	147
4-22	Power spectrum plots for the 4-vane cavity prototype	148
4-23	Power spectrum plots for the 12-vane prototype at room temperature.....	150
4-24	Mode maps for the 12-vane prototype.....	152
4-25	Mode map for the 12-vane prototype for channels S_{HE} and S_{HF}	153
4-26	Color-plot mode maps for the 12-vane prototype	154

4-27	Plot showing the frequency step size of the 12-vane prototype.....	156
4-28	Power spectrum plots for the 12-vane prototype showing frequency discrepancies of a mode.....	158
4-29	Partial measurement mode map in a LN ₂ bath for the 12-vane prototype	159
4-30	Cryostat level detector reading during a L ⁴ He fill.....	160
4-31	Maximum motor speed of the failing motor as a function of temperature	161
4-32	Analytical predictions for the 12-vane prototype during L ⁴ He testing.....	162
4-33	Partial measurement mode map in a L ⁴ He bath for the 12-vane prototype	163
4-34	Measured Q_L of the 12-vane prototype verses temperature.....	165
5-1	Cross-sectional images of the E_z field for the TM ₀₁₀ mode in cylindrical cavities with various tuning configurations depicting parity symmetries	168
5-2	Cross-sectional images of the E_z field of various modes in cylindrical cavities with two non-symmetric, conducting tuning rods and two antenna locations....	169
5-3	Schematic of in-situ mode test.....	171
5-4	Cross-sectional images of the E_z field in an empty cylindrical cavity depicting the location of the top-plate in-situ mode test antennas	173
5-5	Power spectrum plots for the empty cavity in-situ mode test.....	176
5-6	Cross-sectional images of the E_z field for the TM ₀₁₀ in a cylindrical cavity with two conducting tuning rods in the in-situ test configurations depicting the location of the top-plate antennas.....	177
5-7	Power spectrum plots for the 2-rod cavity in-situ mode test in the minimum TM ₀₁₀ frequency configuration	177
5-8	Cross-sectional images of the E_z field of the TM ₀₂₀ in a cylindrical cavity with two conducting tuning rods in the in-situ test configurations depicting the location of the top-plate antennas.....	178
5-9	Power spectrum plot for the 4-vane cavity in-situ mode test	183

Abstract of Dissertation Presented to the Graduate School
of the University of Florida in Partial Fulfillment of the
Requirements for the Degree of Doctor of Philosophy

MICROWAVE CAVITIES FOR
AXION DARK MATTER DETECTORS

By

Ian P. Stern

December 2017

Chair: David B. Tanner
Major: Physics

Nearly all astrophysical and cosmological data point convincingly to a large component of cold dark matter (CDM) in the Universe. The axion particle, first theorized as a solution to the strong CP (charge conjugation times parity) problem of quantum chromodynamics, has been established as a prominent CDM candidate. Cosmic observation and particle physics experiments have bracketed the unknown mass of such CDM axions between approximately μeV and meV . The Axion Dark Matter eXperiment (ADMX) is a direct-detection CDM axion search which has set limits at the KSVZ coupling of the axion to two photons for axion masses between 1.9 and 3.7 μeV . But most of the viable search-space of axions has yet to be probed.

It is now evident that the current cavity design for ADMX does not provide for successful scanning above $\sim 4 \mu\text{eV}$ ($\sim 1 \text{ GHz}$), and new microwave cavity technologies need to be developed to enable searching for CDM axions of greater mass. A broad study into factors that affect high-frequency microwave cavity was conducted in an effort to expand the capabilities of current haloscope detectors. The study evaluated the effects of symmetry breaking on axion search potential and assessed state-of-the-art cavity technologies relevant to haloscope detectors. Periodic arrays of tuning rods or

vanes were evaluated for increasing the search range of haloscopes, and a prototype haloscope cavity and an in-situ mode identification technique were developed and tested.

The study revealed several significant findings. The cause for holes in the frequency search spectrum at mode crossings is hybridization modes (mode mixing), which occurs due to longitudinal symmetry breaking. Symmetry breaking also results in increased mode crowding, which hinders mode identification and tracking, and further increases mode mixing. Arrays of tuning rods or vanes produce tunable modes, but result in increased sensitivity to symmetry breaking, requiring advanced mode identification techniques and additional studies.

CHAPTER 1 INTRODUCTION

The detection of the axion is of significant interest to particle physics and to cosmology. The axion is a theoretical pseudoscalar particle [1,2] which was originally postulated to explain why P (parity) and CP (charge conjugation times parity) are conserved by the strong interactions [3]. If the axion mass were in the range of $\sim 10^{-6}$ - 10^{-3} eV, the axion would be a natural cold dark matter (CDM) candidate [4]. With recent diminutions of the available parameter space for the weakly interacting massive particle (WIMP) [5], the axion is now the most promising candidate for the constitution of cold dark matter and this has generated a proliferation of searches around the world. String theory further suggests the simultaneous presence of many ultra-light axion-like particles, possibly populating each decade of mass down to the Hubble scale of 10^{-33} eV [6].

Axion detection has proven to be extremely challenging. CDM axions have a lifetime vastly greater than the age of the universe [5], have exceptionally weak interactions with matter and radiation, and were originally thought to be "invisible" to all detection techniques. However, in 1983 Sikivie [7] proposed a method by which these axions plausibly could be detected. He showed the decay rate of axions to photons can be greatly increased within a strong magnetic field, through the inverse Primakoff [8] effect.

The Lagrangian for the axion-photon interaction is given by

$$\mathcal{L}_{a\gamma\gamma} = g_{a\gamma\gamma} a \mathbf{E} \cdot \mathbf{B}, \quad (1-1)$$

where $g_{a\gamma\gamma}$ is the axion-photon coupling constant, proportional to the mass of the axion, a is the axion field, and \mathbf{E} and \mathbf{B} are the electric and magnetic fields of each photon,

respectively. The coupling allows the axion to decay to two photons (see Fig. 2-11). In a static external magnetic field, an axion may convert to a photon whose energy equals the total energy of the axion. The \mathbf{B} in Eq. 1-1 is effectively changed to the static magnetic field, \mathbf{B}_0 . Thus, as the external magnetic field strength is increased, so is the conversion rate of the axion. This process is effective for both relativistic or non-relativistic axions [9].

An axion haloscope detector uses a microwave cavity permeated by a strong magnetic field to convert axions to photons via the inverse Primakoff effect. The axion-photon conversion is resonantly enhanced when the frequency of a cavity mode is $f_{mnp} \approx m_a c^2/h$, where c is the speed of light in vacuum and h is Planck's constant, and the mode sufficiently couples to the axion-photon interaction (see Chapter 2.4). From Eq. 1-1, it can be shown that the coupling strength of a resonant mode to the axion-photon interaction is proportional to $\int d^3x \mathbf{B}_0 \cdot \mathbf{E}_{mnp}(\mathbf{x})$, where \mathbf{E}_{mnp} is the electric field of the mode. The indices \mathbf{m} , \mathbf{n} , and \mathbf{p} identify the various modes.

The power produced in the cavity for a particular mode is given by

$$P_{mnp} \approx g_{a\gamma\gamma}^2 \frac{\rho_a}{m_a} B_0^2 C_{mnp} V Q_L, \quad (1-2)$$

where m_a is the mass of the axion, ρ_a is the local mass density of the axion field, V is the volume of the cavity, and Q_L is the loaded quality factor of the cavity (assumed to be less than the effective Q of the axion signal) [10]. C_{mnp} is the normalized form factor describing the coupling of the axion to a specific mode. It is given by

$$C_{mnp} \equiv \frac{|\int d^3x \mathbf{B}_0 \cdot \mathbf{E}_{mnp}(\mathbf{x})|^2}{B_0^2 V \int d^3x \varepsilon(\mathbf{x}) |\mathbf{E}_{mnp}(\mathbf{x})|^2}, \quad (1-3)$$

where $\varepsilon(\mathbf{x})$ is the permittivity within the cavity normalized to vacuum.

The mass of CDM axions is constrained by cosmological [11-13] and astronomical [14] observations, $\mu\text{eV} \lesssim m_a \lesssim \text{meV}$. Haloscope detectors conduct axion searches by incrementally tuning frequency of a coupling resonant mode within the microwave cavity, and scanning for a signal above the background noise.

To date, only a very small fraction of the viable mass range has been searched with sufficient sensitivity to detect the invisible axion. Current haloscope detectors are greatly hindered by the frequency scan range of existing microwave cavity technology [15,16] (see Chapter 2.4). A study of microwave cavities for axion dark matter detectors was conducted in an effort to expand the capabilities of current haloscopes.

Computer simulations were used to evaluate utilizing periodic arrays of tuning rods and vanes for axion detectors and to assess the effects of symmetry breaking in cavities on the detection capabilities of detectors. The analysis showed that such periodic arrays could be used to increase and tune the search frequencies of microwave cavities used in axion detectors while maintain a large volume (see Chapter 3.4). The simulations further showed that symmetry breaking resulted in reduced sensitivity, mode mixing which caused gaps in the detector scan range, and mode crowding that increased the likeliness of mode mixing and complicated mode detection and tracking (see Chapter 3.2).

A cavity prototype was developed and tested to demonstrate the use of tuning vanes for axion detectors (see Chapter 4). The testing was conducted at temperatures of 300 K, 77 K, and 4.2 K. The results showed that tuning vanes adjusted the frequency of the modes the cavity. However, the prototype demonstrated the sensitivity of modes to symmetry breaking. Due to mechanical misalignments, fabrication defects, and

design flaws, significant mode mixing, mode crowding, and mode localization observed in the cavity prevented the desired search mode from being positively identified.

To improve mode identification capabilities, an in-situ mode test was developed (see Chapter 5). The test combines power from two antenna ports to determine if the field at the antenna locations are in-phase or out of phase. By comparing the phases of the fields at multiple locations and comparing the results to simulation predictions, different TM modes could be distinguished as well as certain TE modes. The test method was demonstrated successfully on an empty cylindrical cavity and a cylindrical cavity with two tuning rods. However, the method was not successfully demonstrated on the prototype multivane cavity.

CHAPTER 2 BACKGROUND

2.1 Axion Particle

The axion is a theoretical pseudoscalar particle which was originally postulated to explain, within the framework of the standard model of particle interactions, why P (parity) and CP (charge conjugation times parity) are conserved by the strong interactions. The Lagrangian for Quantum Chromodynamics (QCD) contains a CP symmetry violating term [17]

$$\mathcal{L}_{\text{QCD}} = \dots + \frac{\bar{\theta}g^2}{16\pi^2} \mathbf{G}_{\mu\nu}^a \tilde{\mathbf{G}}^{a\mu\nu} + \dots, \quad (2-1)$$

where $G_{\mu\nu}^a$ is the gluon strength tensor and g is a colorless coupling. The parameter $\bar{\theta}$ is a consequence of the non-abelian nature of QCD, and is an observable parameter with a value between $-\pi$ and π [18,19]. Without further information, $\bar{\theta}$ would be expected to be of order 1.

As the neutron is composed of quarks, the violation of CP symmetry in QCD should also be observed in the neutron. Indeed, the existence of an electric dipole moment in the neutron would violate CP symmetry, and the strength of the moment could be used to determine the value of $\bar{\theta}$ [20-22]. To date, no experiments have detected a neutron electric dipole moment, with an upper limit being placed at 3.0×10^{-26} e-cm (at 90% CL) [23,24]. The resulting upper limit of $\bar{\theta}$ is $\sim 10^{-10}$, which is many orders of magnitude less than predicted. This extremely small upper bound on $\bar{\theta}$ is the so-called “strong CP problem.”

A solution to the strong CP problem was proposed by Peccei and Quinn [3]. By introducing a new $U(1)$ symmetry to the early universe, $\bar{\theta}$ becomes a dynamical

parameter by obtaining field-dependent term a/f_a , where a is a complex pseudo-scalar field introduced by the symmetry and f_a is an energy scale (temperature). The Peccei-Quinn (PQ) symmetry was spontaneously broken when the universe cooled below f_a , causing $\langle a \rangle$ to settle to a minimum and $\bar{\theta}$ to naturally relax to 0. Weinberg [1] and Wilczek [2] individually showed breaking the PQ symmetry results in the creation of a new pseudo-Nambu-Goldstone boson, dubbed the axion. Though massless at the classical level, the explicit breaking of the symmetry gives the axion a potential. Oscillations about the minimum of this potential result in the axion acquiring a mass.

The mass of the axion arises from the explicit breaking of PQ symmetry by instanton effects and is related to f_a by [5]

$$m_a = \frac{z^{1/2} f_\pi m_\pi}{1+z} \approx 6 \mu\text{eV} \frac{10^{12} \text{GeV}}{f_a}, \quad (2-2)$$

where the pion mass and energy scale are $m_\pi = 135 \text{ MeV}$ and $f_\pi \approx 92 \text{ MeV}$, respectively. The canonical value of $z = m_u/m_d = 0.56$ is used, where m_u and m_d are the masses of the up and down quarks, respectively. Initially the PQ symmetry was believed to break around the weak scale, $f_a \approx 250 \text{ GeV}$, leading to an axion mass of $\sim 100 \text{ keV}$ [14], known as the PQWW (Peccei-Quinn-Weinberg-Wilczek) model. However, beam dump experiments ruled out any such models [25].

Current axion models allow f_a to be orders of magnitude higher than the weak scale, which predict a drastically reduced mass of the axion from the PQWW model. Additionally, the increase in energy scale also increases the difficulty detecting an axion (see Chapter 2.4), and such models are often called the “invisible” axion. The two most accepted invisible axion models are the KSVZ (Kim-Shifman-Vainshtein-Zhakharov) model [26,27] and the DFSZ (Dine-Fischler-Srednicki-Zhitnitsky) model [28,29]. The

KSVZ model, which predates the DFSZ model by about a year, is sometimes referred to as the “hadronic” axion. The KSVZ model adds a new, electrically-neutral heavy quark that carries a $U(1)_{PQ}$ charge to the Standard Model. The DFSZ model requires at least two Higgs doublets, and ordinary quarks and leptons carry PQ charges. The KSVZ axion couples to the heavy quark but not to leptons, while the DFSZ axion couples to both quarks and leptons [5].

2.2 Dark Matter

Significant astrophysical and cosmological evidence for the existence of dark matter exists. In 1933, red shift measurements from the Coma Cluster showed a large disparity between the measured velocity dispersion of the galaxies and the predicted values based on the computed luminous mass [30]. Velocity measurements were used to compute the lower limit on the average mass to light ratio [31]

$$\gamma = 500 \frac{M_{\odot}}{L_{\odot}}, \quad (2-3)$$

where M_{\odot} and L_{\odot} are the mass and luminosity of the sun, respectively. The results were two orders of magnitude larger than expected, and led to the claim that the Coma Cluster contained non-luminous matter. Figure 2-1 shows the observed luminous matter in the Coma Cluster.

Measurements of the rotational velocities of spiral galaxies showed the velocity did not exhibit Keplerian motion beyond the cluster bulge, scaling to $1/r^2$ (the inverse of the radius squared). Instead, the velocities at large radii demonstrated rotational motion in an isometric potential, maintaining a constant velocity regardless of radius [34]. The results strongly suggested a large quantity of non-observable matter. Figure 2-2 shows the rotation curve of galaxy M33 [35], demonstrating a near constant velocity beyond

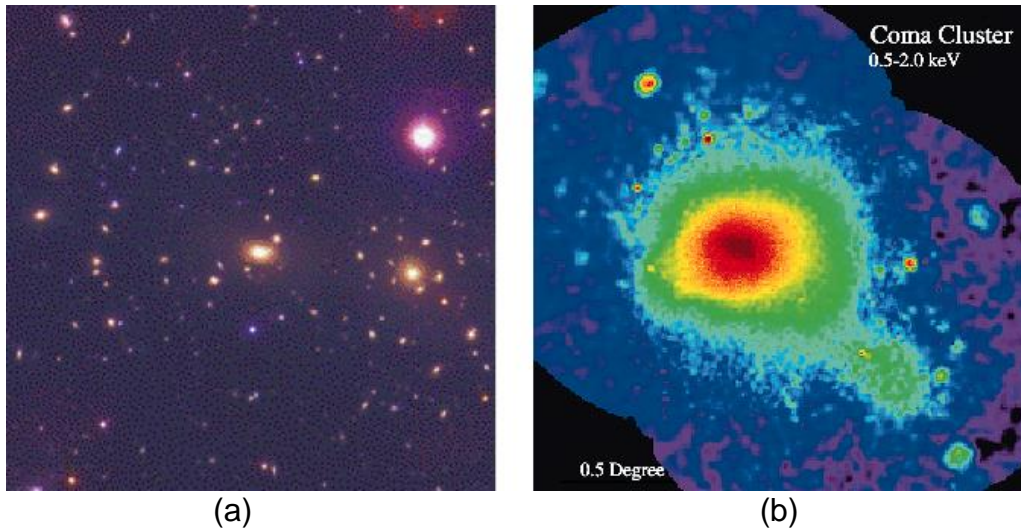


Figure 2-1. Baryonic matter observed in the coma cluster. (a) Optical light [32]. (b) X-ray light [33]. Velocity dispersion measurements of galaxies suggested significant non-luminous mass was present.

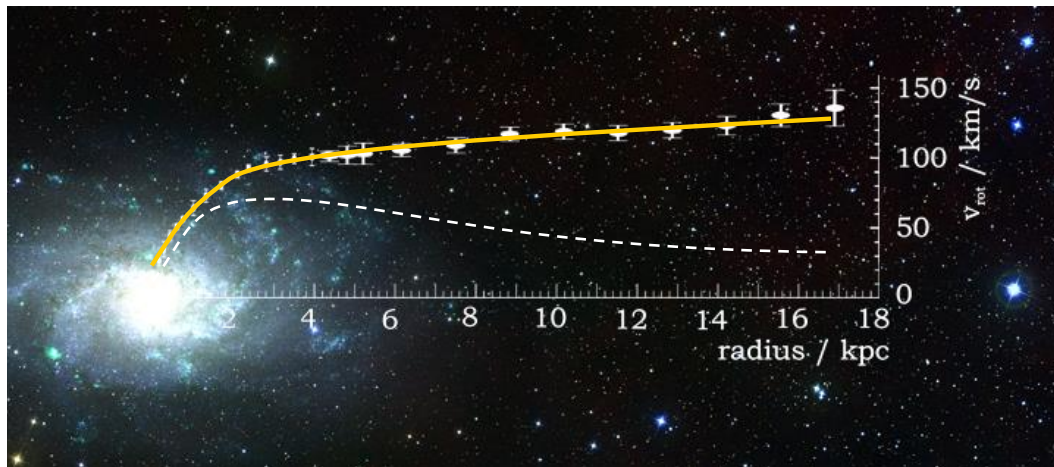


Figure 2-2. Rotation curve of Galaxy M33 [36]. The dashed white line shows Keplerian motion assuming a gravitational potential based on light measurements. The solid yellow line shows rotation in an isothermal halo. The data suggest that significantly more matter is present than can be observed by light emission.

the cluster bulge. The dotted lines show the predicted curve based on the luminous matter. Figure 2-3 shows the rotational curves for four additional galaxies demonstrating similar behavior.

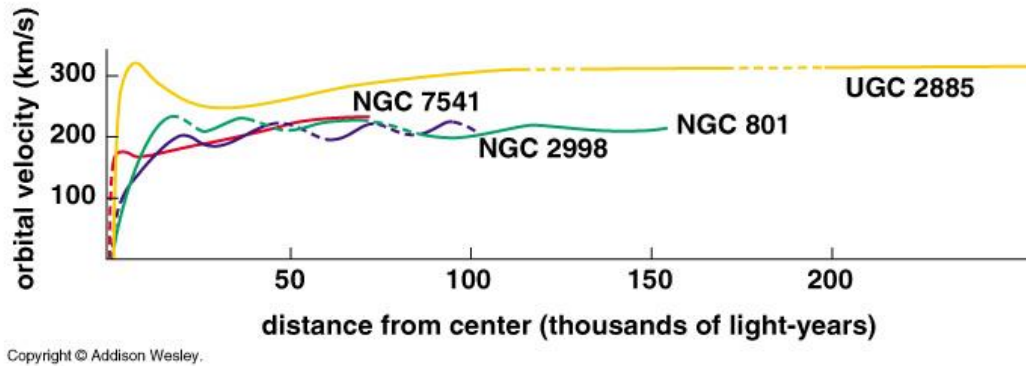


Figure 2-3. Rotation curve of nearby galaxies [37]. Data suggests the galaxies are rotating in an isothermal halo.

Analyses of gravitational lensing have further reinforced the theory of dark matter. As light from distance galaxies passes by a massive gravitational potential, the light is bent by the potential. Observations in the near field depict curved light signatures around the mass sources. Lensing analyses compute the mass of the source. A vast number of weak and strong lensing studies of galaxy clusters have demonstrated a need for additional, non-luminous matter in the universe [38-40]. In some instances, the observed lensing is visible without augmentation or computation. Figure 2-4 shows the gravitational lensing observed in the Abell 2218 galaxy cluster [41]. The lensing is clearly visible on the left side of the figure as depicted by the curved, elongated galaxies. The mass needed to produce such lensing is ten times greater than is perceived through light measurement.

Recently discovered galaxy cluster mergers have revealed some of the strongest evidence for dark matter to date. The x-ray gas from galaxy clusters that merged in the past scattered from collisions, forming a bulk luminous mass around the intersection point. Gravitational lensing studies show the majority mass passed through the intersection point without interaction, producing two separate mass bulges [43,44]. To

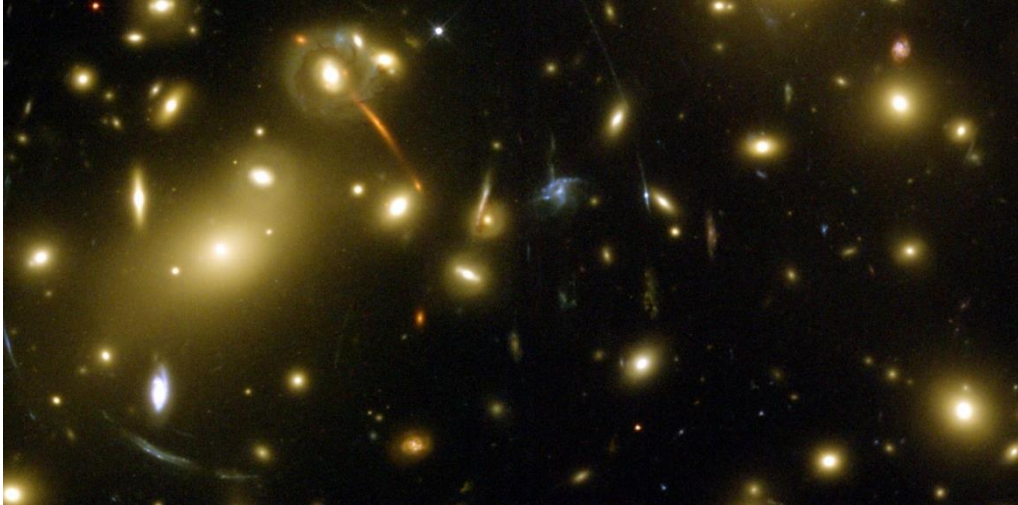


Figure 2-4. Gravitational lensing of the Abell 2218 galaxy cluster [42]. Gravitational lensing of light is visible without augmentation. Weak lensing analyses predict ten times more mass is present than is observed.

date, there is no scientific explanation for these observations besides the existence of dark matter.

Figure 2-5 shows the observations from the Bullet Cluster merger (1E 0657-558) in the optical and x-ray (shown in pink) spectrums. The yellow lines are the mass contour lines resulting from a weak gravitational lensing analysis. The bulk of the x-ray gas is located near the center of the figure. The mass peaks computed from the weak lensing is located at the center of the smallest yellow circles to the sides of the bulk gas, coinciding with the center of the optical cluster centers, suggesting most the mass passed through the intersection point without scattering [45].

While the astronomical evidence for dark matter spans many length scales, the cosmological evidence reaches across several times scales. Observations of high redshift celestial objects provide the abundance of heavy elements present moments after big bang nucleosynthesis. Measured on the ratios of deuterium (^2H), helium (^3He and ^4He), and lithium (^7Li) to hydrogen (H) place constraints on the percent of baryonic

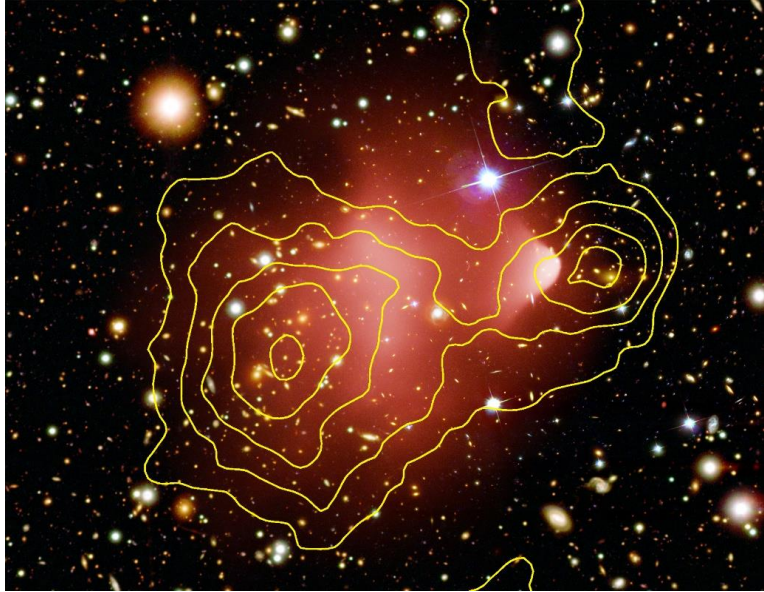


Figure 2-5. Observations from the Bullet Cluster [46]. The yellow lines show the contour lines of the mass computed from weak gravitational lensing. The x-ray gas is shown in pink. Weak lensing suggests the majority of the mass is collisionless, thus non-baryonic.

matter in the universe. Deuterium measurements provide strongest evidence for existence of non-baryonic matter in the universe, as deuterium is extremely sensitive to the initial baryon density of the universe and has no natural mechanism for creation in burning stars.

Figure 2-6 shows the ratio of the measured abundance of ^2H (labeled D), ^3He , ^4He , and ^7Li to the measured abundance of H compared to the abundance predicted during Big Bang Nucleosynthesis. The single lines represent the measurements and the double lines shows the predicted baryon percentage as a function of abundance. The intersection of the lines is the baryon percentage of the universe predicted by each measurement. The measurements of ^2H , ^3He and ^4He estimate baryonic matter makes up only ~5% of the total energy of the universe [47,48], leaving ~95% of the energy (matter or otherwise) unknown.

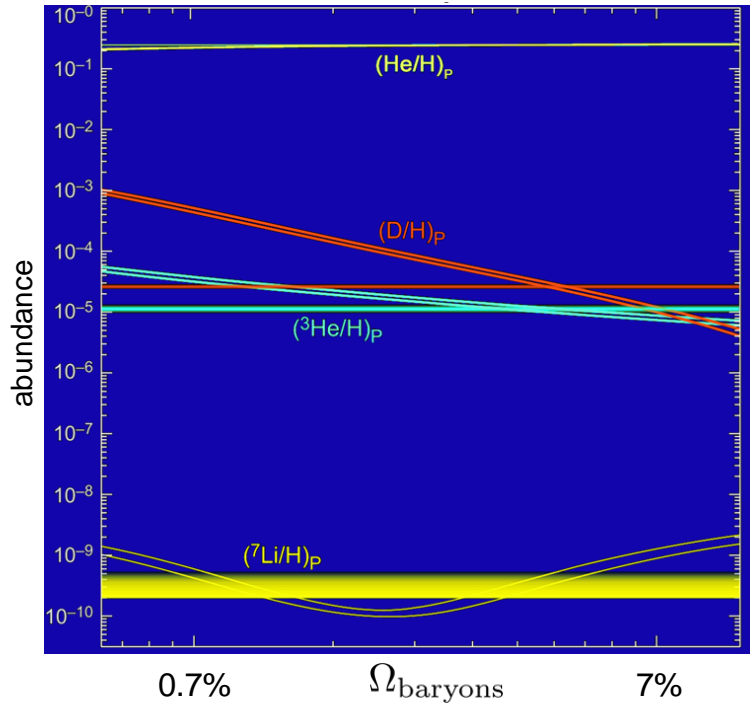


Figure 2-6. Limits on percent of baryons in the universe from nucleosynthesis [49]. The four single lines shows the measured abundance of deuterium (D), helium (^3He and He), and lithium (^7Li) divided by the measured abundance of hydrogen (H). The double lines show the predicted baryon percentage as a function of abundance of each substance. The intersection of the lines show the limit on baryon percentage. The measurements of D, ^3He , and He estimate baryons makes up $\sim 5\%$ of the universe.

Measurements of the cosmic microwave background (CMB) have provided additional evidence for non-baryonic matter 380,000 years after the Big Bang. CMB measurements have shown the universe to be remarkably isotropic with relic quantum fluctuations and acoustic oscillation stretched out to cosmic scales. The power spectrum of the residual power from the fluctuations places constraints on the baryon density in the universe at ~ 0.023 [50]. Figure 2-7 shows the measured temperature of CMB in the universe, depicting the maximum temperature spread of $< 1\text{mK}$. Figure 2-8 shows the power spectrum from the (top) Planck satellite observations with the (bottom) residual fluctuation normalized.

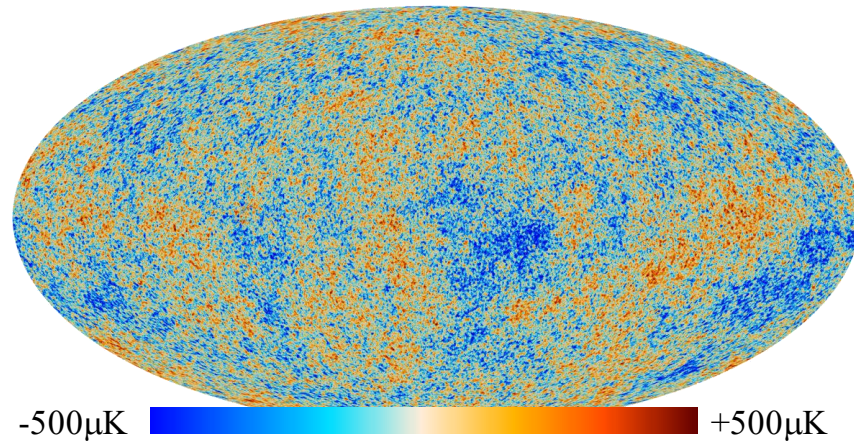


Figure 2-7. Cosmic microwave background measurements from Planck [51]. The thermal spread of < 1 mK shows that the universe is almost perfectly isotropic on the cosmic scale.

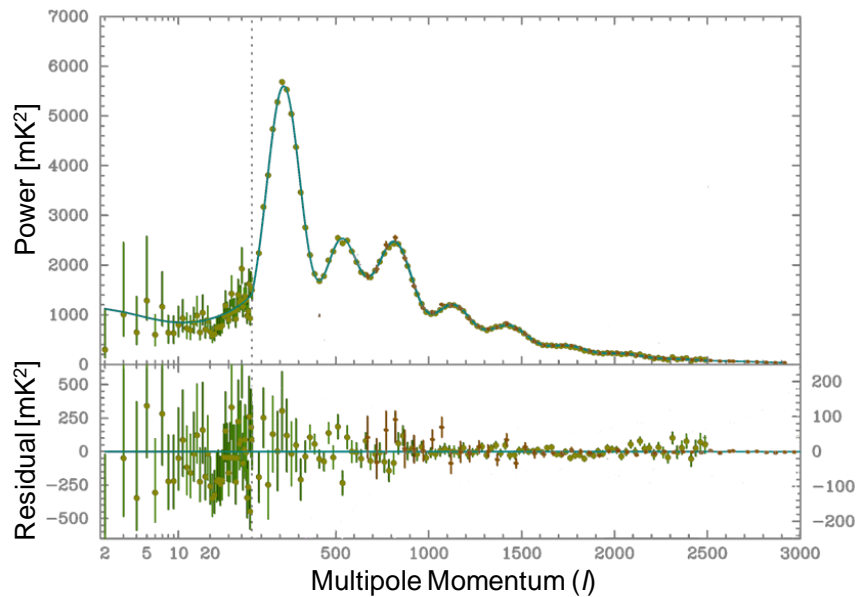


Figure 2-8. Power spectrum of the cosmic microwave background measurements [51]. The top shows the measured power spectrum with the best fit line. The bottom shows the residual of the measurements. The low power fluctuations on the left side of the plot set limits on the baryon mass of the universe at $\sim 2\%$.

Further evidence for dark matter exists in the scale modeling for structure formation in the universe. Current theoretical modeling methods accurately predict the size scale of cosmic structures from observation only when non-baryonic particles are included in the simulations. To align the predictions with observation, the ratio of non-

baryonic matter to baryonic matter needs to be approximately 5 [52]. The non-baryonic matter must also be non-interacting. Figure 2-9 shows the predicted scale of observations methods of cosmological structure using the Λ CDM model (see below) and measured scales. The plot shows that prediction well match observations over all scales.

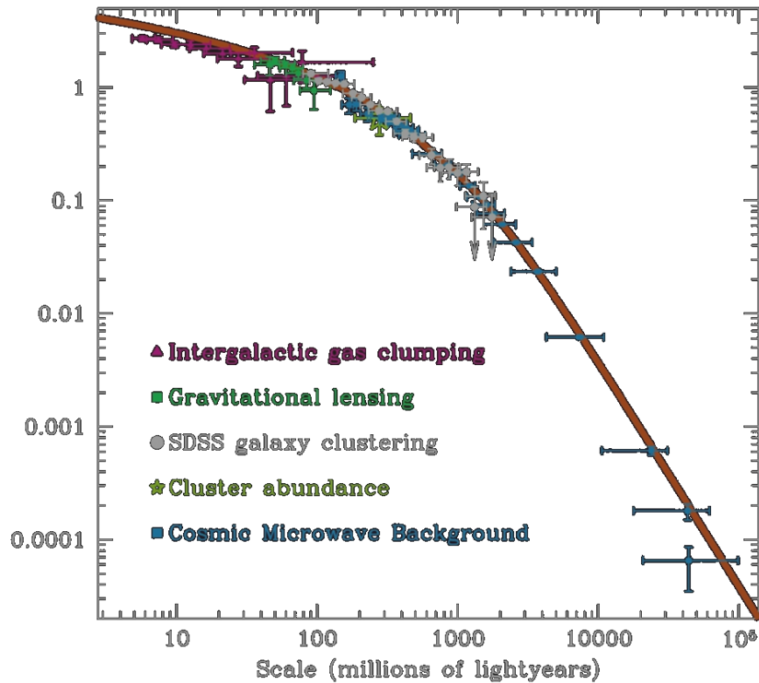


Figure 2-9. Predicted scales of cosmic structure observations using the Λ CDM model [53]. Only when non-baryonic matter is added to the model, do the simulations accurately predict the measurable scales of observation techniques.

Though the evidence for dark matter is plentiful, measurements have established modest bounds on the properties of dark matter. Dark matter must be non-baryonic and collisionless to produce the aforementioned observations. Dark matter must be long lived, as is necessary to produce the results observed from all cosmological time scale up to present day. Additionally, dark matter must have feeble electromagnetic couplings, else signatures of dark matter would have been detected. The abundance of

dark matter is determined by the redshift evolution of the universe pressure-to-density ratio to ~22% [54]. Dark matter is generally considered to be nonrelativistic (cold) as a result of redshift based sky surveys [55]. The property bounds contribute the dark matter portion of the Lambda Cold Dark Matter (Λ CDM) cosmological model of the universe.

Since the origination of the theory of dark matter, various candidates within and beyond the standard model have been proposed. However, the majority these candidates have been excluded through observation or experimentation [56]. Various dark matter candidates are still plausible, though the two most widely considered the strongest are weakly interacting massive particles (WIMP) and the axion. Figure 2-10 shows a visualization of the current field of plausible dark matter candidates.

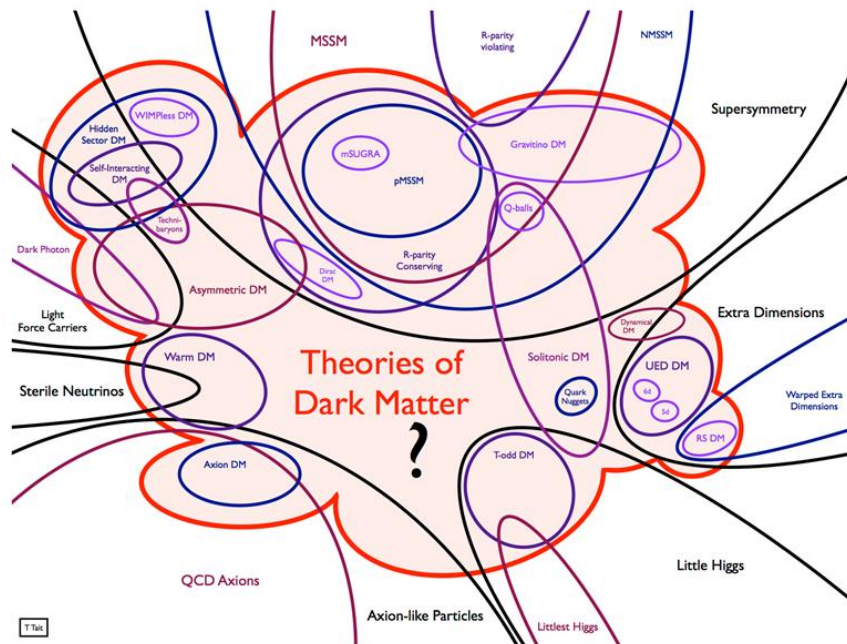


Figure 2-10. Visualization of current theories of dark matter [57]. Various candidates are viable, while WIMPs and CDM axions are generally considered the most plausible.

The WIMP consists of a group of theoretical particles, such as the neutralino and the gravitino, that were produced thermally in the early Universe. The most prominent WIMP theories viable today are predicted by supersymmetry. Current experiments have set strong limits on WIMPs [58] and supersymmetry [59], suggesting additional tuning of the theory may be required.

Axions were first theorized to constitute dark matter in 1983 [4]. The axion particle naturally possesses all the properties of dark matter from its simple extension of the standard model, and is a favored candidate due to its elegant solution to the strong CP problem. The axion is predicted to form a Bose-Einstein condensate, which potentially distinguishes it from other cold dark matter candidates through their phase space structure, supported by astronomical observation [60]. Recently string theory has enhanced the theory of CDM axions as well as other theoretical particles, known as “axion-like” particles (ALP), that spontaneously break a $U(1)$ symmetry similarly to the PQ-symmetry breaking of the axion [61].

2.3 CDM Axions

As solutions to the strong CP problem, axions would need to be abundant at all time scales of the post-inflationary universe. Axions produced through PQ-symmetry breaking would be non-baryonic, nonrelativistic, and collisionless without fine tuning. The axion is dominated by gravitational forces and has an extremely weak coupling to the electromagnetic and weak force. Thus, the axion particle which arises from the Peccei-Quinn solution to the strong CP problem is a natural dark matter candidate.

The mass of the axions is not predicted by the PQ-symmetry breaking theory, but cosmic observation and particle physics experiments have constrained the axion energy

scale, and thus the particle's mass. The duration of the neutrino burst from SN1987A provided the lower bound of $f_a \gtrsim 10^9$ GeV [14]. The cosmic energy density argument places the upper limit. The cosmological energy density of axions increases as the mass of the axion decreases; if $f_a \gtrsim 10^{12}$ GeV, the axion energy density would be too large, causing the early universe to collapse (overclosure) [11-13]. From Eq. 2-2, the allowable mass of the axion is found to be between approximately μeV and meV . The cosmic number density of CDM axions in the allowable mass range is around 10^{11} - $10^{14}/\text{cm}^3$, depending on the mass, though local densities due to caustics produced by the dark matter flow could be several orders of magnitude greater [62].

The coupling of the axion to the standard model particles and forces is so weak that initially it was believed to be undetectable, giving rise to the name "invisible axion." The various couplings are model dependent, but in all axion models within the dark matter mass range, the coupling to standard model particles and forces is $\lesssim 10^{-12} \text{ GeV}^{-1}$, and more often is many orders of magnitude lower [63]. The natural lifetime of an axion is related to mass by

$$\tau_{a\gamma\gamma} \approx \left(\frac{10^5 \text{ eV}}{m_a} \right)^5 \text{ sec.} \quad (2-4)$$

For CDM axions within the allowable mass range, the decay time to convert to a standard model particle is many orders of magnitude greater than the age of the universe, further suggesting that dark matter axions are undetectable.

In 1983, Sikivie [7] suggested using the inverse Primakoff to significantly increase the effective coupling to the electromagnetic force, leading to multiple axion dark matter direct-detection concepts. The electromagnetic interaction of the axion is determined by the Lagrangian for the axion-photon conversion

$$\mathcal{L}_{a\gamma\gamma} = g_{a\gamma\gamma} a \mathbf{E} \cdot \mathbf{B}, \quad (2-5)$$

where a is the axion field, and E and B are the electric and magnetic fields of the two propagating photons, respectively (see Fig. 2-11). The axion-photon coupling constant, $g_{a\gamma\gamma}$, is proportional to the axion energy scale by

$$g_{a\gamma\gamma} = \frac{\alpha g_\gamma}{2\pi f_a}, \quad (2-6)$$

where α is the fine structure constant and g_γ is a model-dependent constant of order 1.

In the KSVZ and DFSZ models, g_γ is equal to -0.97 and 0.36, respectively.

Equation 2-6 leads directly to a model dependent axion-photon coupling constant. In the KSVZ model, the coupling is [26,27]

$$g_{a\gamma\gamma}^{KSVZ} = 0.38 \frac{m_a}{\text{GeV}^2}. \quad (2-7)$$

In the DFSZ model, the coupling is [28,29].

$$g_{a\gamma\gamma}^{DFSZ} = 0.14 \frac{m_a}{\text{GeV}^2}. \quad (2-8)$$

The axion coupling to the photon in the DFSZ is weaker than in the KSVZ model, making detection of axions more challenging if the DFSZ model is accurate.

The Primakoff effect, first theorized by Primakoff [8] in 1951, describes a coherent-nuclear production mechanism for a single photon-to-meson conversion in the presence of a magnetic field. Sikivie [7] detailed how the same mechanism could be used to convert single photons to axions or single axions to photons. (The latter is most often referred to as the inverse Primakoff effect.) In the presence of a static magnetic field, the effective Lagrangian of the axion-photon interaction becomes

$$\mathcal{L}_{a\gamma\gamma} = g_{a\gamma\gamma} a \mathbf{E} \cdot \mathbf{B}_0, \quad (2-9)$$

where \mathbf{B}_0 is the static magnetic field. Figure 2-11 shows the Feynman diagrams for the axion-photon conversion (a) in vacuum and (b) in a static magnetic field from the Primakoff effect.

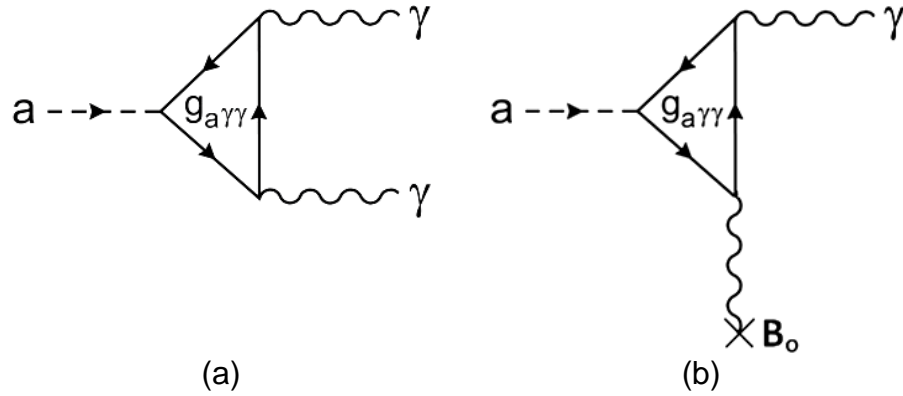


Figure 2-11. Feynman Diagram of Axion-photon Interaction. (a) Interaction in vacuum. (b) Interaction in a static magnetic field due to the Primakoff effect.

The lifetime of the axion from conversion to photons is proportional to \mathbf{B}_0^2 . Conversion due to the inverse Primakoff effect in the presence of a significantly strong magnet produces a lifetime many orders of magnitude lower than that of conversion in vacuum, greatly increase the conversion rate. This process is effective for relativistic or non-relativistic axions.

As axion dark matter is nonrelativistic, the frequency of the photon from the axion-photon conversion is $f \approx m_a c^2 / h$, where c is the speed of light in a vacuum and h is Planck's constant, with a very small adjustment for the relative kinetic energy. If CDM axions are virialized, $0 < v < c/1000$, making the spread of energy for conversions $\sim 10^{-6} m_a c^2$ [10] and has a Maxwellian distribution. For non-virialized axion flows, the energy spread could be significantly lower [64].

Sikivie proposed two direct-detection experiments utilizing the inverse Primakoff effect, a haloscope and a helioscope. An axion haloscope uses a microwave cavity

permeated by a strong magnetic field to resonant the conversion of CDM axions to photons, producing an enhanced signal for detection (see Chapter 2.4). An axion helioscope converts axions produced in the sun. The helioscope is composed of a long telescope permeated by a strong magnetic field; the telescope it pointed at the sun, converting relativistic solar axions (not CDM axions) released from the sun to photons inside the telescope. A photon detector at the back of the telescope observes the signal produced from the conversion.

The most sensitive haloscope and helioscope detectors presently are the Axion Dark Matter eXperiment (ADMX) [65] and the CERN Axion Solar Telescope (CAST) [66], respectively. Both experiments use cryogenic systems to reduce background noise and highly-sensitive signal detectors to enhance sensitivity. The Haloscope At Yale Sensitive To Axion CDM (HAYSTAC) published results in 2016 that were not sensitive to KSVZ coupling [67] (not included in Fig. 2-12). No dark matter or solar axions have been directly detected to date.

Figure 2-12 shows the axion exclusion plot around the mass range for dark matter axions. The y-axis is the axion-to-photon coupling. The yellow bar bounds the KSVZ (upper) and DFSZ (lower) coupling, depicting the linear relationship between photon coupling and mass of the axion for the two models (see Eq. 2-7 and Eq. 2-8). The green area shows the axion search-space that has been excluded by haloscope detectors; ADMX is the leftmost green bar and the only exclusion area to include some KSVZ coupling region within the allowable mass range for CDM axions. The blue area shows the axion search space that has been excluded by the CAST helioscope. The

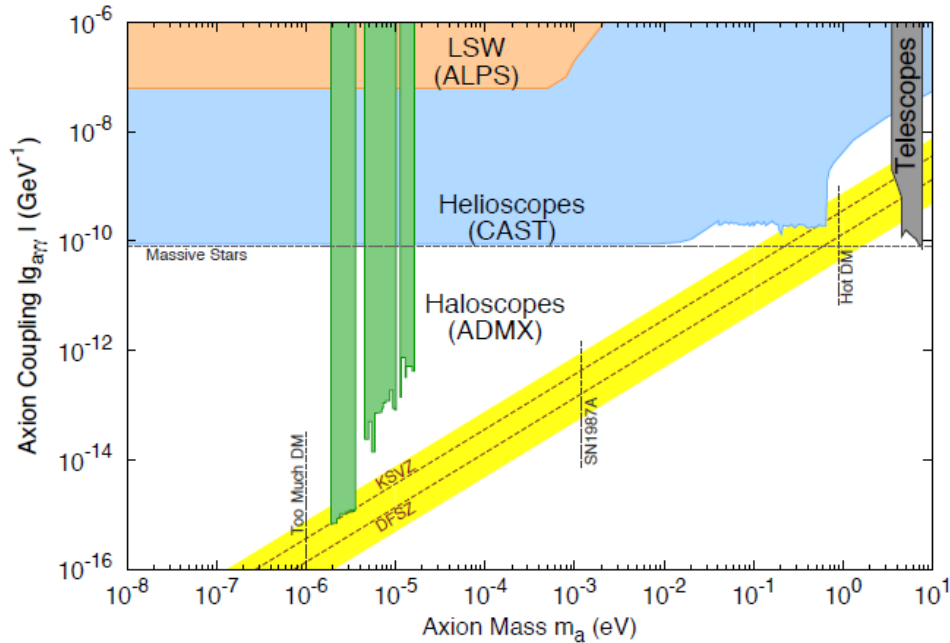


Figure 2-12. Axion exclusion plot near the CDM axions mass range [68]. The y-axis is the axion-to-photon coupling. The yellow bar bounds the KSVZ (upper) and DFSZ (lower) coupling. The green, blue, and pink areas show the axion search-space that has been excluded by haloscopes, helioscopes, and LSW experiments, respectively. Most of the search-space of CDM axions is yet unexplored.

pink area shows axions excluded by light-shining-through-wall (LSW) experiments (see below). The plot shows that most of the search-space of CDM axions is yet unexplored.

More recently, various axion detectors have been proposed, with a select few being developed. The LSW (light-shining-through-wall) experiment, which uses the Primakoff effect and inverse Primikoff effect in series, is perhaps the most notable of these experiments. The LSW experiments passes coherent light though a static magnetic field, converting a fraction of the photons to axions which must conserve energy and momentum of the light. The axions would pass through a physical barrier (wall) into a second static magnetic field, where a fraction of the axions would convert back to a photon [69].

LSW experiments are broad searches that detect any ALP, but a detection cannot determine the mass of the particle nor distinguish an axion from ALPs. The detector does not search for CDM axions, as the axions are generated in the laboratory. The Any Light Particle Search is a LSW detector that uses optical cavities to enhance sensitivity. The Any Light Particle Search has set axion exclusion limits that are shown on Fig. 2-12, though they are less encompassing than the CAST limits.

The Center for Axion and Precision Physics (CAPP) in South Korea is conducting research on axion dark matter detectors to search for axions of mass greater than ~ 20 μeV . CAPP is developing novel microwave cavity concepts to include a toroidal cavity haloscope design. The proposed International Axion Observatory (IAXO) experiment will be an improved solar axion search that is projected to be an order of magnitude more sensitive than CAST.

Additional axion detection schemes have been proposed recently, though none have published limit yet. NMR-based detectors detect the spin precession caused by low mass ($< 10^{-9}$ eV) axions; the Cosmic Axion Spin Precession Experiment (CASPEr) is a proposed NMR-based experiment [70]. A detection method using a LC circuit was proposed by Sikivie et al. [71]. The presence of axions in a static magnetic field alter Maxwell's equations, causing an oscillating electric current to flow along magnetic field lines. An LC circuit within a static magnetic field could be used to detect the oscillating current. The detector is believed to be sensitive to axions with mass approximately 10^{-7} - 10^{-9} eV. The University of Florida is developing a prototype detector. Variants of haloscope detectors using periodic dielectrics within waveguides and optical cavities are being developed at the University of Washington [72]. The dielectrics "spoil" half of an

antisymmetric mode within the waveguide or cavity, yielding higher-order modes with a nonzero form factor. The tuning is conducted by adjusting the cavity length and the spacing between the dielectrics.

2.4 Axion Haloscope Detectors

To date, the only detection scheme that has been sensitive enough to detect CDM axions at KSVZ coupling is the haloscope. As previously stated, the axion haloscope uses a microwave cavity resonator permeated by a high-strength static magnetic field. The magnetic field increases the conversion rate of axions to photons, due the inverse Primakoff effect, proportional to $|\mathbf{B}_0|^2$. Increasing the strength of the magnetic field thus increases the power of the axion signal and, consequently, the sensitivity of a haloscope detector. Typically, a haloscope uses a superconducting solenoidal magnet to maximize the field strength.

The signal of the axion conversion would have a bandwidth (b_a) determined by the kinetic energy spread, ΔE , at half of the peak probability. The effective quality factor of the signal (Q_a) would be the peak energy divided by the bandwidth, $E/\Delta E \approx c^2/v\Delta v$, where v and Δv are the peak velocity and velocity dispersion of the local axions. From the predicted energy spread of the (virialized) axion conversion, $Q_a \gtrsim 10^6$. Figure 2-13 shows the local kinetic energy distribution of galactic axions, normalized such that the peak is one. The energy spread at half the peak is on order $10^{-6} m_a c^2$.

The microwave cavity of the haloscope is of great importance. From Eq. 2-9, it can be shown that the cavities capacity to resonate the axion decay signal is proportional to $\int dx^3 \mathbf{E}_{mnp} \cdot \mathbf{B}_0$ over the volume of the cavity, where \mathbf{E}_{mnp} is the electric field of each individual cavity mode identified by the indices \mathbf{m} , \mathbf{n} , and \mathbf{p} . For right-circular

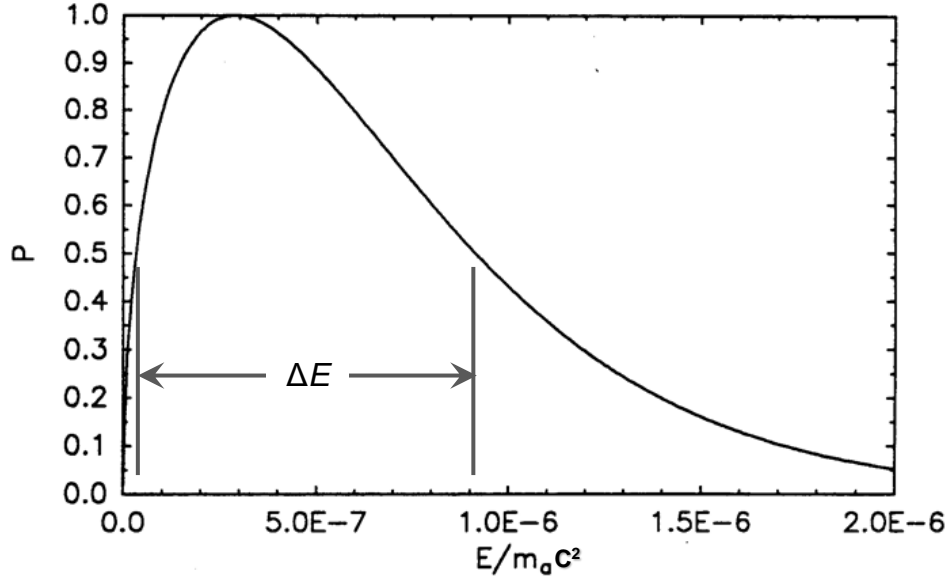


Figure 2-13. Local kinetic energy distribution of galactic axions [73]. The plot is normalized such that the peak has a value of one. The distribution is Maxwellian (virialized axions). The energy spread is $\sim 10^{-6} m_a c^2$. For non-virialized axions, the energy spread will be much less.

cylindrical cavities, the indices correspond to the polar coordinates ϕ , ρ , and z , respectively. From this proportionality, a normalized “form factor”, is established to quantify the capacity of a given cavity mode to resonantly enhance the signal from axion conversion,

$$C_{mnp} \equiv \frac{|\int d^3x \mathbf{E}_{mnp}(\mathbf{x}) \cdot \mathbf{B}_0|^2}{B_0^2 V \int d^3x \varepsilon(\mathbf{x}) |\mathbf{E}_{mnp}(\mathbf{x})|^2}, \quad (2-10)$$

where V is the volume of the cavity and ε is the permittivity within the cavity normalized to vacuum. The form factor can be interpreted as a coupling factor between a cavity mode and the axion-photon interaction. C_{mnp} has a value between zero, where no conversion signal is resonated, to one, where the signal is resonated homogeneously within the entire volume of the cavity. Note, due to boundary conditions of the electromagnetic fields, a value of one is unobtainable.

The most common cavity configuration for a haloscope is a right-circular cylindrical cavity oriented in the detector such that the center axis is normal to the magnetic field central axis. As the cavity's ability to resonate the axion signal is dependent on the integral over the cavity volume, maximizing the volume of the cavity is desired, and utilizing a right-circular cavity in a cylindrical solenoid obviously maximizes the available volume. From Eq. 2-10, only modes that have an electric field component parallel to the static magnetic field of the detector will yield an observable signal. In a right-circular cylindrical cavity in a solenoidal magnet, only transverse magnetic (TM) modes and hybrid modes (see Chapter 3.1) containing some longitudinal electric field will resonate the axion signal. Transverse electric (TE) and transverse electromagnetic (TEM) modes will yield no detectable signal.

In order for the axion signal to resonate a mode, the signal power spectrum must sufficiently overlap with the mode power spectrum. Thus, the frequency of the axion signal ($f \approx m_a c^2 / h$) must match the frequency of the mode (f_{mnp}) within f / Q_{min} , where Q_{min} is the minimum of the cavity's loaded quality factor, Q_L (see Chapter 3.1) and the effective quality factor of the signal, Q_a . Typically, Q_L is significantly less than the Q_a , making $Q_{min} = Q_L$.

Because the mass of the axion is unknown, the frequency of searchable cavity modes must be incrementally adjusted, or "tuned", to scan for CDM axions within a finite mass range. As the frequency of the search mode is tuned, the measurement frequency of the detector is simultaneously changed to match. Cavity tuning has historically been done using one or two conducting or dielectric tuning rods that run approximately the length of the cavity that are mechanically rotated about a pivot point off-center of the

rods, though other concepts have been proposed in recent years (see Chapter 3.4). A “search mode” is a resonant mode of a cavity that can be tuned across a frequency range that is within the allowable mass range of CDM axions and has a sufficient form factor, C_{mnp} , to yield a non-negligible signal throughout the search range.

The frequency step size, the change in frequency of the search mode from one scan to the next, must be no larger than f_{mnp}/Q_L . Most haloscope experiments will use step sizes $\Delta f \leq f_{mnp}/5Q_L$ to maintain a more consistent sensitivity throughout the search range, reducing the integration time at each step but increasing the total number of steps across a range. Figure 2-14 shows a schematic of mechanical tuning using (a) one large tuning rod and (b) two smaller tuning rods. Generally conducting rods will increase the search mode frequencies and dielectric rods will decrease the frequencies (see Chapter 3.1).

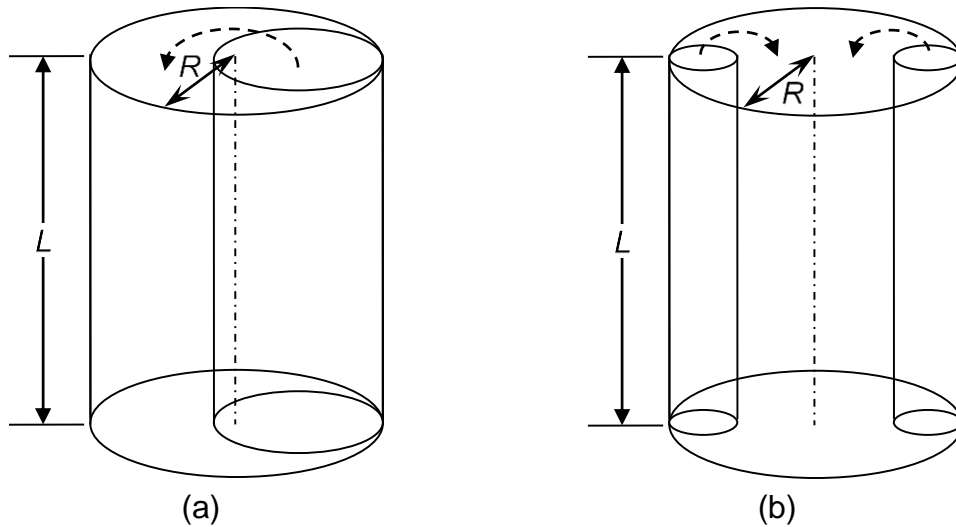


Figure 2-14. Schematic of mechanical tuning of haloscope cavities. (a) One tuning rod. (b) Two tuning rods. A mechanical gap must exist between the top of the tuning rods and the endcaps of the cavity to enable motion. Generally conducting rods will increase the search mode frequencies and dielectric rods will decrease the frequencies.

For an empty cylindrical cavity, only TM_{0n0} will resonate the axion signal due to mode anti-symmetry. However, an empty cavity cannot be tuned to scan across a frequency range. Mechanical tuning requires longitudinal symmetry breaking within the cavity to maneuver the rods. The symmetry breaking causes modes to break pure TE/TM/TEM field configurations (see Chapter 3.2). Though the search modes of such cavities are no longer pure TM_{0n0} modes, the nomenclature TM_{0n0} for cylindrical cavities is often used to indicate the mode the perturbed modes most closely resemble. In particular, the most common search mode for a haloscope is usually referred to as the TM_{010} mode, though the mode is a perturbed form of the pure mode, and “ TM_{010} -like” would be a more accurate description.

The TM_{010} mode tends to be the most desired mode to use for axions searches as it yields the highest form factor, with higher values of n (e.g., TM_{020} , TM_{030} , etc.) providing reduced form factors with a value of $\sim C_{010}/4^{(n-1)}$ for a given cavity. C_{010} refers to the form factor for the TM_{010} (-like) mode of the cavity at a given tuning configuration. Depending on the tuning rod(s) configuration, occasionally symmetry breaking of a mode with $m > 0$ yield a mode with a nonnegligible form factor (see Chapter 2.2).

From the proportionalities noted above and those of the axion parameters, the power transmitted from the cavity is [10]

$$P_{mnp} \approx g_{a\gamma\gamma}^2 \frac{\rho_a}{m_a} B_0^2 C_{mnp} V Q_L, \quad (2-10)$$

where ρ_a is the local density of CDM axions and $g_{a\gamma\gamma}$ is the model dependent axion-photon coupling constant given by Eq. 2-7 for the KSVZ model and Eq. 2-8 for the DFSZ model. Note, ρ_a/m_a is the number density, n_a , of the axion. Q_L is mode dependent, though the indices for the mode are conventionally not written. The

sensitivity of the haloscope is maximized when the antenna coupling to the cavity is over-coupled, such that the loaded quality factor is one-third the unloaded cavity quality factor, $Q_L = Q/3$ [15]. However, implementing and maintaining that coupling throughout a frequency range scan is challenging; typically, the antenna is critically coupled to the cavity so that $Q_L = Q/2$.

The search scheme of an axion haloscope consists of tuning the search mode of the microwave cavity to an initial frequency, measuring the signal within the cavity for a set scan time, adjusting the search mode frequency by an amount less than f/Q_L , and repeating until the scan range of the search mode is exhausted. Because the axion signal adds coherently and noise adds incoherently, the longer the scan integrates measurements, the greater the sensitivity of the detector. Thus, the scan integration time is determined by the desired sensitivity to axion-photon coupling and confidence of the search detecting the axion if it exists at a scanned mass. For example, a search at DFSZ coupling sensitivity and 95% confidence requires considerably longer integration time per frequency step than a search with the same detector at KSVZ coupling sensitivity and 90% confidence (see Eq. 2-13).

The confidence is related to a signal-to-noise ratio of an observation, which is related back to the power transmitted by the radiometry equation [74],

$$\frac{s}{n} = \frac{P_{mnp}}{k_B T_n} \sqrt{\frac{t}{b_a}}, \quad (2-11)$$

where T_n is the system noise temperature of the detector, k_B is Boltzmann's constant, t is the scan integration time, and b_a is the axion signal bandwidth. For axion searches,

typically $s/n > 5$ to obtain a confidence of $>95\%$. The signal bandwidth can be expressed in terms of the axion mass,

$$b_a \approx \frac{m_a}{Q_a}. \quad (2-12)$$

Solving Eq. 2-11 for t yields the integration time required for a given frequency

$$t \approx \left(\frac{s}{n}\right)^2 \frac{k_B^2 T_n^2 m_a}{P_{mnp}^2 Q_a}. \quad (2-13)$$

If the Q_L is less than Q_a , then the number of signal bandwidths that can be scanned simultaneously is $N = Q_a/Q_L$. Thus, the integration time for a single frequency step is $\sim t/N$. The total integration time (Δt) required to scan over a small frequency range (Δf) is

$$\Delta t = \Delta f \left(\frac{s}{n}\right)^2 \frac{k_B^2 T_n^2 Q_L}{P_{mnp}^2 Q_a}. \quad (2-14)$$

Combining Eq. 2-10 and Eq. 2-14 and rearranging yields the haloscope scan rate [75],

$$\frac{df}{dt} \approx \left(\frac{s}{n}\right)^{-2} \left(\frac{1}{k_B T_n}\right)^2 \frac{g_{a\gamma\gamma}^4 \rho_a^2}{m_a^2} B_0^4 V^2 C^2 Q_L Q_a. \quad (2-15)$$

Note the scan rate is proportional to $g_{a\gamma\gamma}^4$, so increasing the sensitivity of a haloscope detector from KSVZ coupling to DFSZ coupling would require an increase in scan time of ~ 50 , if no changes were made to the detector.

Equation 2-15 demonstrates that an axion haloscope search is a tradeoff between sensitivity and time. Because a typical haloscope search is conducted on order of a year, a higher scan rate is obviously desired. As experiments have no control over axion parameters such as mass and local density, the haloscope is designed to maximize scan rate as much as possible. As mentioned earlier, the magnetic field strength is maximized to obtain the highest axion-to-photon conversion rate. The microwave cavity design and fabrication ideally maximizes volume, quality factor, and

form factor, but, as discussed below, other search factors can constrain the cavity parameters (see also Chapter 3.4).

The system noise temperature significantly affects the detectors sensitivity. From Eq. 2-15, a minimum temperature is desired. The temperature dictates the signal noise; the higher the system temperature is, the longer the required integration time will be for a given signal-to-noise ratio. Haloscope experiments make great efforts to reduce the system noise temperature by placing the detector within a cryostat. Recent experiments have utilized SQUID (superconducting quantum interference device) amplifiers to obtain near quantum-limited electronic noise and dilution refrigerators to obtain physical temperatures of the cavity at $T \approx 150$ mK.

Figure 2-15 shows (a) a graphic representation of a haloscope using a cavity within a solenoidal magnet and (b) the expected axion signal of a detection. Axions converted to photons via the inverse Primakoff effect will resonate when the frequency of a mode with a sufficient form factor is nearly the same as the axion signal. The physical temperature of the cavity is minimized to reduce the noise. An antenna, usually critically coupled, will extract the signal along with the physical temperature noise. The extracted signal is carried to a power meter, often passing through amplifiers and gaining electrical noise. The system noise is the total of the physical temperature and electrical noise. The power spectrum of the readings would yield a detection signal if the detector is sensitive enough.

Under even the most optimistic circumstances, the axion signal within the haloscope cavity is extremely weak, requiring amplification and a well-conceived receiver chain to enable detection. Each experiment has individual receiver chains that

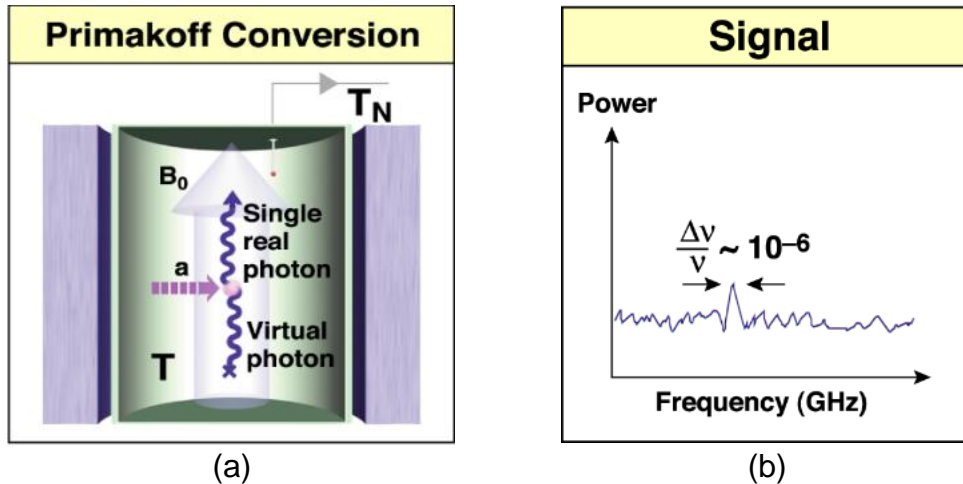


Figure 2-15. (a) Graphic representation of a haloscope detector using a solenoid magnet and a cylindrical microwave cavity, and (b) an anticipated detection signal of CDM axions [68]. The signal can only be observed if the frequency of a mode with a nonnegligible form factor nearly matches the axion signal and the detector sensitivity is sufficient. The signal-to-noise ratio shown is ~ 5 .

optimize their detector, but nearly all will have cryogenic and noncryogenic amplifiers to increase the signal strength, filters to isolate the axion signal, mixers to make the signal more manageable, and circulators to prevent any reflected power from corrupting the measurements. Detectors usually have power injection ports to take Q_L measurements at different tuning configuration and a data storage system to conduct data analysis after a search is conducted.

The largest and most sensitive microwave cavity axion search to date is ADMX. Currently located at the University of Washington, the Department of Energy funded experiment searches for CDM axions with a haloscope detector using a 7.6 Tesla superconducting solenoid and a $\sim 0.15 \text{ m}^3$ copper cylindrical microwave cavity. The TM_{010} frequency of the cavity is tuned using two copper rods. The signal measurement is extracted through a critically coupled antenna and amplified through a receiver chain using a SQUID amplifier and several HFET (heterostructure field effect transistors). The

signal is passed through a crystal filter and mixed down to 35 KHz before being stored in medium-resolution and high-resolution bins for data analysis. A medium-resolution analysis searches for axions signals with a Maxwellian velocity distribution [76] and a high-resolution analysis searches for signals with a fine-structure velocity spread [77].

Figure 2-16 shows (a) the schematic of the receiver chain and (b) a photograph inside a cavity depicting the tuning rods.

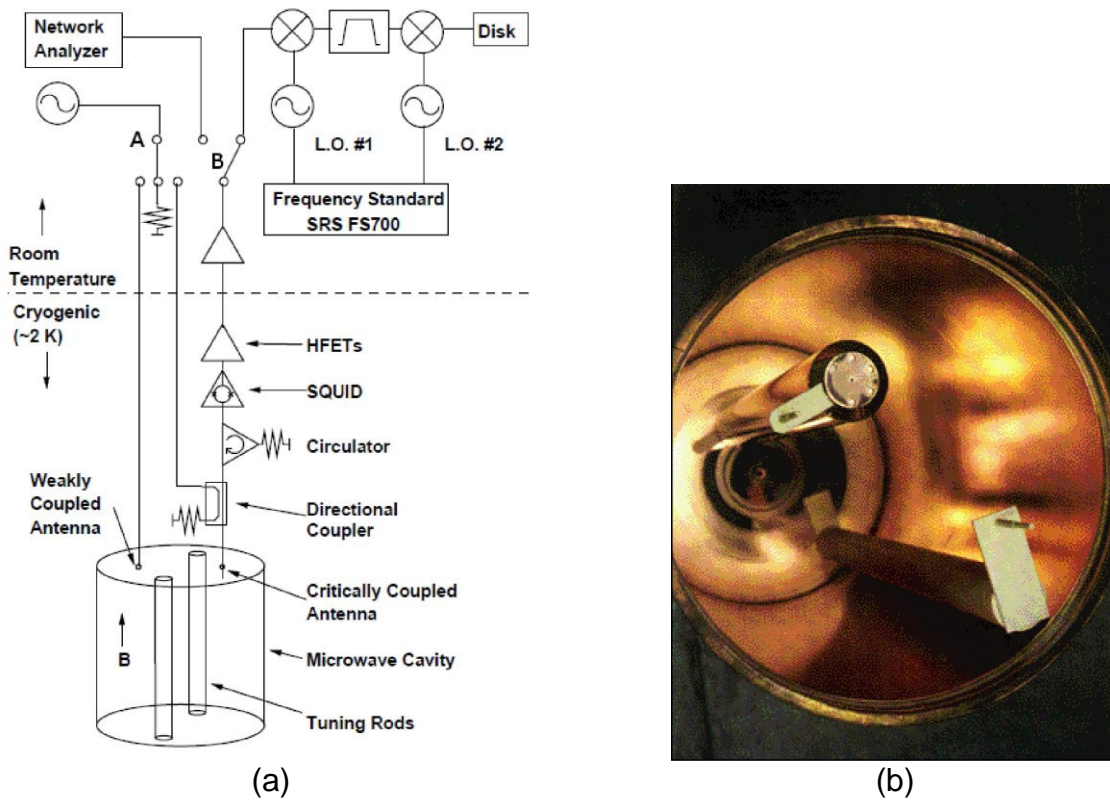


Figure 2-16. (a) Schematic of ADMX receiver chain [78] and (b) photograph of the inside of the ADMX microwave cavity [68]. The tuning rods are incrementally rotated about the offset pivot points to adjust the TM_{010} frequency, providing scanning across an axion mass range of $\sim 2\text{-}4 \mu\text{eV}$.

ADMX has successfully excluded CDM axions at the KSVZ coupling sensitivity in the mass range of $1.9\text{-}3.7 \mu\text{eV}$ ($460\text{-}890 \text{ MHz}$) [79-82] using a $\sim 3 \text{ K}$ system temperature detector. In 2016, ADMX installed a dilution refrigerator and is currently operating the detector at $\sim 300 \text{ mK}$ system temperature over approximately the same

mass range. The new data is projected to be at the DFSZ coupling sensitivity. However, the current detector is not sensitive above $\sim 4 \mu\text{eV}$ ($\sim 1 \text{ GHz}$) and a new haloscope cavity is required to search at higher masses. Figure 2-17 shows the exclusion limits published by ADMX.

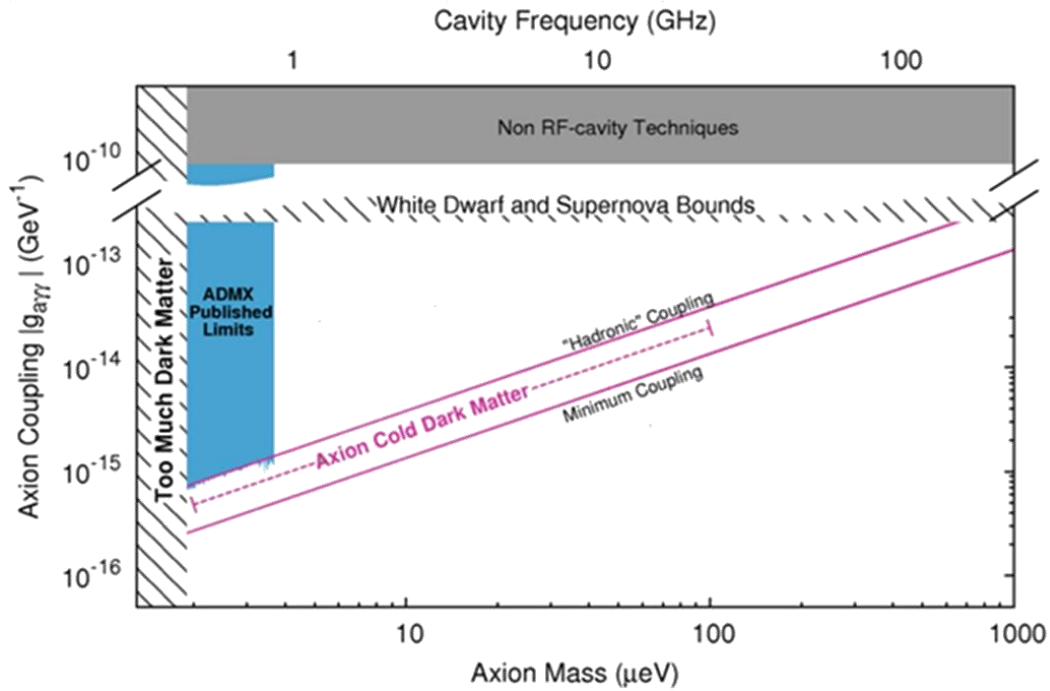


Figure 2-17. Axion exclusion plot showing published results of ADMX [68]. The KSVZ coupling is labeled “Hadronic” and the DFSZ coupling is labeled “Minimum”. ADMX has excluded axions to KSVZ coupling in the mass range of $1.9\text{--}3.7 \mu\text{eV}$ ($460\text{--}890 \text{ MHz}$) [79-82].

The following proportionalities illustrates the challenges of axion searches at higher mass. The frequency of a search mode scales as the axion mass. The search mode frequencies scales inversely with the cavity radius and the volume as the cube of the radius when the ratio of the length to the radius, L/R , is maintained. At temperatures below $\sim 7 \text{ K}$, Q_L scales as $f^{-2/3}$ with constant L/R due to the anomalous skin effects (see Chapter 3.1) and the power transmitted from the cavity will scale as $\sim f^{-8/3}$. Thus, using the current state-of-the-art for haloscope cavities, doubling the scan frequency of the

detector by simply scaling the cavity will reduce the signal power by a factor of ~ 6.3 and increase the scan time by a factor of ~ 25 for the same confidence and coupling sensitivity.

HAYSTAC (formerly ADMX-HF) recently conducted a CDM axion search at a mass range of ~ 23.6 - 24.0 μeV [67]. The experiment only obtained a sensitivity of ~ 2.3 times KSVZ coupling despite using a dilution refrigerator and a near quantum-limited superconducting amplifier and searching across a modest mass range for about four months. The results well demonstrate the difficulties of scanning for axions at frequencies above ~ 1 GHz as detailed above. Researchers now know that new microwave cavity technologies need to be developed to search for CDM axions with masses above ~ 4 μeV (~ 1 GHz).

CHAPTER 3
MICROWAVE CAVITIES FOR AXION HALOSCOPE DETECTORS

3.1 Microwave Cavity Theory

A resonant cavity is any arbitrarily shaped enclosure with electromagnetic-reflecting boundary conditions, which are most commonly satisfied by conducting walls. Resonant cavity theory is derived as an extension of waveguide theory. Assuming a steady-state solution that maintains an oscillating \mathbf{E} and \mathbf{B} field with a time component consisting of $e^{-i\omega t}$, where $\omega = 2\pi f$, Maxwell's equations within the cavity are

$$\nabla \cdot \varepsilon \mathbf{E} = 0, \quad (3-1)$$

$$\nabla \cdot \mathbf{B} = 0, \quad (3-2)$$

$$\nabla \times \mathbf{E} = i\omega \mathbf{B}, \quad (3-3)$$

$$\nabla \times \frac{1}{\mu} \mathbf{B} = -i\omega \varepsilon \mathbf{E}, \quad (3-4)$$

where ε and μ are the permittivity and the permeability inside the cavity, respectively.

The conducting boundary conditions are

$$\mathbf{n} \times \mathbf{E} = 0, \quad (3-5)$$

$$\mathbf{n} \cdot \mathbf{B} = 0, \quad (3-6)$$

where \mathbf{n} is the normal vector to the surface of the boundary.

Combining Eq. 3-3 into Eq. 3-4 and vice versa yields the field-separated equations

$$\frac{1}{\varepsilon} \nabla \times \frac{1}{\mu} \nabla \times \mathbf{E} - \omega^2 \mathbf{E} = 0, \quad (3-7)$$

$$\nabla \times \frac{1}{\varepsilon} \nabla \times \frac{1}{\mu} \mathbf{B} - \omega^2 \mathbf{B} = 0. \quad (3-8)$$

Under the most general conditions, the permittivity and the permeability inside the cavity are a function of location, \mathbf{x} , and ω can have any positive value. Expanding Eq. 3-7 and Eq. 3.8 yields

$$(\nabla^2 + \mu\epsilon\omega^2)\mathbf{E} = \mu\nabla\frac{1}{\mu}\times\nabla\times\mathbf{E} + \nabla(\nabla\cdot\mathbf{E}), \quad (3-9)$$

$$(\nabla^2 + \mu\epsilon\omega^2)\mathbf{B} = \mu\left(\nabla\frac{1}{\mu}\times\nabla + \nabla\times\nabla\frac{1}{\mu}\right)\times\mathbf{B} - \frac{\nabla\epsilon}{\epsilon}\times\left(\mu\nabla\frac{1}{\mu} + \nabla\right)\times\mathbf{B}. \quad (3-10)$$

If the cavity has constant permittivity and permeability, the right side of Eq. 3-9 and Eq. 3-10 go to zero, yielding the wave equations

$$(\nabla^2 + \mu\epsilon\omega^2)\mathbf{E} = 0, \quad (3-11)$$

$$(\nabla^2 + \mu\epsilon\omega^2)\mathbf{B} = 0. \quad (3-12)$$

In arbitrary geometry, the waves flow in a direction dictated by the boundary conditions. Because the system is closed, standing waves are formed. If the boundary conditions are constant in the longitudinal direction (i.e., constant cross-section) and the ends of the cavity (endcaps) are normal to the longitudinal axis, forming a right cylinder, then the solution to the wave equations will be of the form

$$\mathbf{A} \sin\left(\frac{p\pi z}{L}\right) + \mathbf{B} \cos\left(\frac{p\pi z}{L}\right), \quad (3-13)$$

where L is the distance between the endcaps (cavity length), z is the distance (between 0 and L) along the longitudinal axis between the endcaps, and p is a nonnegative integer. \mathbf{A} and \mathbf{B} are the electric or magnetic field in the cavity, depending on the solution.

When the cavity maintains translational invariance, or longitudinal symmetry, the solution can be separated into transverse magnetic (TM) and transverse electric (TE) solutions. The wave equation can be reduced to the 2-dimensional wave problem

$$\left(\nabla_t^2 + \mu\epsilon\omega^2 - \left(\frac{\rho\pi}{L}\right)^2\right)\psi = 0, \quad (3-14)$$

where ψ is the magnitude of the electric or magnetic field in the z-direction for the TM and TE solutions, respectively. By definition, B_z and E_z for the TM and TE solutions, respectively, are zero. The symbol ∇_t indicates the 2-dimensional vector differential operator in the transverse direction.

For a right-circular cylindrical cavity, the longitudinal direction is along the cylinder axis. The electric field in the z-axis for the TM solutions is given by [83]

$$E_z = E_0 J_m\left(\frac{x_{mn}}{R}\rho\right) e^{\pm im\phi} \cos\left(\frac{\rho\pi z}{L}\right), \quad (3-15)$$

where J_m is the m^{th} order of the Bessel function of the first kind, and x_{mn} is the n^{th} root of $J_m(x) = 0$. R is the radius of the cavity, ρ is the distance from the center between 0 and R , and ϕ is the angle between 0 and 2π relative to an arbitrary baseline on the cavity cross-section. E_0 is a nonzero electric field used to indicate an arbitrary scalar value of the eigenfunction solution. The plus/minus in the exponential acts on ϕ and indicates a polarization of the modes. Modes with $m > 0$ have a 2-state degeneracy, with $+\phi$ and $-\phi$ polarization. For rotationally invariant cavities, the orientation of the polarization is arbitrary.

Equation 3-15 shows that the TM solution to the 2-dimensional wave equation Eq. 3-14 is a set of finite solutions, or modes, with integer values of m , n , and p . The characteristics of the Bessel and cosign functions dictate that m and p are nonnegative while n must be positive. But none have an upper limit, indicating that the solution set is infinite. Each solution oscillates at a frequency

$$f_{mnp} = \frac{1}{2\pi\sqrt{\mu\epsilon}} \sqrt{\left(\frac{x_{mn}}{R}\right)^2 + \left(\frac{\rho\pi}{L}\right)^2}. \quad (3-16)$$

Note, the minimum TM frequency for an empty cavity is the TM_{010} mode frequency, denoted as $f_0 = 0.1145 \text{ GHz}\cdot\text{m}/R$. For TE modes, x_{mn} is replaced with x'_{mn} , the n th root of the $J'_m(x) = 0$.

Figure 3-1 shows images of the E_z field through a cross-section of the cavity for the (a) TM_{010} , (b) TM_{110} , and (c) TM_{020} . The cross-section is parallel to the cavity axis and the outer edge of the images are the conducting boundaries. Red indicates higher field and blue indicates lower field, with zero field at the boundaries. The blue diagonal line in (b) and the blue circle in the middle of (c) are nodes where the field is zero. On one side of the node E_z is out of the page and on the other side E_z is into the page. The orientation of the TM_{110} mode is arbitrary.

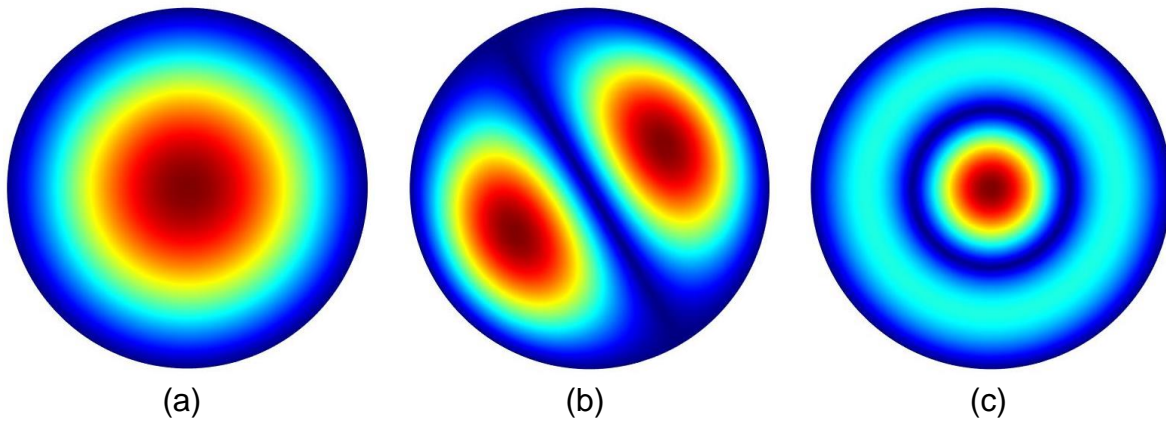


Figure 3-1. Cross-sectional images of the E_z field in an empty cylindrical cavity. (a) TM_{010} . (b) TM_{110} . (c) TM_{020} . The cross-section is parallel to the cavity axis and the outer edge of the images are the conducting boundaries. Red indicates higher field and blue indicates lower field with zero field at the outer boundaries. The mechanism of selecting the orientation of the TM_{110} mode is unknown.

From Eq. 2-10, for empty circular cylindrical cavities, only TM_{0n0} modes will have a nonzero form factor due to the anti-symmetry of the other TM modes, as the opposing fields will cancel each other out when integrated over the cavity volume, and the absence of a E_z field in the TE modes. The TE solutions are similar in nature, containing

an infinite set of modes with a \mathbf{B} field and frequency indicated by some m , n , and p integer values. Equation 3-14 denotes two decoupled Sturm–Liouville eigenvalue equation, so the solution is a complete set of decoupled orthogonal modes (TM and TE) defined by

$$\int d^3x \mathbf{E}_i(\mathbf{x}) \cdot \mathbf{E}_j(\mathbf{x}) = \delta_{ij}, \quad (3-17)$$

$$\int d^3x \mathbf{B}_i(\mathbf{x}) \cdot \mathbf{B}_j(\mathbf{x}) = \delta_{ij}, \quad (3-18)$$

where i and j indicate any TM or TE mode and δ_{ij} is the Kronecker delta. The orthogonality can be applied to degenerate modes, but a rotational transformation of $\pi/2$ about the z -axis must be applied to one of the modes.

Due to rotational invariance of the cavity, the orientation of the degenerate mode is chosen arbitrarily or with no known mechanism (see Fig. 3-1(a)). No research has been published as to how the orientation would be determined by nature. However, no theory could be tested, as any testing would require the presence of an antenna within the cavity, breaking the symmetry and providing a basis of orientation.

A microwave cavity used in a haloscope must have a tunable search mode, making an empty cylindrical cavity unusable for the detector. Currently, the most common method of generating a tunable mode that will resonate the axion-photon conversion is to insert one or more tuning rods that are rotated off axis to translate through the cavity (see Fig. 2-14). The rod creates additional boundaries within the cavity, which changes the solution and the frequency of the modes.

Because the cavity of a haloscope operates within a static magnetic field, a relative permeability of $\mu \approx 1.0$ is desired for the tuning rods. As the Laplacian is a measure of scalar curvature of the mode, Eq. 3-14 shows that conducting rods will

typically result in an increase in frequency for TM. The additional boundary conditions with zero tangential electric field require the TM mode to return to zero at the boundary, causing the scalar curvature of the field to increase (see Fig. 3-6), unless the mode has a node at/near the boundary condition already. The TM_{01p} modes will always experience an increase in frequency; higher-order m and n modes will often experience an increase depending on where the rod is in location to the node(s) of the mode.

When the conducting rod runs the length of the cavity, Eq. 3-14 is valid, and the solution is an infinite set of orthogonal modes that meet the criteria of Eq. 3-17 and Eq. 3-18. The addition of an interior boundary allows for an infinite set of transverse electromagnetic (TEM) modes to exist in addition to the TE and TM modes where

$$f_p = \frac{\rho}{\pi L \sqrt{\mu \epsilon}}. \quad (3-19)$$

The E_z field of the TM modes takes a form similar to Eq. 3-15, but with the single Bessel function (J_m) replaced with a summation of Bessel functions of the first and second kind [84].

Figure 3-2 shows images of the E_z field through a cross-section of the cavity with a coaxial conducting rod for the (a) TM_{010} , (b) TM_{110} , and (c) TM_{020} . The white area in the center is the location of the rod with no field solution. The dark blue at the inner and outer boundaries indicates zero field. The diameter of the rod is $R/2$.

Dielectric rods, most often made of alumina (Al_2O_3) for haloscope cavities, typically results in a decrease in the TM modes, as the mode tends to localize within the rod, resulting in an overall reduction in scalar curvature [15]. However, the rod location relative to a node also contributes to the effect on modes with higher order than TM_{01p} .

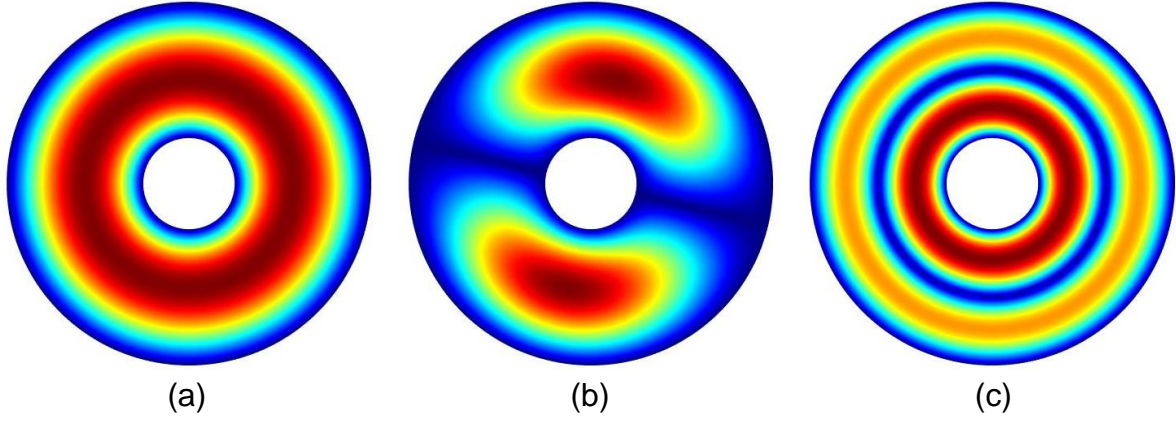


Figure 3-2. Cross-sectional images of the E_z field in a cylindrical cavity with a coaxial conducting rod. (a) TM_{010} . (b) TM_{110} . (c) TM_{020} . The cross-section is parallel to the cavity axis. The white area in the center is the location of the conducting rod ($d = R/2$); a field solution is not included in the images as there is zero field inside the conductor. The outer edge of the images and white center areas are the conducting boundaries. Red indicates higher field and blue indicates lower field with zero field at the conducting boundaries. The mechanism of selecting the orientation of the TM_{110} mode is unknown.

From Eq. 3-9 and Eq. 3-10, the field equations of a cavity with dielectric rods are

[85]

$$(\nabla^2 + \mu\epsilon\omega^2)\mathbf{E} = \nabla(\nabla \cdot \mathbf{E}), \quad (3-20)$$

$$(\nabla^2 + \mu\epsilon\omega^2)\mathbf{B} = (\nabla \times \mathbf{B}) \times \frac{\nabla\epsilon}{\epsilon}. \quad (3-21)$$

If the rods run the entire length of the cavity and are parallel to the center axis, symmetry is preserved. TE_{0np} and TM_{0np} modes exist in the form of [86]

$$\mathbf{E} = \mathbf{E}_0(r)e^{-i\omega t} \cos\left(\frac{p\pi z}{L}\right), \quad (3-22)$$

$$\mathbf{B} = \mathbf{B}_0(r)e^{-i\omega t} \sin\left(\frac{p\pi z}{L}\right). \quad (3-23)$$

In order to meet the boundary conditions, modes with $m > 0$ must break pure TE and TM configuration and incorporate some E_z and B_z field, respectively [87,88]. The new eigenfunction solutions are hybrid modes. The electric and magnetic fields of the

hybrid modes are coupled, which changes the orthogonality to a “biorthogonal” basis defined as [89,90]

$$\int d^3x \mathbf{E}_i^*(\mathbf{x}) \times \mathbf{B}_j(\mathbf{x}) \cdot \hat{\mathbf{z}} = 0, \quad i \neq j, \quad (3-24)$$

where \mathbf{E}_i^* is the complex conjugate of \mathbf{E}_i . When the dielectric rod is off-axis from the cavity, rotational invariance is broken, and all modes are hybrid to meet the boundary conditions [91]. Figure 3-3 shows images of the E_z field through a cross-section of the cavity with a coaxial dielectric rod for the (a) TM_{010} , (b) TM_{110} , and (c) TM_{020} . The field is localized within the dielectric, outlined by a dotted line, when compared to Fig. 3-1.

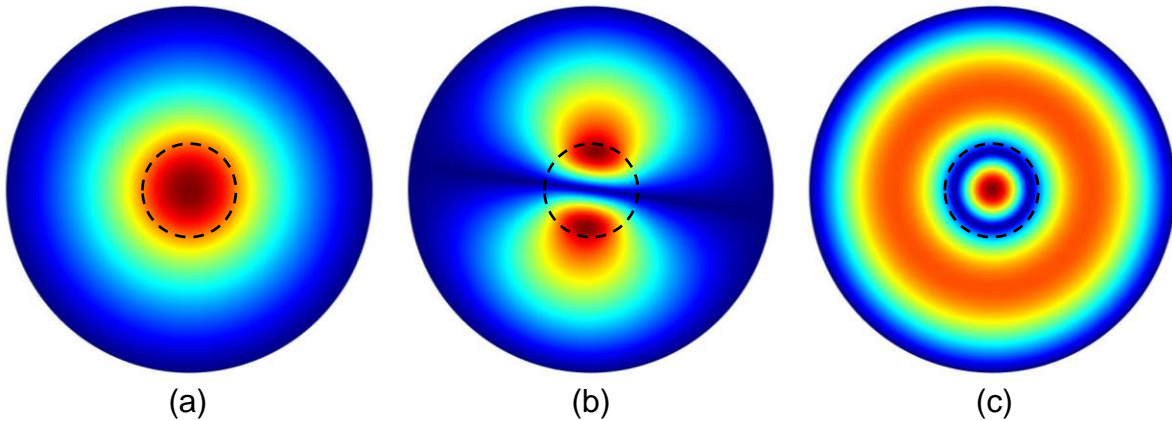


Figure 3-3. Cross-sectional images of the E_z field in a cylindrical cavity with a coaxial dielectric rod. (a) TM_{010} . (b) TM_{110} . (c) TM_{020} . The cross-section is parallel to the cavity axis and the outer edge of the images are the conducting boundaries. The dielectric rod is outlined by a dotted line and is the same diameter as the conducting rod in Fig. 3-2 ($d = R/2$). Red indicates higher field and blue indicates lower field with zero field at the outer boundaries. Localization of the field within the dielectric can be seen. The mechanism of selecting the orientation of the TM_{110} mode is unknown.

As energy is stored in a cavity as a resonance, power is simultaneously lost through the boundaries as well as any lossy material that is inside the cavity. A frequency dependent measure of the energy storing efficiency of a resonating cavity is the quality factor, Q . The quality factor of any resonator is defined as

$$Q \equiv -\frac{\omega}{\frac{dU}{dt}} U, \quad (3-25)$$

where U is the energy stored in the cavity and ω is the resonant frequency. Though Q for a cavity is mode dependent, it is not common to use subscripts to annotate the mode.

For a cylindrical cavity with conducting tuning rods, the Q for a TM mode is given by [83]

$$Q = L \left[\delta_{ends} + \delta_{wall} \xi \frac{L}{R} + \sum_n \delta_{rod} \xi'_n \right]^{-1}, \quad (3-26)$$

where δ_i is the skin depth of the fields in each cavity component, identified by the subscript. The summation is over n number of tuning rods. The variables ξ and ξ' are dimensionless numbers of order unity, defined by

$$\xi^{(r)} \equiv \frac{1}{\mu\epsilon\omega^2} \frac{A}{S} \oint \frac{d|\frac{\partial\psi}{\partial n}|^2}{\int da|\psi|^2}, \quad (3-27)$$

where ψ is the 2-dimensional field solution to Eq. 3-14. A and S are the cross-sectional area and circumference of the cavity, respectively. The prime differentiates between the walls and the tuning rods: without the prime, the line integral is around the boundary of the walls; with the prime the line integral is around the boundary of the n^{th} tuning rod. For both, the surface integral is across the cavity.

When all the boundaries of the cavity are homogeneous (i.e., made of the same material), the skin depth is constant throughout the cavity. Equation 2-26 reduces to

$$Q = \frac{L}{2\delta} \frac{1}{1 + \frac{L}{2R} \sum \xi^{(r)}}. \quad (3-28)$$

The summation is over all the tuning rods plus the wall. For modes with $p = 0$, Eq. 3-28

is multiplied by 2 and L is replaced by $2L$. The quality factor is highly dependent fabrication method of the cavity and tuning rods.

To inject power into a resonating cavity, the cavity must be coupled to a power source; to extract power to a receiver chain or measurement device, the power sink must be coupled to the cavity. Coupling is achieved through an antenna inserted into the cavity or through a waveguide feed connecting to aperture in the cavity. An antenna can take the form of a probe or a loop. An infinitely thin probe antenna will only be excited by an electric field that runs parallel to the axis of the probe, while an infinitely thin loop antenna will only be excited by a magnetic field that is normal to the plane of the loop. Figure 3-4 depicts (a) a probe antenna excited by an electric field and (b) a loop antenna excited by a magnetic field. The arrows indicate the electric field and the crosses indicate the magnetic field into the page.

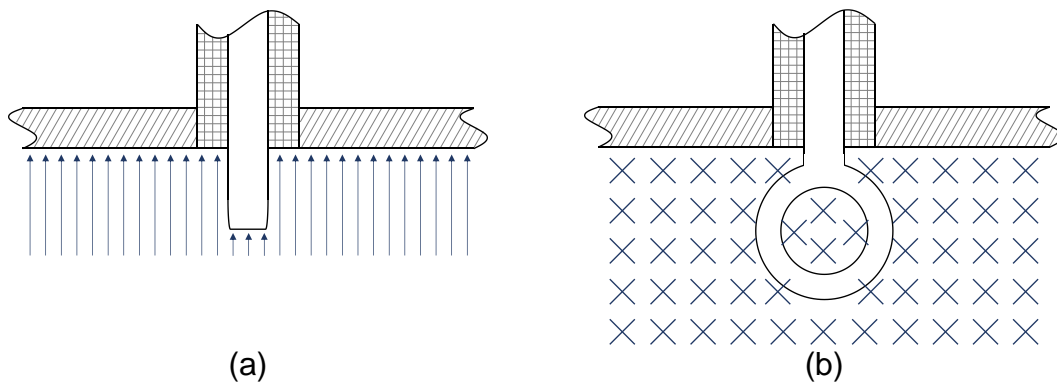


Figure 3-4. Antenna coupled to a cavity through a wall or endplate. (a) Probe antenna. (b) Loop antenna. Blue arrows in (a) are electric field lines. Blue crosses in (b) are magnetic field line going into the page. The fields shown interact strongly with the antennas shown. The hatched area represents a dielectric used as a coaxial waveguide to transmit the signal to/from the cavity.

The most common way to couple to a TM mode in a cylindrical cavity is via a probe antenna through an endplate. The amount of coupling is controlled by the penetration depth of the probe: the greater the depth, the stronger the coupling.

Because the antenna is a source of power absorption, the Q of the cavity is reduced by the presence of the antenna. The quality factor of a cavity with an antenna is called a loaded quality factor, given by

$$Q_L = \left[\frac{1}{Q} + \frac{1}{Q_A} \right]^{-1}, \quad (3-29)$$

where Q_A is the quality factor of the antenna, which is removing energy from the cavity. Q_A decreases with increased coupling and is approximately inversely proportional to y^4 , where y is the insertion depth of the antenna. When the power loss in the cavity equals the loss through the antenna, the antenna is critically coupled and $Q_L = Q/2$.

Because real antennas are not infinitely thin, the antenna will perturb the fields. Specifically, a probe antenna will bend the electric field locally, which results in a weak interaction with the crossing field. TE and TEM modes are therefore commonly observed with a probe antenna inserted into the endplate of cylindrical cavities, though usually at a much lower power than the TM modes. The frequency shift caused by the antenna can be estimated using perturbation theory for each mode [92],

$$\Delta\omega \approx \omega \frac{\Delta U_B - \Delta U_E}{U}, \quad (3-30)$$

where ΔU_E and ΔU_B are the change in the stored electric and magnetic energy, respectively. The effects on the field require numerical analysis to predict.

Waveguide coupling is achieved by connecting to an aperture in the cavity. The aperture can be designed to filter modes. The aperture size also affects the coupling between the cavity and waveguide; a smaller aperture results in a reduced coupling. The Q of the aperture is

$$Q_A = \frac{Z_A}{\omega L_A}, \quad (3-31)$$

where Z_A and L_A are the shunt impedance and inductance the of the aperture, respectively.

The physical temperature of the cavity also affects the Q of the modes. As temperature of a conductor decreases, the mean free path of the electrons increases. Simultaneously, lowering the temperature of a conducting cavity decreases the skin depth. At temperatures below T_{ASE} , the mean free path of the electrons exceeds the cavity skin depth. The response of free electrons within a conductor to an externally applied electric field becomes nonlocal, such that the current at a location is dependent on the field elsewhere [93].

The long mean free path puts the cavity in the anomalous skin effects (ASE) regime. In ASE, the skin depth of the cavity is [94]

$$\delta_{ASE} = \left(\frac{m_e c^2 v_f}{2\pi N e^2 \mu \omega} \right)^{\frac{1}{3}}, \quad (3-32)$$

where m_e and e are the mass and charge of the electron, respectively, v_f is the Fermi velocity, and N is the electron number density. Equation 3-32 gives rise to a frequency dependence of Q

$$Q \propto \omega^{-\frac{2}{3}}. \quad (3-33)$$

3.2 Symmetry Breaking

Symmetry breaking has been shown to have negative effects on the form factor of search modes in haloscope cavities [15,16]. Two types of symmetry breaking exist: transverse and longitudinal. In a circular cylindrical cavity, transverse symmetry breaking is a loss of discrete or continuous rotational invariance. Transverse symmetry can be broken by placing one or more tuning rods off-axis or using noncircular tuning rods. Longitudinal symmetry breaking is a loss of translational invariance within the

boundaries of the cavity. Longitudinal symmetry can be broken using discontinuous tuning rods that do not bridge the entire length of the cavity. Tilting the rod(s) or endcaps, or warping the shape of the cavity wall break both transverse and longitudinal symmetry.

Transverse symmetry breaking from displacing a conducting rod causes localization of the electric fields in TM modes, but the electric and magnetic field remain decoupled. Therefore, Eq. 3-14 is valid as is the orthogonality of modes defined by Eq. 3-17 and Eq. 3-18. The solution to the eigenfunction consists of a combination of several Bessel functions of the first and second kind [95], where the mode subscripts m , n , and p are preserved.

Figure 3-5 shows images of the E_z field through a cross-section of the cavity with an offset conducting rod for the (a) TM_{010} , (b) TM_{110} , and (c) TM_{020} . The tuning rod is shown as a white circle; the offset is $x = R/4$. The localization of the electric field is observed to the left of the rod. One degeneracy of the TM_{110} mode is shown; the second degenerate mode is less obvious by visual inspection. The orientation of the TM_{110} modes are now determined by the offset of the rod. The TM_{020} mode is also less obviously identified visually than the TM_{020} mode shown in Fig. 3-2.

Localization of a mode from transverse symmetry breaking causes the frequency to change. ADMX and HAYSTAC take advantage of this phenomena to tune the search mode frequency of their detectors. In general, moving a tuning rod away from the center axis of the cavity will lower the frequency of the TM_{010} because the curvature of the field is reduced. Figure 3-6 shows the electric field of the TM_{010} mode inside a cylindrical cavity with the tuning rod (a) on-axis and (b) off-axis. The field is localized in the larger

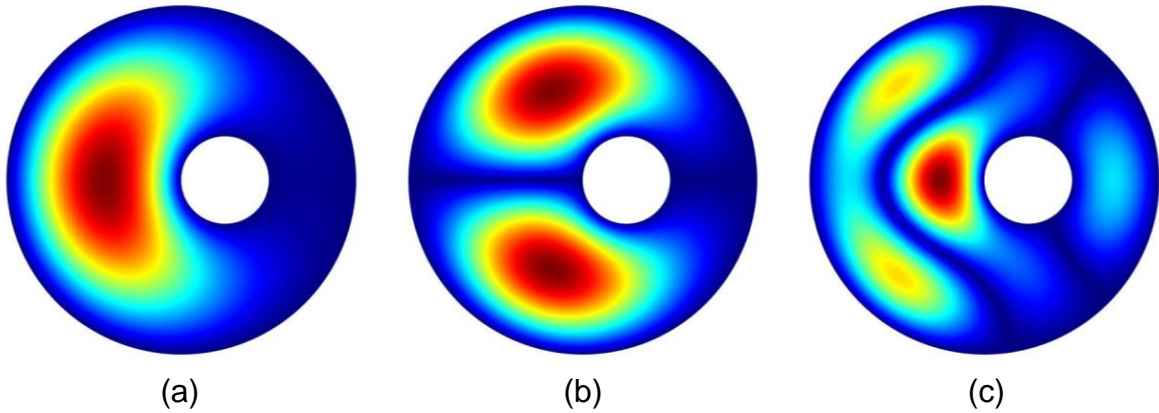


Figure 3-5. Cross-sectional images of the E_z field in a cylindrical cavity with an offset conducting rod. (a) TM_{010} . (b) TM_{110} . (c) TM_{020} . The cross-section is parallel to the cavity axis. The white area in the center is the location of the conducting rod ($d = R/2$) offset by $R/4$; a field solution is not included in the images as there is zero field inside the conductor. The outer edge of the images and white center areas are the conducting boundaries. Red indicates higher field and blue indicates lower field with zero field at the boundaries. Localization of the field is seen to the left of the rod.

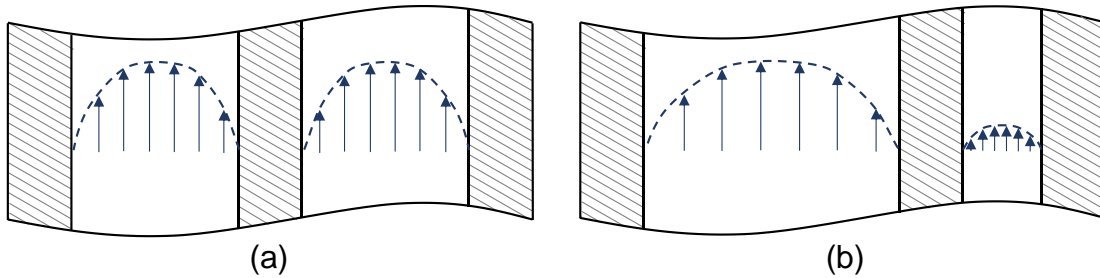


Figure 3-6. Example of the electric field of the TM_{010} mode inside a tuned cylindrical cavity depicting the curvature of the field. (a) On-center tuning rod. (b) Off-center tuning rod. The cross-section is cut through the $x-z$ plane and shows a portion of the cavity. The localization in (b) mirrors the localization shown in Fig. 3-5(a). The curvature of (a) is greater than the curvature of (b), resulting in a higher TM_{010} frequency in (a) than (b). The fields lines are for visualization and are not to scale.

cross-sectional area when the rod is off axis. The widening of the field reduces the curvature. In the non-localized area, the reduction of the field reduces the curvature.

From Eq. 3-14, the reduced curvature of the field produces a reduced mode frequency.

At higher-order modes, translation of a tuning rod has even less intuitive effects, and multiple rods further complicate the mode solutions. Small displacements of a

single rod toward the center usually increase the frequency of higher $TM_{0,r0}$ modes, but quite often the tuning rod position localizes the field in a way that causes a mode frequency to decrease as the tuning rods approach the center of the cavity. Predicting when this occurs typically require numerical analysis. Often when multiple rods are used, the next higher search mode above the TM_{010} changes from one mode to another depending on the configuration, complicating the use of higher TM modes for axion searches.

Breaking rotational invariance causes the form factor of the cavity to decrease due to transverse localization of the electric field. Figure 3-7 shows a plot of the TM_{010} mode (top) frequency and (bottom) form factor as a function of tuning rod displacement from a finite element model (FEM) of a circular cylindrical cavity. The simulation used an eigenfrequency solver conducted with a prepackaged program, COMSOL version 5.1 [96]. The radius of the model cavity was $R = 6.826$ cm and the tuning rod diameter is $0.532R$. The x-axis is the displacement of the rod from the center axis (x) normalized by the cavity radius. The detector's magnetic field is assumed to be homogeneous and in the z-direction for computing C . Note TM_{010} frequency for the empty cavity is $f_0 = 1.68$ GHz.

The plot demonstrates moving the tuning rod off-center reduces the frequency and breaking transverse symmetry decreases the form factor significantly. TM mode frequencies scale as the inverse of the radius when all other geometry (length, tuning rods, etc.) is kept proportional and the mode subscript is $p = 0$ (see Eq. 3-16). The form factor is always independent of radius when all geometry is kept proportional.

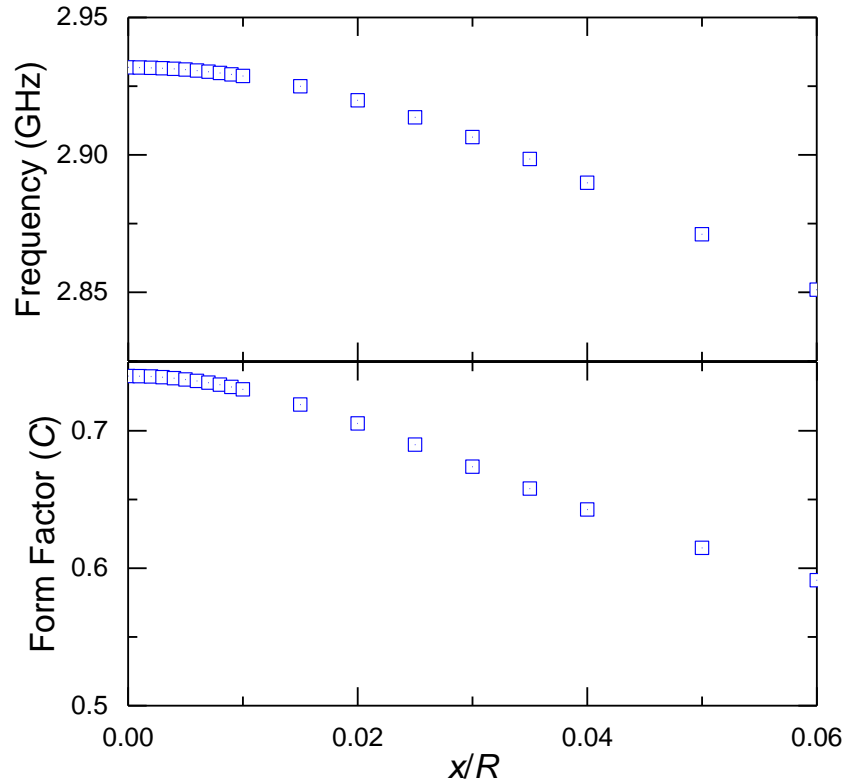


Figure 3-7. Plot of the TM_{010} (top) frequency and (bottom) form factor as a function of tuning rod displacement for a circular cylindrical cavity. Displacement is shown on the x -axis as distance from the center axis (x) over the cavity radius (R). The plot shows f_{010} and C_{010} decrease as the tuning rod moves away from the axis.

When multiple tuning rods are used in a microwave cavity, breaking discrete transverse symmetry can reduce the form factor of a search mode considerably. Figure 3-8 shows images of the E_z field through a cross-section of two cavities with multiple conducting tuning rods, shown as white circles. A cavity with two rods is shown with (a) symmetry maintained and (b) symmetry broken, and a cavity with seven rods is shown with (c) symmetry maintained and (d) symmetry broken. The localization of the electric field when the symmetry is broken results in a form factor that is $\sim 3/4$ the form factor when the symmetry is maintained.

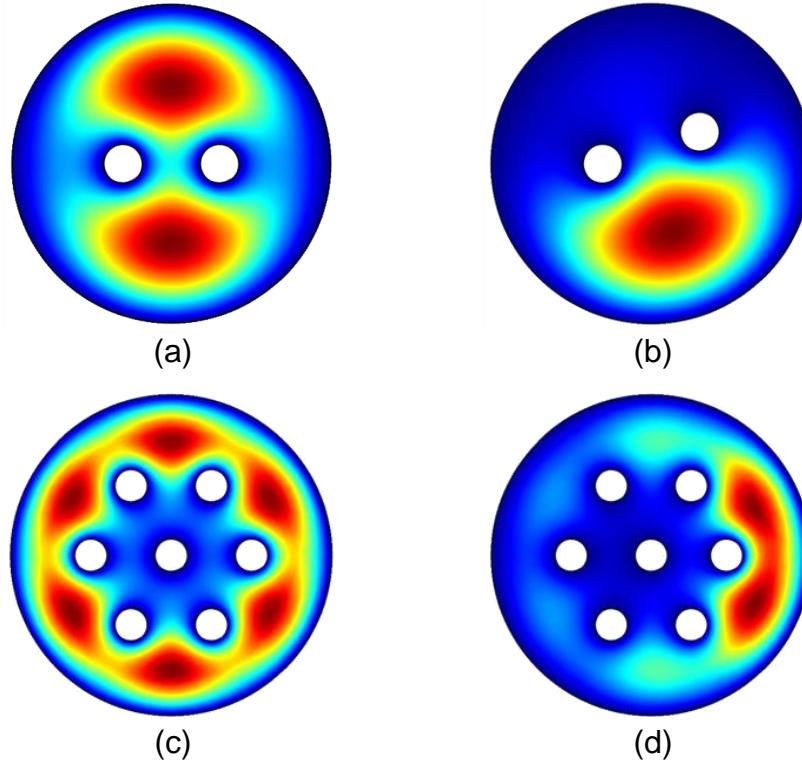


Figure 3-8. Cross-sectional images of the E_z field for the TM_{010} mode in a cylindrical cavity with multiple conducting rods. (a) Two rods maintaining discrete transverse symmetry. (b) Two rods with broken transverse symmetry. (c) Seven rods maintaining discrete transverse symmetry. (d) Seven rods with broken transverse symmetry. The cross-section is parallel to the cavity axis. The white areas are the location of the conducting rods; a field solution is not included in the images as there is zero field inside the conductor. The outer edge of the images and white areas are the conducting boundaries. Red indicates higher field and blue indicates lower field with zero field at the boundaries. Localization of the fields reduces C to $\sim 3/4$ the form factor with symmetry maintained.

Multiple tuning rods can produce unexpected changes in the TM_{010} frequency when symmetry is broken. For both cases of symmetry breaking shown in Fig. 3-8, the breaking decreases f_{010} , though the one tuning rod is moved away from the axis in the cavity with two rods, and one tuning rod is moved toward the axis in the cavity with seven rods. When multiple tuning rods are used, numerical analysis is almost always required to evaluate tuning and symmetry breaking effects.

Transverse symmetry breaking also causes degeneracy breaking. The eigenfunction solutions with subscript $m > 0$ contain two indistinguishable degeneracies with plus/minus polarization about the axis of the circular cylinder. The modes have no preferred orientation, but the degeneracies are oriented 90° about the axis relative to each other to maintain orthogonality. Breaking rotational invariance localizes the fields of the degenerate modes in differing ways, causing the modes to have distinct solutions and preferred orientations. The two modes have different peak frequencies.

Figure 3-9 shows images of the E_z field through a cross-section of a cylindrical cavity with two conducting tuning rods (white circles) for the TM_{110} modes. The cavity has 180° rotational invariance. The modes are degenerate when the cavity maintains 90° rotational invariance, but in the configuration shown, the degeneracies are lifted. Though the tuning rods are at the edge of the cavity where they have the smallest effect on the modes, the frequencies of the modes vary considerably: (a) $f_{110}R = 16.30$ GHz-cm; (b) $f_{110}R = 20.62$ GHz-cm. When the tuning rods are located closer to the center of the cavity, the degeneracy breaking is greater, and the modes are more distinct with a greater relative difference between frequencies. Note, the variable $f_{nm0}R$ for TM modes can be scaled to any cavity size by dividing by the cavity radius [16].

With multiple tuning rods, degeneracy breaking can affect higher-order modes in unexpected ways. Figure 3-10 shows images of the E_z field through a cross-section of a cylindrical cavities with two conducting tuning rod (white circles) for the (a) TM_{210} , (b) unknown TM mode, and (c) TM_{020} . The solution set contains only one TM_{210} mode even though there should be a polarized pair. A 90° rotation of the field within the cavity would result in no distinguishable change in the mode. The TM_{020} mode is not obvious

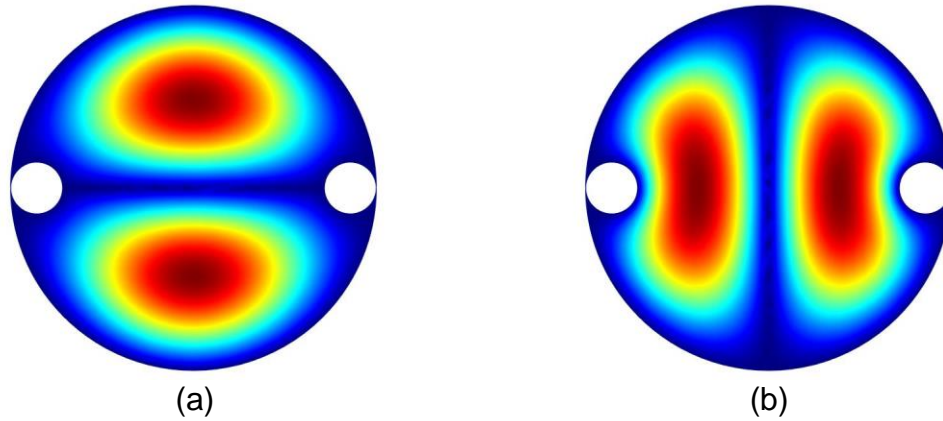


Figure 3-9. Cross-sectional images of the E_z field for the TM_{110} modes in a cylindrical cavity with two conducting rods. The cross-section is parallel to the cavity axis. The white areas are the location of the conducting rods; a field solution is not included in the images as there is zero field inside the conductor. The outer edge of the images and white areas are the conducting boundaries. Red indicates higher field and blue indicates lower field with zero field at the boundaries. The tuning rods break the degeneracy of the modes, resulting in two distinct modes at differing frequencies. An orientation relative to the rods is fixed for both modes.

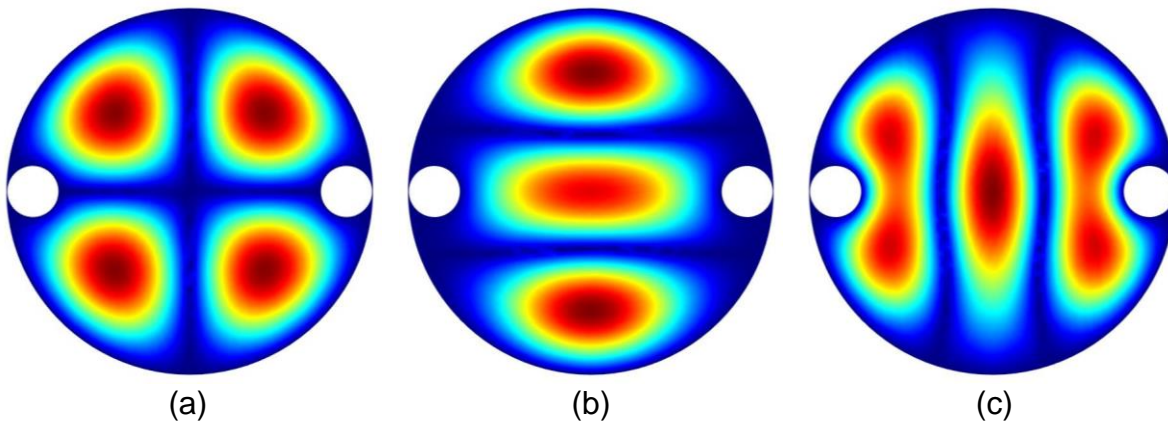


Figure 3-10. Cross-sectional images of the E_z field for higher-order modes in a cylindrical cavity with two conducting rods. (a) TM_{210} . (b) Unknown mode. (c) TM_{020} . The cross-section is parallel to the cavity axis. The white areas are the location of the conducting rod; a field solution is not included in the images as there is zero field inside the conductor. The outer edge of the images and white areas are the conducting boundaries. Red indicates higher field and blue indicates lower field with zero field at the boundaries. The unknown mode appears visually to be a degeneracy of the TM_{020} mode, but is more likely the degeneracy of the TM_{210} mode.

visually, as the shape of the field is considerably different than that of the empty cavity (see Fig. 3-1(c)).

The unknown mode visually appears to be a degeneracy of the TM_{020} mode, though the mode does not have a polarization, as the subscript $m = 0$. The form factor of the unknown mode is 0.054. The form factors of the other modes are $C_{210} = 0$ and $C_{020} = 0.081$. The subscript of the unknown mode could only be determined by finding a closed-form solution to Eq. 3-14 and matching electric field of one solution to the figure.

Sometime localization of the fields from transverse symmetry breaking produces a TM mode with $m > 0$ and $C > 0$ unambiguously. Figure 3-11 shows the images of the E_z field through a cross-section of a cylindrical cavity with two conducting tuning rod (white circles) for the (a) TM_{110} and (c) TM_{020} . The orientation of the rods breaks discrete and continuous rotational invariance. The localization results in $C_{110} = 0.080$ and $C_{020} = 0.037$, where the TM_{110} is more sensitive to the axion for a typical haloscope (see also Fig. 3-30).

For cylindrical cavities with offset dielectric rods, the solution requires an infinite series of Bessel functions of the first and second kind, with diminishing coefficients [91]. To meet the boundary conditions, the electric and magnetic fields are coupled and all modes are hybrid modes. The mode subscripts m , n , and p are still preserved. The field is localized within/about the dielectric. The dielectric always decreases the frequency and form factor of TM_{010} mode, but has varying effects on higher-order modes, much like the conducting rods, requiring numerical analysis to predict the effects.

Figure 3-12 shows images of the E_z field through a cross-section of the cavity with an offset dielectric (alumina) rod for the (a) TM_{010} , (b) TM_{110} , and (c) TM_{020} . The

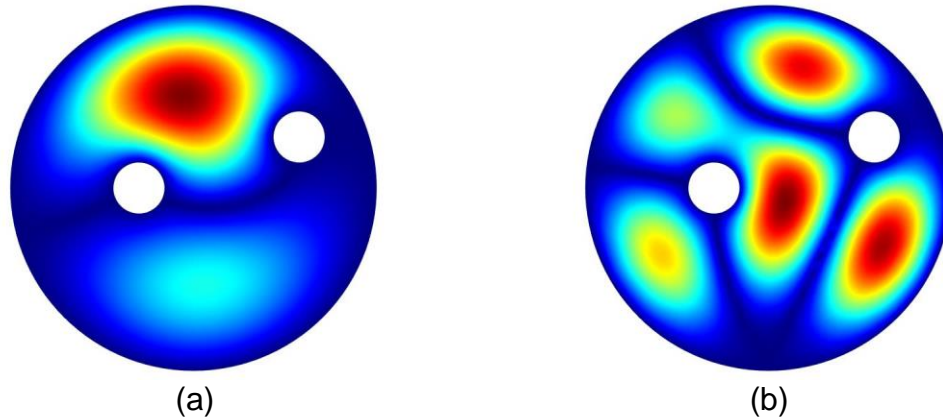


Figure 3-11. Cross-sectional images of the E_z field for modes in a cylindrical cavity with two conducting rods. (a) TM_{110} . (b) TM_{020} . The cross-section is parallel to the cavity axis. The white areas are the location of the conducting rods; a field solution is not included in the images as there is zero field inside the conductor. The outer edge of the images and white areas are the conducting boundaries. Red indicates higher field and blue indicates lower field with zero field at the boundaries. TM_{110} mode has a higher form factor than the TM_{020} mode, though modes with $m > 0$ are conventionally thought to have a form factor of zero.

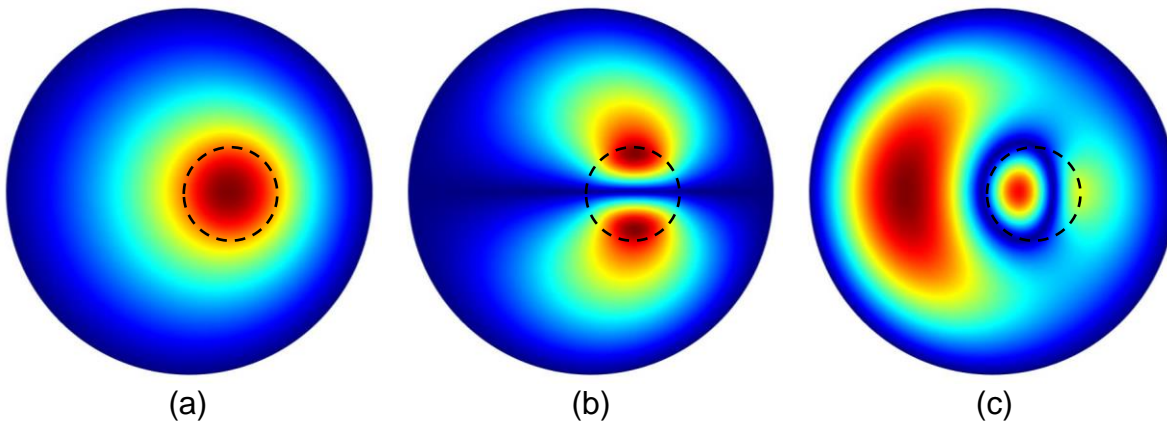


Figure 3-12. Cross-sectional images of the E_z field in a cylindrical cavity with an offset dielectric rod. (a) TM_{010} . (b) TM_{110} . (c) TM_{020} . The cross-section is parallel to the cavity axis and the outer edge of the images are the conducting boundaries. The dielectric rod is outlined by a dotted line. The rod is the same diameter as the rod in Fig. 3-2 ($d = R/2$) and is offset by $R/4$. Red indicates higher field and blue indicates lower field with zero field at the boundaries. The field is localized inside the dielectric.

offset is $x = R/4$. The electric field is localized inside the rod, outlined by a dotted line.

One degeneracy of the TM_{110} mode is shown; the second degenerate mode is less

obvious by visual inspection. The orientation of the TM_{110} is now fixed by the offset of the rod.

Translation of a conducting or dielectric tuning rod will change the frequency of all TM modes in the cavity, but will have no effect on the frequency of the TE or TEM modes. Rod insertion will alter the TE mode frequency some, but considerably less than the change it produces on the TM mode frequencies. As a result, tuning a TM mode across a large frequency range will almost always cause the frequency to match that of a TE or TEM mode. A mode crossing occurs when the frequency of a search mode is the same as the frequency of a non-search mode.

Figure 3-13 shows a plot of the frequency tuning of the TM_{010} mode with a conducting tuning rod through a mode crossing in a circular cylindrical cavity. The frequency of the broken degeneracies of the TE_{215} , and the TM_{011} are also shown. The results are from a FEM simulation conducted with COMSOL version 5.1 [96]. The radius of the model cavity is $R = 6.826$ cm, the length is $5R$, and the tuning rod diameter is $0.532R$. The x -axis is the displacement of the rod from the center axis (x) normalized by the cavity radius. The point where the TM_{010} and TE_{215} modes have the same frequency are mode crossings. It is important to note that mode repulsion, which is discussed below, is not observed.

Longitudinal symmetry breaking compromises translational invariance within a microwave cavity. Localization from longitudinal symmetry breaking has been predicted from the eigenfunction problem [97] as well as finite integration simulations [15]. Longitudinal localization of fields in waveguides and cavities have been less studied than transverse localization due to the complex nature of the solution. However,

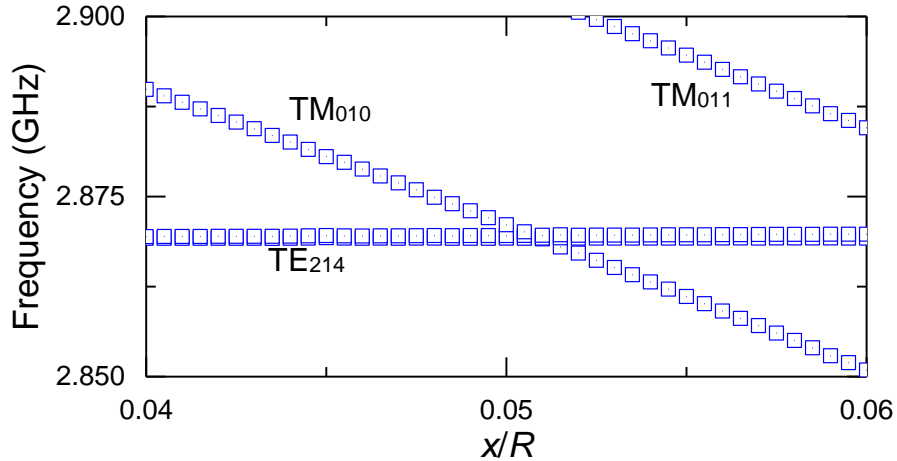


Figure 3-13. Plot of a TM_{010} mode crossing during frequency tuning with a conducting rod for a circular cylindrical cavity. Displacement is shown on the x -axis as distance from the center axis (x) over the cavity radius (R). The plot shows the TM_{010} , the (broken) degeneracies of the TE_{215} , and the TM_{011} modes. The mode crossing occurs where the frequency of the TM_{010} matches that of the TE_{215} mode.

longitudinal localization is more problematic than transverse localization for axion haloscopes [15], and requires in-depth consideration for future searches, especially those at higher frequencies.

Several types of longitudinal symmetry breaking exist in haloscope cavities. The most common type is a discontinuity between the tuning rods and the endcaps. Since the cavity must be tuned to different frequencies, tuning rods used to shift the frequency must be capable of moving within the cavity. If the rod(s) is inserted through an endcap, a mechanical gap will exist between rod-end and the opposing endcap. If the rod(s) translates inside the cavity, a mechanical gap needs to exist between the endcaps and both rod-ends.

Dielectric rod insertion was analyzed by Hagmann et al. [15], quantifying the effects of longitudinal symmetry breaking in cavities with dielectric rods. As the primary focus of this study is conducting axion searches at higher frequencies and dielectric

rods lower the frequency of search modes, longitudinal symmetry breaking with dielectric rods are not reevaluated. See Zaki et al. [90] for modeling discontinuities of dielectric-loaded waveguides.

The mode for a cylindrical cavity with discontinuities at conducting rod-ends can be solved using mode matching techniques [98,99], where each translationally invariant section contains an infinite set of mode solutions consisting of reflective and transmissive parts from the ends of their respective section. Ends that correspond to the endcaps have only a reflective part. Each mode solution has an associated coefficient. The infinite set of solutions for each section are equated together at the transition locations along the z -axis, and the coefficients of the series are solved simultaneously to obtain a complete set of eigenfunctions. In practice, only a finite number of coefficients are solved to obtain a sufficiently accurate solution to the desired modes. The subscripts m , n , and p of the modes are not maintained, but the nomenclature of TM_{mnp} and TE_{mnp} are often used in microwave cavities, as the modes are commonly perturbed versions of the TE/TM_{mnp} solutions.

For TM modes, the mechanical gap between a rod-end and an endcap acts as a capacitor. Electric currents oscillate in the longitudinal direction along the surface of the rod. At each oscillation, an electric potential is built up at the rod discontinuity, as the charge is attracted to the endplate, forming a capacitive effect [100]. The potential results in localizing the electric field.

Figure 3-14 shows images of $|\mathbf{E}|$ for the TM_{010} mode through a cross-section in the x - z plane of the coaxial cavity with (a) translational invariance maintained and (b) translational invariance broken by discontinuities (mechanical gaps) of the center rod

(white area). The endcaps are located at the top and bottom of the image and the cavity wall bounds the left and right side. The diameter of the conducting rod is $d = R/2$, the cavity length is $L = 5R$, and the mechanical gap at both rod-ends for (b) is $g = 0.02L$. The cavity with longitudinal symmetry maintains a constant E field (all E_z) along the z -axis; the cavity with the gap has a varying field along the z -axis. The red area above and below the center rod in (b) illustrate the electric field caused by the electric potential buildup (i.e., capacitive effect). Visual inspection reveals the mode in (a) meets the form of Eq. 3-22, while the mode in (b) does not.

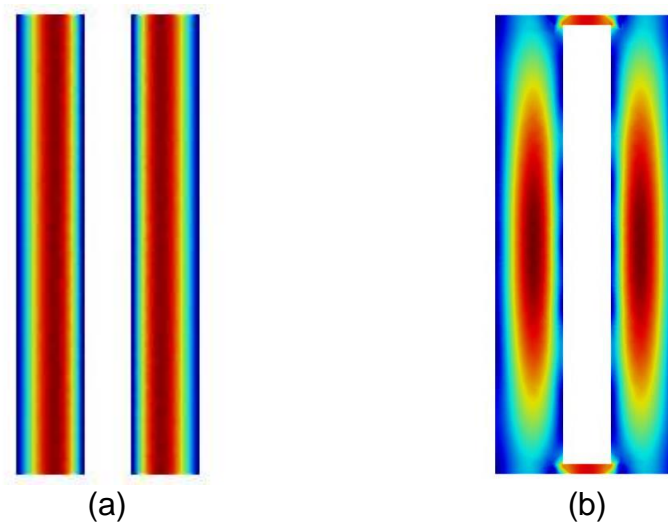


Figure 3-14. Cross-sectional images of $|\mathbf{E}|$ of the TM_{010} mode in a coaxial cavity. (a) Longitudinal symmetry maintained. (b) Longitudinal symmetry broken by discontinuities at both rod-ends. The cross-section is through the x - z plane. The white area is the center conductor; the outer edge of the image and the white area are the conducting boundaries. Red indicates higher field and blue indicates lower field. The interface between the endplate and the center conductor in (a) is not distinguished. The localization of the electric field due to the capacitive effect is shown in red above and below the center rod in (b).

When the frequencies of two modes are reasonably close, the longitudinal symmetry breaking will often cause the modes to mix. The mixing breaks the mode purity, forming a pair of hybrid modes. As a tuning rod is translated or inserted in a

manner that would otherwise bring the frequencies of the two modes together, the mode mixing increases, further breaking the mode purity and causing the two modes to take on similar form. As this happens, the two modes do not come to the same frequency, but instead maintain some inequality through what would be a mode crossing in a longitudinally symmetric cavity. This phenomenon is called “mode repulsion” [15,101].

Figure 3-15 shows plots of (top) mode frequencies and (bottom) form factor verses tuning rod displacement for a mechanical gap at both ends of (a) $g = 0.001L$, (b) $g = 0.003L$, and (c) $g = 0.005L$ from a FEM of a circular cylindrical cavity. The simulation was conducted using COMSOL version 5.1 [96]. The radius of the model cavity is $R = 6.826$ cm, the length is $5R$, and the tuning rod diameter is $0.532R$. The x -axis is the displacement of the rod from the center axis (x) normalized by the cavity radius. The detector magnetic field is assumed to be homogeneous and in the z -direction for computing C .

The frequency plots show the frequency of the TM_{010} , the TM_{011} , and the degenerate TE_{215} modes, as labeled. The modes are not true TE/TM_{mnp} modes, but perturbed forms of the modes. The nomenclature is most commonly used, though TE/TM_{mnp} -like better describes the true nature of the modes. Data shown in the plots are partial to reduce computation time; the plot scales are the same for comparison purposes.

The plots depict several important characteristics of longitudinal symmetry breaking. First, mode repulsion is observed in all plots. As the TM_{010} and TE_{215} mode are brought closer in frequency due to the translation of the tuning rod away from the axis, one of the broken degeneracies of the TE_{215} begins to change frequency with

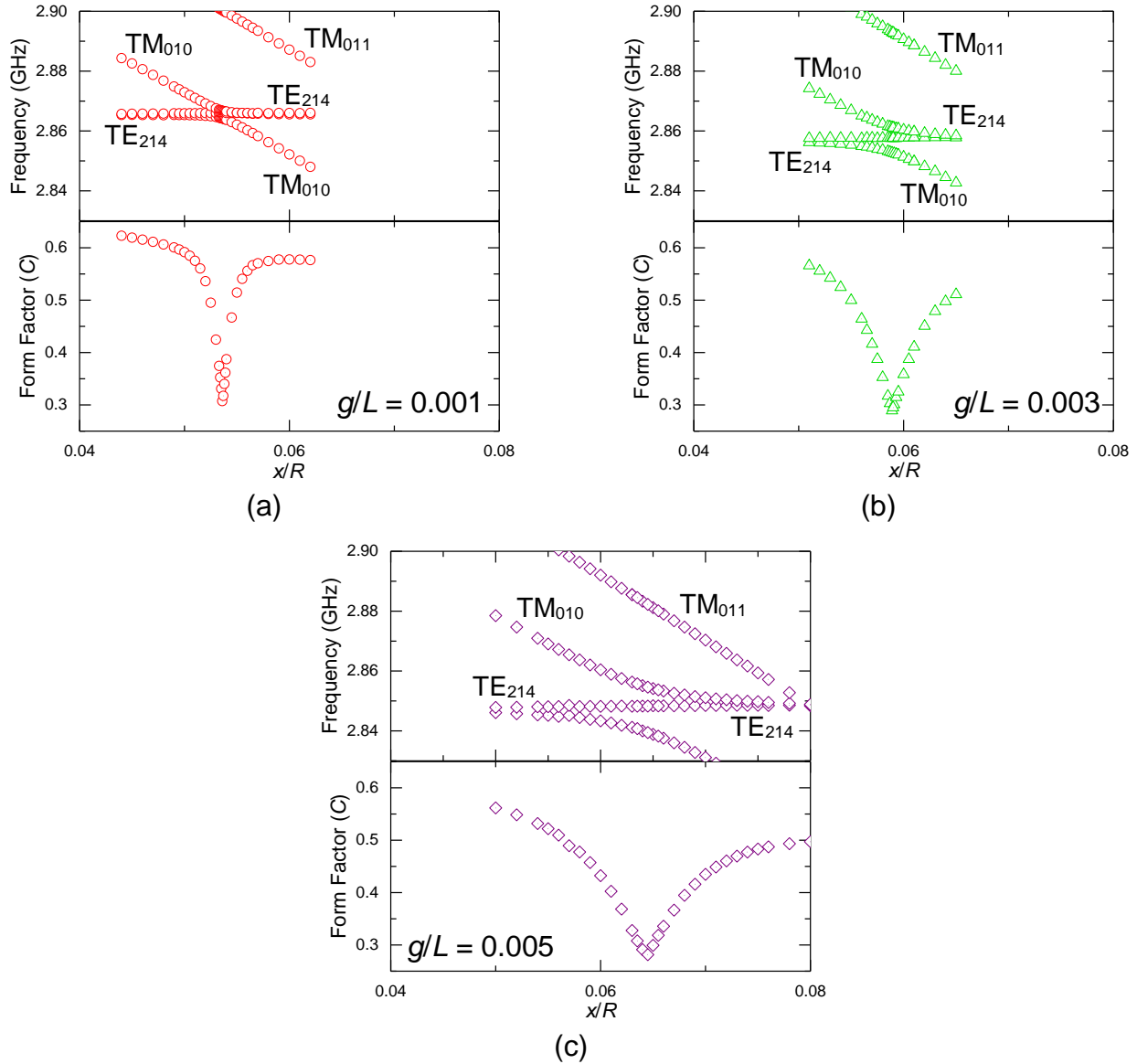


Figure 3-15. Plots of (top) mode repulsion and (bottom) search mode form factor for a circular cylindrical cavity with a discontinuous conducting tuning rod. (a) Mechanical gap of $0.001L$. (b) Mechanical gap of $0.003L$. (c) Mechanical gap of $0.005L$. Displacement is shown on the x -axis as distance from the center axis (x) over the cavity radius (R). The frequency plot shows the TM_{010} , the (broken) degeneracies of the TE_{215} , and the TM_{011} modes, as well as the TE/TM hybrid modes through the mode-repulsion phase. The form factor plot shows the form factor of the search mode (C_{010}) through the tuning; all other form factors are approximately zero.

tuning rod displacement. The change is away from the TM_{010} frequency leading to the term mode repulsion; the TM_{010} repels the TE_{215} in the frequency spectrum, keeping

some difference between them and avoiding a mode crossing. When this occurs, the rate of change of the TM_{010} frequency with a change in rod position decreases. This is depicted in the plot by the curving of the TM_{010} frequency trace near the TE_{215} trace.

This phenomenon is due to the two modes mixing. When the mode frequencies are close enough, the electric and magnetic fields in the two modes couple slightly within the localizations caused by longitudinal symmetry breaking. The two modes become hybrid modes, breaking TE/TM purity. As the tuning rod is displaced to bring the mode frequencies closer, the mixing increases, further breaking TE/TM purity more. At the point of maximum repulsion, the two modes take on similar form (see Fig. 3-16).

As the tuning rod is further translated away from the axis, the mixing of the modes decreases. However, the mode that is the TM_{010} on the left side of the plot now transforms into a TE_{215} -like mode, and the mode is the TE_{215} on the left side of the plot transforms into a TM_{010} -like mode. When the tuning rod is translated to a point where the frequencies of the two modes are sufficiently different, the mode return to pure TE/TM modes, but with the once TM_{010} mode transforming fully into a TE_{215} mode and the once TE_{215} transforming fully into TM_{010} .

Though the hybrid modes do not cross (i.e., match frequencies) within the mode repulsion phase of the tuning, it is convention to classify the mode repulsion as a mode crossing. For purposes of clarity, the mode repulsion phase will be identified as such to distinguish this phenomenon from a mode crossing without mode mixing as depicted in Fig. 3-13.

The plots show that any longitudinal symmetry breaking from a rod-end gap will cause mode mixing, and the larger symmetry breaking (i.e, gap size), the greater the

repulsion and, thus, mixing (see Fig. 3-17). Further, only one of the two TE degeneracies mix with the TM mode. This is true for all TE-TM mode mixing; only one TE mode and one TM mode will mix. If degeneracies exist, one degeneracy will maintain mode purity. The mechanism for selecting which broken degenerate mode mixes is not fully understood, but is related to the broken degeneracies and the TM mode configurations at the localizations.

In the cases shown in the Fig. 3-15, the degenerate TE_{215} mode that does not mix also does not change frequency. As the mode is a pure TE mode throughout the repulsion phase, it will not be significantly detectable with a probe antenna. It is important to note that transverse symmetry breaking does not cause mode repulsion; mode repulsion is a specific result of longitudinal symmetry breaking only. Further, the quality factors of the modes do not alter the mode repulsion, and increasing Q will not reduce the negative effects of the phenomenon discussed below.

The mechanical gap decreases the frequency of TE_{215} modes and slightly increases the frequency of the TM modes in the plots. The gap increases the effective length of the cavity which decreases the frequency of any mode with $p > 0$ (see Eq. 3-16). The gap decreases the effective radius of the cavity which increases the frequency of all modes. Since the TM modes are perturbed form of modes with $p = 0$, only the radius change has an effect, and their frequencies are slightly increased by the gaps. The TE modes are a perturbed form of a $p = 4$ mode, so the length change effect is approximately four time greater than the radius change effect, resulting in a decrease in the frequency larger than the change observed in the TM modes. The changes in frequencies cause the repulsion phase to move to the right in the plots as the

mechanical gap is increased. Different modes will have different frequency responses to the gaps, depending on the p -value of the mode.

Another important characteristic of longitudinal symmetry breaking in haloscope cavities is the discrete transition of the search mode. The form factor plots show the highest form factor of the modes in the corresponding frequency plot. The form factor of the TM_{110} mode and the non-mixing TE_{215} mode are approximately zero in the plots. The form factor of the TM_{010} mode when the mode is not mixed is $\sim 0.5-0.6$ and the form factor of other degenerate TE_{215} mode is about zero. However, in the mode repulsion phase, due to the two modes mixing, the form factor of the TE_{215} mode increase and the form factor of the TM_{010} mode decrease as the tuning rod is moved away from the center axis.

At the point of maximum repulsion, the form factors of the two modes are equal. As the tuning rod is moved further from the axis, the form factor of the mode that is the TE_{215} mode in the left side is the largest, and this mode becomes the search mode. To accomplish this change, the measurement frequency must be instantly changed from one mode frequency to the other and continue scanning with the new mode, causing a hole in the frequency search spectrum (see Fig. 3-16) [15]. The form factor of the hybrid modes at the point of maximum repulsion is $C = \sim 0.3$ for all gap sizes evaluated, suggesting the gap size has almost no effect on the minimum form factor due to mode mixing.

The transition of the search mode from one hybrid mode to the other causes the V-shape in the form factor plots. As the mechanical gap size increase, the width of the V increases, resulting in a reduced form factor over a larger frequency span. Thus, a

larger mechanical gap typically leads to a less effective microwave cavity for axion searches. Further, reviewing the frequency and form factor plots simultaneously reveals a larger mechanical gap size causes a larger hole in the frequency search spectrum.

Figure 3-16 is a replot of Fig. 3-15(c) identifying the hole in the frequency search spectrum caused by the mechanical gaps at the rod-ends, $g/L = 0.005$. The difference in frequency between the two hybrid modes when their form factors are identical is the hole size, denoted as Δf . The scale of the plot has been changed from Fig. 3-15 to emphasize the hole.

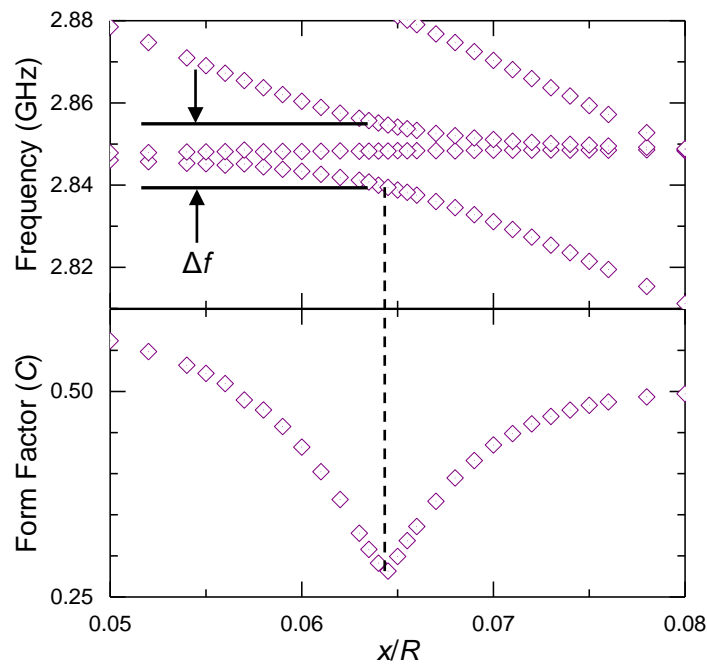


Figure 3-16. Plots showing the hole in the frequency search spectrum produced by longitudinal symmetry breaking. The plot shows the (top) frequency and (bottom) search mode form factor through the mode-repulsion phase for a circular cylindrical cavity with a discontinuous conducting tuning rod, $g/L = 0.005$. The plot is the same as Fig. 3-15(c) with the scale adjusted to emphasize the hole. The dotted line indicates the rod displacement at the point of maximum repulsion. The hole in the spectrum is Δf .

The degradation of C as well as the mode repulsion is a result of the mode mixing. Mode crossings without mode mixing does not degrade the sensitivity of a

haloscope detector like mode repulsion, though it can make mode identification more challenging if the crossing mode is detected by the instrumentation (see Chapter 3.3). When longitudinal symmetry is maintained, mode repulsion does not occur; mode tuning that does not break longitudinal symmetry thus will never experience a loss in C at mode crossings (see Chapter 3.4).

In reality, an axion search will stop scanning prior to the point of maximum repulsion, tune the cavity beyond the point, and continue scanning on the new mode. This procedure is done because the simulation cannot perfectly predict the form factor of the modes, so additional precautions must be made to ensure a scan is not conducted with a mode that has a negligible form factor inadvertently. Thus, the actual size of the hole in the search spectrum will always be greater than Δf .

Figure 3-15 demonstrates that a larger mechanical gap causes a greater Δf . Figure 3-17 shows a plot of Δf , normalized by the mode frequency versus gap size for the cavities modeled in Fig. 3-15. At small gap sizes, $\Delta f/f \approx g/L$ for the cavity modeled.

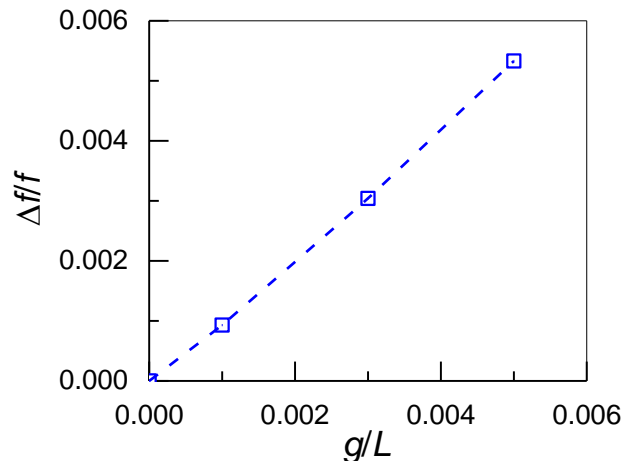


Figure 3-17. Plot of hole in frequency search spectrum as a function of rod-end gap size. Gap size is normalized by the length of the cavity and the frequency hole is normalized by the search mode frequency. For a single tuning rod of diameter $\sim R/2$, $\Delta f/f \approx g/L$ at small gaps.

Figure 3-18 shows images of $|\mathbf{E}|$ and the \mathbf{E} vectors for the (left) lower frequency hybrid, (middle) non-mixing degenerate TE mode, and (right) higher frequency hybrid mode in a cylindrical cavity at the point of maximum repulsion. The cross-sections are through the (top) x - z plane and (bottom) y - z plane of the cavity. The mechanical gap of the ends of the tuning rod (white area) is $g = 0.005L$. The geometry of the cavity is identical to that of Fig. 3-15. The black arrows show the \mathbf{E} vectors; the location of the vector origin is the tail of the arrow.

The mode configuration in the x - z plane of the lower and upper hybrid (TM_{010} -like) modes, Fig. 3-18(a) and Fig. 3-18(c), are notably similar. The left side of both images appear to be opposing hybrid modes while the right side appears to be mirrored TE-like modes. The mode configuration in the x - z plane of the hybrid modes, Fig. 3-18(d) and Fig. 3-18(f), also have similar configurations, both appearing TM-like, though the E_z field in the lower frequency mode is observably stronger. The contrasting configurations of the modes are like that of broken degeneracies. Vectors that are into the page are not seen, so \sim half of the vectors for the hybrid modes in the x - z plane are not visible.

The mode configuration of the TE_{215} demonstrates mode purity in both planes. The vectors are projected onto a plane, so the in/out-of-plane magnitude is not depicted. The vectors in Fig. 3-18(b) are in or out of the plane, so appear as dots or are not shown in the image. The mode configure does not significantly change with translation of the tuning rod.

Currently no common nomenclature of a hybrid mode in haloscope cavities exists. Most often the search mode is to call the TM_{0n0} , though it is neither a pure TM

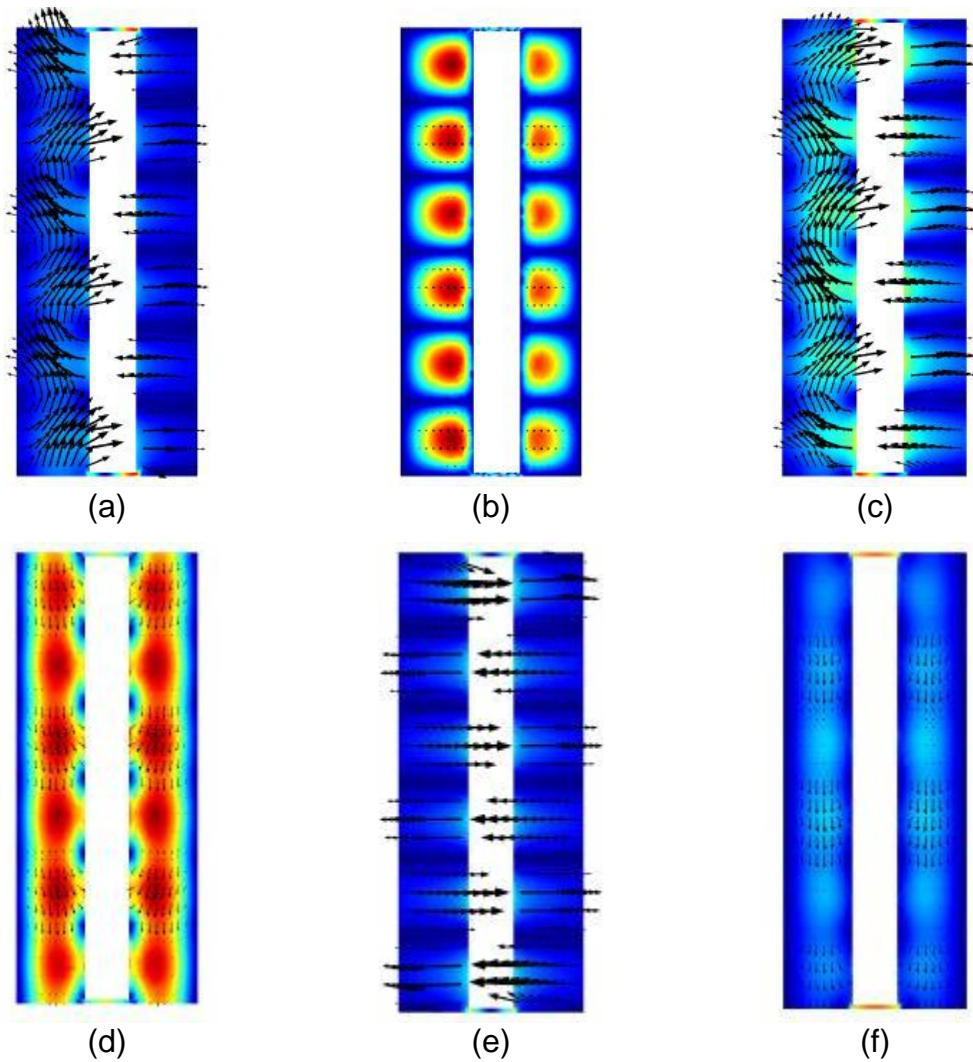


Figure 3-18. Cross-sectional images of $|\mathbf{E}|$ with \mathbf{E} vectors of the hybrid modes and the TE_{215} mode at the point of maximum mode repulsion in a cylinder cavity. (a) and (d) Lower frequency TM_{010} -like. (b) and (e) TM_{215} . (c) and (f) Higher frequency TM_{010} -like. (a)-(c) Cross-sections through the x - z plane. (d)-(f) Cross-sections through the y - z plane. The white area is the center conductor; the outer edge of the image and the white area are the conducting boundaries. Red indicates higher field and blue indicates lower field. The electric field vector is depicted by the black arrows originating from the tail of the arrow. The hybrid (TM_{010} -like) modes are not pure TE/TM modes.

mode nor are the subscript m , n , and p of any meaning mathematically. Sometimes the modes are given a “-like” suffix (as done herein), but this doesn’t distinguish them from the non-hybrid modes. During the mode repulsion phase, mode mixing makes mode

identification extremely difficult as the hybridization make different parts of the mode appears as different mode types, as seen in Fig. 3-18.

Perhaps for this reason, hybrid modes in waveguides are sometimes indicated by H_{mnp} . But when m , n , and p subscripts lose meaning, such as in the mode repulsion phase, even this method is insufficient. Hybrid mode in waveguides where complex mixing occurs are sometime designated H_i , where i simply indicates the number of the hybrid mode, counting by frequency from the lowest frequency mode; H_1 indicates the lowest frequency hybrid mode. In general, there is no universally agreed upon nomenclature for hybrid modes in waveguides or cavities.

Degeneracy breaking of modes due to longitudinal symmetry breaking causes additional modes to exist within a given frequency range of a microwave cavity. In addition, reentrant modes appear in the mechanical gaps and evanescent modes will form. The result is modes will cluster closer together and increase in mode density about a search mode, causing mode crowding. Debate still exists as to whether the modes are formed from the symmetry breaking, or if the modes existed at much higher frequencies prior to the breaking and were greatly reduced due to the breaking.

The mode crowding interferes with identifying and tracking a search mode (see Chapter 3.3). Additionally, mode crowding increases the number of mode repulsion type crossings across a frequency scan, further degrading the capability of a detector. Figure 3-19 shows the nearest 15 modes to the TM_{010} mode, plus the TM_{010} , from a FEM simulation of a cylindrical cavity with the tuning rod along the center axis for various mechanical rod-end gaps. The radius of the cavity is $R = 6.826$ cm, the length is $5R$, and the tuning rod diameter is $0.532R$.

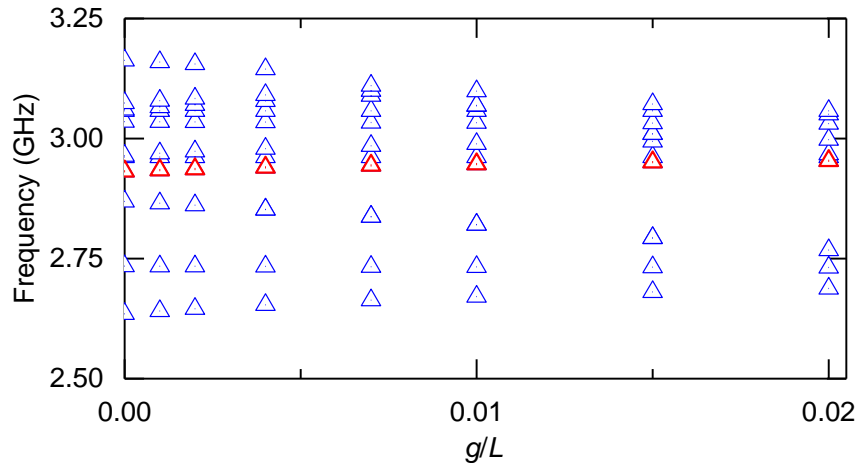


Figure 3-19. Plot showing mode crowding due to increased mechanical gap at the rod-ends. At each gap size with data, 16 modes are shown; the TM_{010} mode is in bold red. The tuning rod is located along the center axis. Gap size is normalized by the length of the cavity. As the gap is increased, mode density increases.

At each mechanical gap with data, a total of 16 modes are shown (vertically), though some modes are too close in frequency to distinguish visually. Each gap size represents a single eigenfunction solution of 16 modes about, and including, the TM_{010} mode (bold red). The simulation was conducted using COMSOL [96] version 5.1. Because exactly 16 modes are solved for in each run, mode crowding is revealed as the frequency span across the modes shrinking. The mode density is clearly greater on the right side of the plot than the left.

The mode crowding is caused by reentrant and/or evanescent modes existing near the TM_{010} mode, when they were not found at smaller gaps, and degeneracy breaking of nearby modes. In general, mode crowding will be observed at almost any frequency when a mechanical gap is introduced; the TM_{010} mode is only used as a reference point in the plot. Two distinct clustering of modes is seen; the mechanism for the separation into two clusters is unknown.

A second significant symmetry breaking in tuned microwave cavities is misalignment of the tuning rod relative to the cavity boundary, or “tilt.” Tilting of the tuning rod is a more complex symmetry breaking, as it breaks both transverse and longitudinal symmetry simultaneously. In theory, the mathematical method used to find the eigenfunction solutions for modes in tuned cavities with mechanical gaps could be used to find the solutions for cavities with a tilted tuning rod, but the summation would need to be replaced with an integration. However, no such mathematic formulation has been established to date. Instead, eigenfunction solutions are found with a finite-element (or similar) type computer simulation.

Mode localization due to rod tilt is dependent on the displacement of the rod. Figure 3-20 shows images of $|\mathbf{E}|$ for the TM_{010} mode through a cross-section in the x - z plane of a cylindrical cavity with longitudinal symmetry broken by a 1.0° of the tuning rod (white area) with (a) no displacement from the center axis and (b) a rod displacement of $R/100$ in the x -direction. The endcaps are located at the top and bottom of the image and the cavity wall bounds the left and right side.

When the rod is not displaced from center of the cavity, symmetry breaking is done by the tilt alone and the mode takes on a discrete antisymmetric form in the longitudinal direction. A small displacement of the rod breaks the anti-parity and the localization moves to one section of the cavity, greatly diminishing the form factor. Visual inspection reveals the modes do not meet the form of Eq. 3-22.

Symmetry breaking from tuning rod tilt manifests mode repulsion and the associated reduction in form factor as seen with mechanical gaps. Figure 3-21 shows plots of (top) mode frequencies and (bottom) form factor verses tuning rod displacement

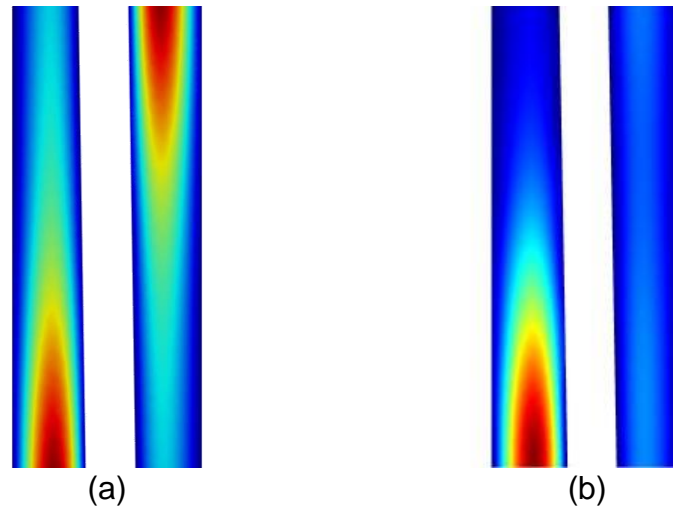


Figure 3-20. Cross-sectional images of $|\mathbf{E}|$ of the TM_{010} mode in a tuned cavity with a rod tilt (angular misalignment). (a) No transverse displacement of the rod. (b) Transverse displacement of the rod of $x = R/100$. The cross-section is through the x - z plane. The white area is the center conductor; the outer edge of the image and the white area are the conducting boundaries. Red indicates higher field and blue indicates lower field. The interface between the endplate and the center conductor is not distinguished.

for a tuning rod tilt of (a) $\varphi = 0.25^\circ$, (b) $\varphi = 0.50^\circ$, and (c) $\varphi = 1.00^\circ$ from a FEM of a for a circular cylindrical cavity. The simulation was conducted using COMSOL version 5.1 [96]. The radius of the model cavity is $R = 6.826$ cm, the length is $5R$, and the tuning rod diameter is $0.532R$. The x -axis is the displacement of the rod from the center axis (x) normalized by the cavity radius. The detector magnetic field is assumed to be homogeneous and in the z -direction for computing C .

The plots demonstrate many of the same characteristics of Fig. 3-15. Any longitudinal symmetry breaking from a rod tilt will cause mode mixing and mode repulsions. In all cases shown, the mode hybridization characteristics observed with the mechanical gap are observed with the rod tilt. However, the mixing is less severe than that experienced with mechanical gaps. In particular, the mode repulsion is not even visible in Fig. 3-22(a). Only through observing the form factor of the modes does the

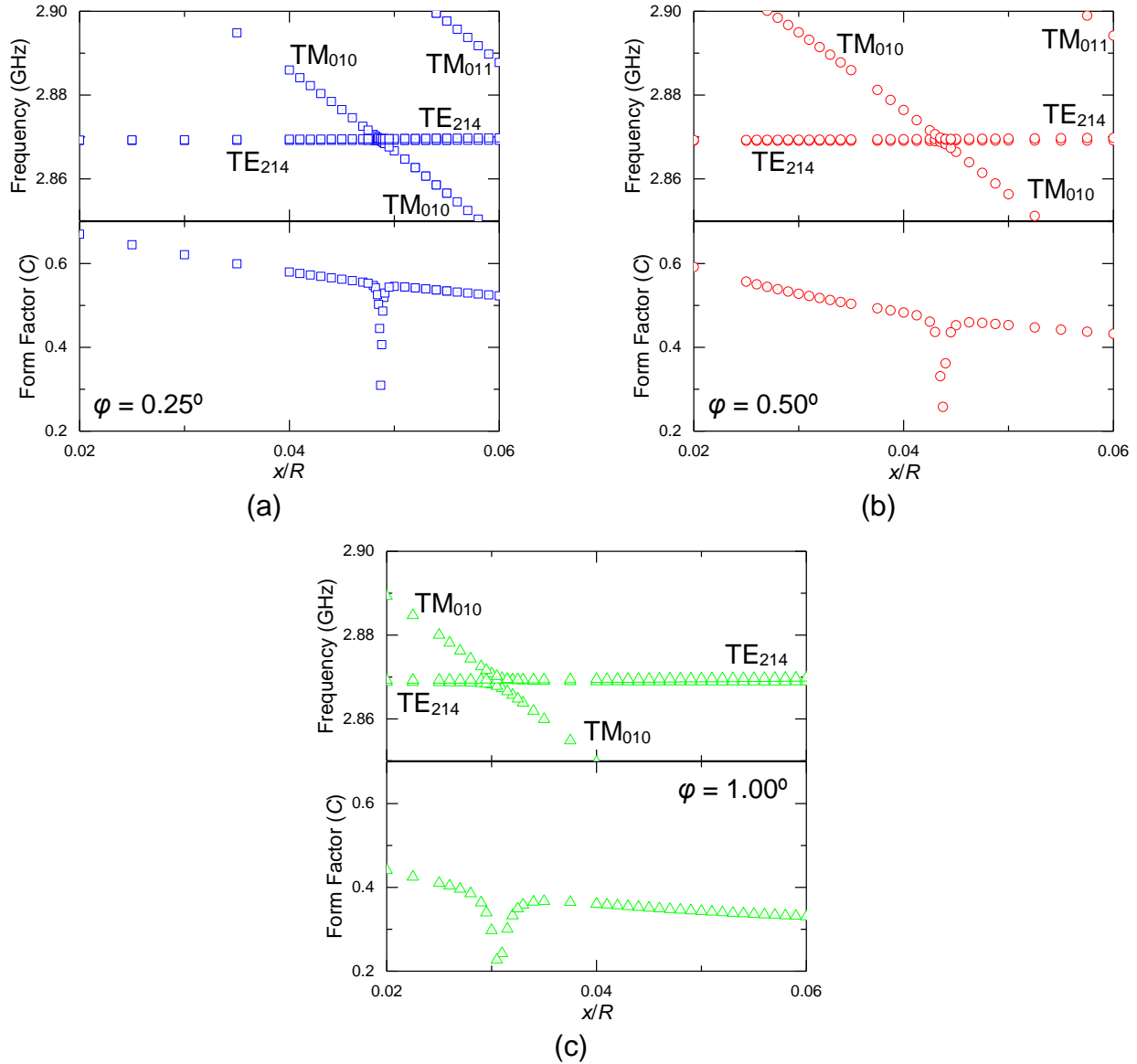


Figure 3-21. Plots of (top) mode repulsion and (bottom) search mode form factor for a circular cylindrical cavity with a tilted conducting tuning rod. (a) Tilt of 0.25° . (b) Tilt of 0.50° . (c) Tilt of 1.00° . Displacement is shown on the x-axis as distance from the center axis (x) over the cavity radius (R). The frequency plot shows the TM_{010} , the (broken) degeneracies of the TE_{215} , and the TM_{011} modes, as well as the TE/TM hybrid modes through the mode-repulsion phase. The form factor plot shows the form factor of the search mode (C_{010}) through the tuning; all other form factors are approximately zero.

mode mixing and thus repulsion become apparent. As a result, the hole in the frequency search spectrum and the width of the form factor degradation is considerably smaller.

Contrary to the mode repulsion effects, the reduction in form factor is more extreme from the conducting rod tilt, which could be predicted from the mode configurations seen in Fig. 3-20. As the tilt is increased, the form factor across the frequency range decrease considerably, until $C \approx 0.4$ for a tilt of $\varphi = 1.00^\circ$ even when the TM_{010} is not in the mode repulsion phase. At the point of maximum repulsion, the form factor is $\sim 0.2-0.3$, similar to Fig. 3-15.

At a tilt above $\sim 1.00^\circ$, mode configurations and interactions become complex. Figure 3-22 shows plots of (top) mode frequencies and (bottom) form factor verses tuning rod displacement for a tuning rod tilt of $\varphi = 1.80^\circ$ from a FEM of a circular cylindrical cavity. The simulation was conducted using COMSOL version 5.1 [96] and the cavity parameters are the same as Fig. 3-21.

The TM_{010} and TE_{215} mode enter mode repulsion as soon as the tuning rod is moved from the center axis. At $x/R \approx 0.01$, the TM_{010} mode is no longer mixing with the TE_{215} mode. The TM_{010} continues to decrease as the tuning rod is moved away from the center axis, maintain a form factor of ~ 0.3 . The next higher mode, labeled TM_{010} -like, initially increases with tuning rod displacement and has a form factor of about zero. The form factor of the mode increase as the rod moves away from the center axis, until obtaining a C approximately the same as the TM_{010} mode at $x/R \approx 0.02$. The form factor of the TM_{010} -like continues to increase until $x/R \approx 0.04$. Then the mode's frequency and form factor decrease with rod displacement.

While the mode's form factor is greater than the form factor of TM_{010} , the mode configuration looks like a separate TM_{010} mode, leading the TM_{010} -like label. The example shown is an extreme case, but demonstrates the complex nature of cavity

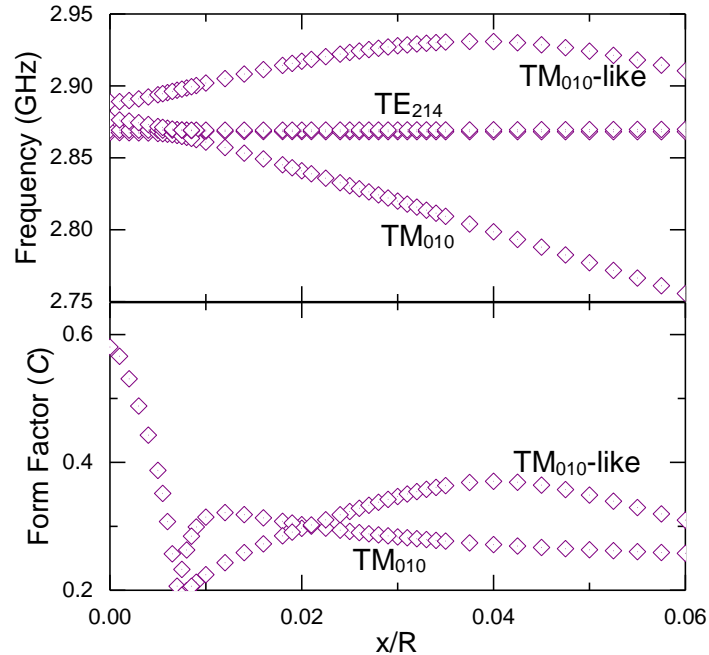


Figure 3-22. Plots of (top) frequency and (bottom) search mode form factor for a circular cylindrical cavity with a conducting tuning rod tilted 1.80° . Displacement is shown on the x -axis as distance from the center axis (x) over the cavity radius (R). The frequency plot shows the TM_{010} , the (broken) degeneracies of the TE_{215} , and a second TM_{010} -like mode, as well as the TE/TM hybrid modes through the mode-repulsion phase. The form factor plot shows the form factors of all modes with $C > 0.2$. The mode interaction is complex.

modes when longitudinal and transverse symmetries are broke, as well as highlights the complication with nomenclature for such modes.

Bending of a tuning rod produces similar effects to tilt. The localization is either near the center of the cavity or near the two ends, depending on the tuning rod bend in relation to the rod displacement. Longitudinal symmetry breaking can also be a result of cavity fabrication or assembly errors. But such symmetry breaking produce insignificant changes to the frequency or form factor of search modes except in extreme cases.

Angular misalignments of an endcaps relative to the center axis would need to be many degrees to produce any noticeable effect. Bowing of the cavity walls would need $a/L \gtrsim$

0.1 to produce any measurable difference, where a is the bow height (maximum distance from the theoretical location to the actual location).

3.3 Mode Identification Methods

Axion searches with a haloscope detector must be conducted with modes that are sufficiently sensitive to the particle conversion (i.e., have a large enough C) to achieve a possible detection. At each tuning rod configuration, an infinite number of modes exist while only a very small number of modes will yield any statistical probability of a detection within a feasible time frame. In theory, a threshold for a minimum form factor of a search mode could be determined by the cavity parameters (see Eq. 2-10), the frequency range of the mode(s) to be scanned, the desired model sensitivity (see Fig. 2-17), and the available search time.

In practice, the TM_{010} mode has been exclusively used to conduct axion searches, as it nearly always has the highest form factor of any mode. Higher modes have been investigated, but instead of establishing a threshold, the detector sensitivity is established from the available modes and time, and the sensitivity is evaluated for scientific worth. Until recently, no experiment had established sufficient sensitivity with a mode other than the TM_{010} to detect the KSVZ axion.

The form factor of a mode is not directly measurable; there is no current measurement technique that could evaluate the electric field in the entirety of the cavity without significantly disrupting/destroying the field. Absent any preplanning, the signal received from a desired search mode is indistinguishable from signals from any other mode. Thus, mode identification is critical to the success of an axion detector. Further, the search must match the scan frequency of the receiver chain with the frequency of the search mode throughout the cavity tuning range. Mode identification must be

performed repeatedly and rapidly at all times, and mode tracking, staying on the search mode throughout the search, is necessary.

The most common technique used for mode identification is mode mapping. Mode mapping consists of two parts: analytical predictions and cavity measurements. The analytical predictions of mode frequency verses tuning configuration are calculated, typically using computer simulations, throughout the tuning range of the cavity. The predictions will be within a frequency window, usually spanning the lowest frequency of any TM mode to some upper limit established by the search objectives. The predicted form factor and quality factor of each mode is also calculated.

The frequency of the modes is plotted against the tuning configuration parameters of the cavity, forming an analytical mode map. The tuning parameters would be, for example, the angle of rotation against some baseline for rods that rotate or the depth of insertion for rods that are inserted. A 2-dimensional map exists for each tuning parameter, yielding $n+1$ dimensional mapping where n is the number of degrees of freedom. For a cavity with only one tuning rod, the mapping is a single plot; for a cavity with two tuning rods, a 3-dimensional map will result. The display of a 3-dimensional (or higher) map requires slicing the map into 2-dimensional plots by holding all but one parameter constant. The predictions can also be displayed with a color-axis as the form factor, enabling easier identification of search modes, particularly at mode repulsion frequencies.

Figure 3-23 shows an example of analytical predictions from ADMX [100]. The predicted frequency of several modes is shown verses the angular rotation of one tuning rod (θ_2) while the other tuning rod is held fixed (θ_1). Only part of the full tuning

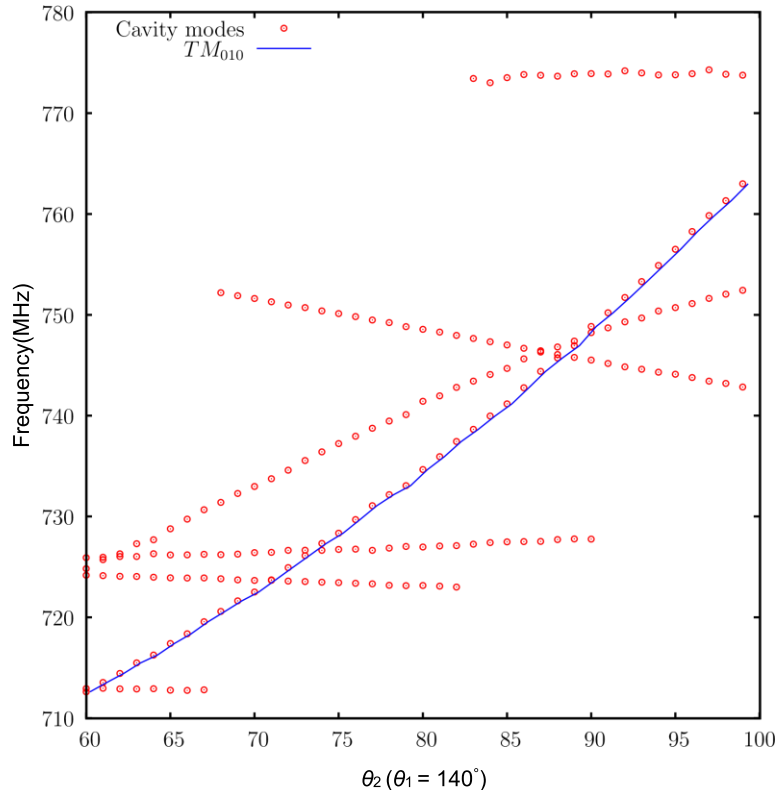


Figure 3-23. Example of frequency predictions from ADMX [102]. The red circles show the predicted frequency while the blue line identifies the predicted f_{010} as determined by C_{010} of the analytical results. One tuning rod is rotated while the other is held fixed. Results are from a 2-dimensional analysis.

range is shown. The red circles show the predicted frequency while the blue line identifies the predicted f_{010} as determined by C_{010} of the analytical results. Several mode crossings are depicted but no mode repulsions are shown, as the simulation assumed longitudinal symmetry.

The cavity measurement mode map is composed from the power spectrum of the cavity at various configurations across the scanning range. The spectrum is obtained from sweeping an injection signal, usually through a weakly coupled port, across a frequency range that bounds the search frequency range of the cavity, and measuring the power through the receiver chain (an S_{12} measurement). The measurements are visually displayed in two forms. One form is a color-plot, with the data shown with the x-

axis as one tuning parameter, the y -axis as the frequency, and the color-axis as the measured power. The second form uses a power threshold, plotting only the frequencies of the peak power that exceed the threshold. Measurement data maps without the predictions are also referred to as a mode maps; maps with analytical predictions should be identified clearly.

The measured data is compared to the analytical predictions to identify the modes of the cavity. The identification method is often performed manually using visual techniques, as misalignments in the cavity make it nearly impossible to bound error in the predictions prior to the mode mapping. Figure 3-24 shows an example of a mode map from ADMX showing both the analytical predictions and the measured data [100], using the threshold method. The analytical data is identical to Fig. 3-23. The red dots are the analytical predictions and the blue asterisks are the measured data.

Mode repulsion is visible at two of the mode crossings of the TM_{010} , around 725 MHz and 745 MHz. Though the 2-dimensional simulation did not predict the mode repulsion, the predictions are accurate enough to identify the TM_{010} . However, a 3-dimensional model is needed to determine where the mode transfer should occur in the mode repulsion phase. Due to prediction errors, the form factor at the mode repulsion is not well bound, requiring a broadening of the frequency hole in search spectrum to avoid scanning with an insufficient form factor. A few false positive mode measurements are also observed as single scattered points.

Mode mapping has been successfully used in haloscope searches historically. However, as searches move into higher frequencies, mode maps become less effective. At higher-order search modes, mode density increases greatly. Using a power-threshold

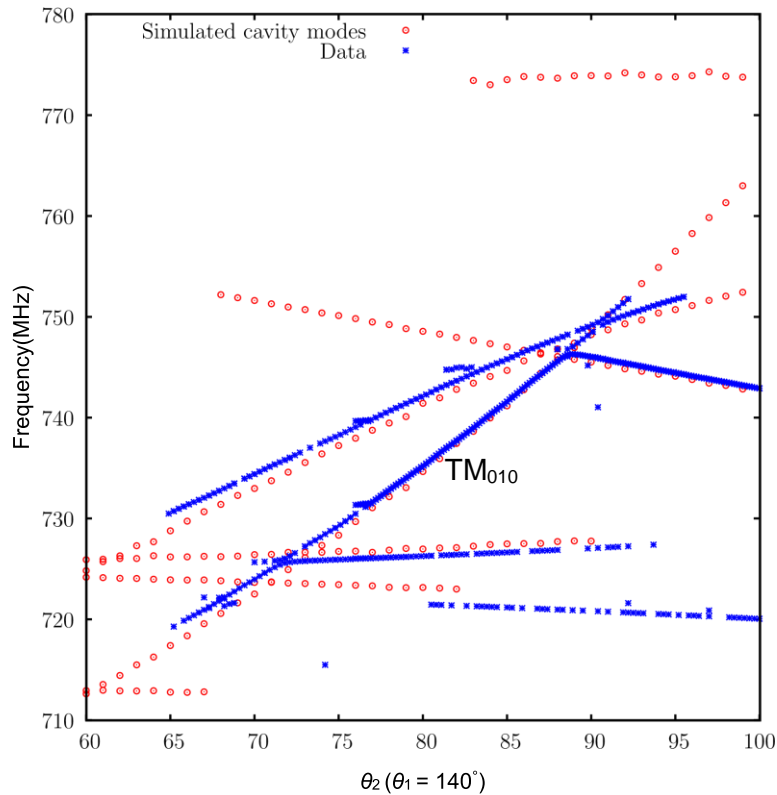


Figure 3-24. Example of a TM_{010} mode map from ADMX [102]. The red circles show the predicted frequency and the blue asterisks are the measured data. One tuning rod is rotated while the other is held fixed. The predictions are accurate enough to identify the TM_{010} .

type map is more useful for mode identification, but can result in data overcrowding, such that modes cannot be sufficiently distinguished from each other for tracking. Additionally, threshold maps often identify false positives or miss the search mode depending on where the threshold is set, further complicating mode identification. A color-plot relieves some of the issues, but is usually too congested to be of much practical use.

Figure 3-25 shows a 2-dimensional mode map, without analytical predictions, of ADMX at the next higher-order search mode above the TM_{010} . The mode was identified as TM_{020} [100], though the subscript is not fully accurate (see Fig. 3-32). The map is very crowded and depicting a search mode, one that yields a viable form factor, over

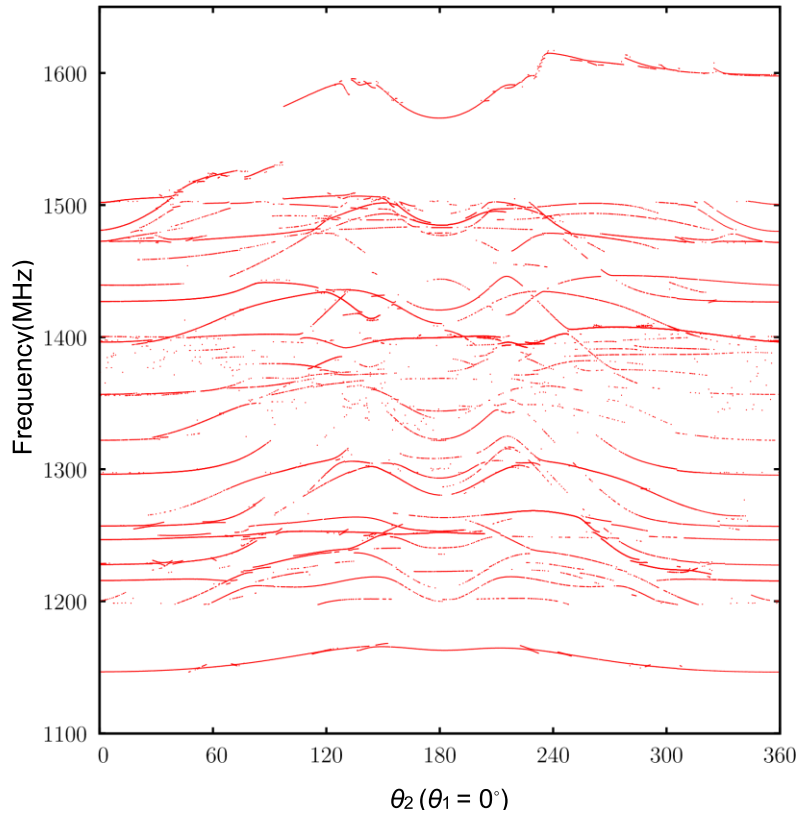


Figure 3-25. Example of a TM_{020} mode map without predictions from ADMX [102]. The red dots are frequency peaks of measured data above a specified power-threshold. One tuning rod is rotated while the other is held fixed. The map is too congested to accurately identify the search mode throughout tuning.

modes with $C \approx 0$, is extremely difficult. Overlaying the analytical predictions makes the map even more complicated and small misalignments or symmetry breakings cause the modes to move too far from the analytical predictions to identify the desired search modes.

Searching higher-order modes is only one of several methods of conducting higher frequency axion searches. Other methods include power-combining multiple smaller cavities or using a greater number of tuning rods (see Chapter 3.4). However, these methods have distinct issues that hinder the effectiveness of mode maps. Smaller cavities are more sensitive to symmetry breaking and mechanical misalignments, causing a greater error in the predictions, especially around mode repulsions. Large

numbers of tuning rods tend to drive the search mode into more mode-dense frequencies, resulting in mode maps like Fig. 3-25. For these reasons, additional mode identification techniques need to be developed for successful axion search at higher frequencies.

The simplest method of mode identification is rod insertion. Inserting a conducting rod a short distance inside the cavity will always increase the TM_{010} mode and will typically increase the frequency of higher-order search modes, though not always (see Chapter 3.2). Rod insertion can help identify the search mode by comparing shifts in the S_{12} measurements of the mode frequency to the predicted shifts from a preexisting analysis. Both the magnitude and the direction of the shift can be used for identification. The method is particularly useful when only two candidate modes exist.

In theory, the rod insertion could be conducted using the receiver antenna of the haloscope antenna. Because the antenna needs to be coupled at different frequencies, a haloscope cavity usually uses an adjustable probe antenna. The antenna could be inserted further to force the frequencies of the modes to shift. However, the insertion of the antenna also changes the coupling and Q_L . A very precise analysis would be required to accurately predict the frequency shifts from the insertion. Characterizing the method prior to a search would be necessary. Alternatively, a separate rod with associated drive system could be used. Some haloscope cavities use such a system as part of their tuning method.

A more sophisticated and robust technique of mode identification is a bead-pull (or bead perturbation) test. A small dielectric or conducting bead is placed inside the

cavity, shifting the frequencies of the modes slightly depending on the local field at the bead. The bead is translated within the cavity, usually by pulling on a nonconducting cord attached to the bead, and multiple S_{12} measurements of the mode frequency verses bead location are taken to map the frequency shift along a straight line. For a small lossless dielectric bead, the frequency shift of any mode can be predicted by [103]

$$\Delta f_{mnp} \approx f_{mnp} \frac{V_b (1 - \epsilon_b) \epsilon_0 |\mathbf{E}|^2}{U}, \quad (3-34)$$

where V_b and ϵ_b are the volume and relative permittivity of the bead, respectively, and \mathbf{E} is the field at the center of the bead.

Mapping the frequency shift of a mode against the location of the bead reveals the relative strength of the field. When the bead is traversed in the z-direction through the length of the cavity, the measurements produce a local profile of the modes. The number of nodes, where $\Delta f \approx 0$, is the value of the subscript p of the mode (or the subscript for the closest TE/TM_{mnp} mode). Using a conducting bead can provide a mapping of the magnetic field.

The measurement can also identify misalignments or other internal issues. For example, a tuning rod tilt will cause Δf to vary linearly with height, where an aligned rod will yield a constant or sinusoidal Δf . The larger the tilt, the larger the variation in Δf . Using the bead-pull test in multiple transverse locations yields a field map of the cavity that can be compared to predictions to validate the analysis and bound errors in form factor. The bead-pull test is the closest check an axion haloscope has to a direct measurement of the form factor. HAYSTAC [104] is currently conducting bead-pull tests to enhance their microwave cavity development program.

Figure 3-26 shows (a) a schematic of a bead-pull test setup and (b) results [105] from a test on an empty cylindrical cavity with a dielectric bead. The red block depicts the bead and the grey line depicts the cord used to translate the bead. The blue arrows indicate the E field of the TM_{010} (not to scale). The black arrows indicate a force: the force down maintains tension on the cord while the force up translates the bead some Δz after each S_{12} measurement.

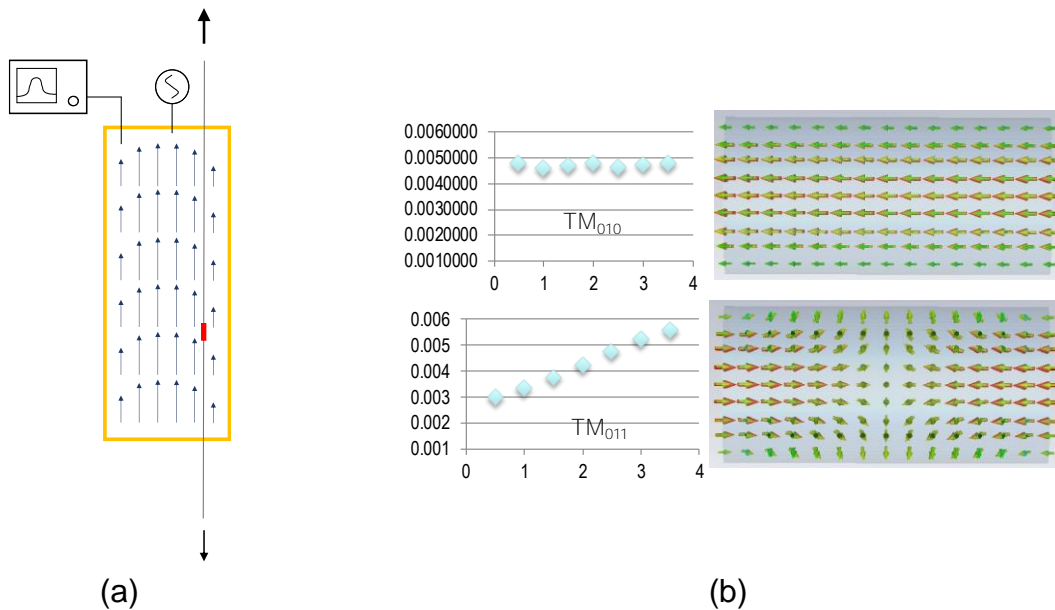


Figure 3-26. (a) Schematic of bead-pull test and (b) test results from a bead-pull test [68]. The red bar depicts the bead and the blue arrows are the E field for the TM_{010} mode (not to scale). The grey cord is pulled taut and translated a finite distance after each S_{12} measurement. The test results show Δf for several locations inside an empty cylindrical cavity next to the predicted field lines for the cavity mode that matches the results. The x -axis is the displacement of the bead from an arbitrary baseline. The node for the TM_{011} is to the left of the plot.

The test results show Δf of about half the cavity for the (top) TM_{010} and (bottom) TM_{011} modes. The frequency shift for the TM_{010} mode is approximately constant; the shift for the TM_{110} mode decreases from the edge to the center revealing one node at

the center ($\rho = 1$). The predicted field for the modes from a computer simulation is shown to the right of the data. The z-axis of the cavities is horizontal in (b).

All preexisting mode identification techniques beyond the mode map require perturbing the field in some manner. While it may be feasible to perturb the field when conducting an axion search, recent development testing revealed the need for an in-situ method of enhancing mode identification. Chapter 5 details a new approach that uses the phase of the fields to distinguish modes

3.4 High-Frequency Cavities

ADMX has successfully excluded KSVZ axions up to $\sim 3.7 \mu\text{eV}$ ($\sim 0.9 \text{ GHz}$). The experiment is currently searching for axions at DFSZ sensitivity up to about the same mass limit. Extending the search up to 1 GHz while maintaining similar sensitivity is viable, but searching at frequencies beyond 1 GHz requires new cavity technologies. For axion searches, the term “high-frequency cavity” refers to a haloscope cavity that is capable of successfully searching for axions to at least the KSVZ sensitivity above 1 GHz within a feasible time frame.

Since the limits set on the WIMP [58] and on the existence of supersymmetry [59] in recent years, interest in axion searches has increased significantly. In particular, several scientific organizations from around the world have joined the effort to expand current haloscope detector capabilities above 1 GHz. The Axion Dark Matter eXperiment High-Frequency (ADMX-HF), a National Science Foundation funded axion search now named HAYSTAC, began in 2011 as a path-finder experiment for high-frequency haloscope cavities. The Republic of Korea formed CAPP, an Institute of Basic Science, around 2014 to search for axions at frequencies above 1 GHz. ADMX formed the Cavity Working Group in 2015 to formalize the collaboration’s research and

development program for high-frequency cavities, while incorporating additional research facilities into the organization, to include Fermilab and Pacific Northwest National Laboratories. Other research institutes have also joined the efforts, such as the University of Western Australia.

The original research on high-frequency cavities was conducted by Hagmann et al. [15] in 1990. The work evaluated reducing the cavity radius, conducting searches with higher-order TM modes, both with and without dielectric materials, and using higher number of conducting tuning rods. While the groundwork for the research was established nearly 30 years ago, only in the past ~5 years has any significant work been conducted to advance the current science. A few additional concepts have been conceived since the original study, such as utilizing multiple frequency-locked cavities of smaller radius, but limited development was conducted until recently.

The simplest method to increase the frequency of a microwave cavity is to increase the size of a conducting tuning rod. HAYSTAC [24] utilized one tuning rod with a large diameter instead of two smaller-diameter rods, like ADMX, to drive up the TM_{010} frequencies. However, the form factor of the cavity is reduced as the tuning rod diameter is increased. Figure 3-2(a) shows that a larger tuning rod results in less volume with E_z field, as no field exists in the rod, which reduces C for all search modes.

Figure 3-27 shows the TM_{010} frequency range times the cavity radius, and the associated form factor of a cavity with one conducting tuning rod of varying diameter. The data was obtained from a 2-dimensional COMSOL simulation [96]. The tuning rod diameter is normalized by the cavity radius. The frequency is multiplied by the cavity radius for scaling. The scan range of a cavity would be between the minimum and

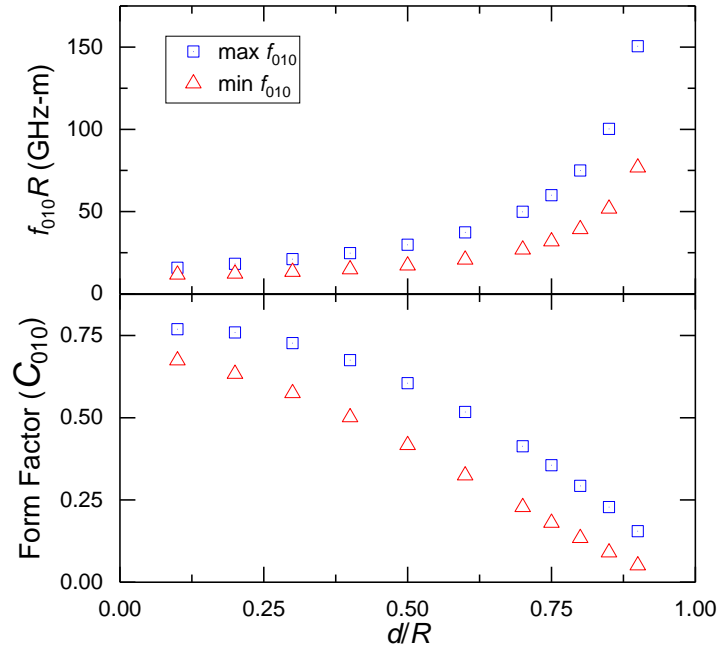


Figure 3-27. Plot of (top) frequency range and (bottom) form factor for a circular cylindrical cavity with a conducting tuning rod at varying diameters. Rod diameter (d) divided by the cavity radius (R) is shown on the x-axis. The frequency is multiplied by the cavity radius. The frequency plot shows the maximum and minimum frequencies for the TM_{010} mode. The form factor plot shows C_{010} for the associated maximum/minimum frequency. As the tuning rod diameter increases, the f_{010} increases while C_{010} decreases.

maximum f_{010} , vertically, for a given rod diameter. To tune, the rod is moved from on-center until displaced such that the rod touches the wall. As the frequencies increase with the rod diameter, the scan range increases and the C_{010} drops. The form factors shown are not the lowest form factors, as the minimum form factor occurs between the minimum and maximum frequency configurations (not shown).

A modestly more complex method to increase the search frequency is to reduce the radius of a cavity. Perturbed forms TM_{mn0} modes scales as $\sim 1/R$. To maintain the same frequency range proportionality, the tuning rods would need to be scaled the same as the radius (i.e., d/R is constant).

The length of the cavity dictates the TE modes, with a longer cavity lowering each TE mode frequency. The length of the cavity should be minimized in general to reduce mode crossings, thus driving the TE modes above the search mode. However, reducing the length of course reduces the volume of the cavity and therefore the sensitivity of the haloscope. In simple cavities with one or two tuning rods, length of $\sim 5R$ is usually considered the “best” ratio to minimize mode crossings while maximizing volume. For this reason, the aspect ratio of $L/R \approx 5$ has been historically maintained for haloscope cavities. At higher frequencies and with more complex cavities, more consideration needs to be given to mode crossings than previously.

Maintaining all other haloscope parameters and assuming anomalous skin effects (ASE), reducing the cavity geometry yields a scan rate scaling of $\sim f_{010}^{-14/3}$ [16]. Thus, cutting a cavity radius in half, along with the length and tuning geometry, will double the minimum and maximum frequencies of the search range, but will take 25 times longer to obtain the same axion sensitivity. The primary reason for the sensitivity loss is the reduction in volume; the scan rate scales as V^2 (see Eq. 2-15), and the volume scales as R^3 if the aspect ratio is not changed.

One way to regain some of the sensitivity of the haloscope is to use a stronger magnet and/or operate at colder temperatures. The scan rate scales as B_0^4 and $1/T_n^2$. Since the cavity is physically smaller, the bore of the magnet can be smaller. Solenoidal magnets with smaller bores can be made at higher strengths. To recoup the sensitivity reduction from reducing R , the magnetic strength would need scale as $R^{-7/6}$.

Similarly, smaller cavities have less mass, and thus can be cooled to a lower temperature more easily. To recover the sensitivity loss from reducing R , T_n would need

to scale as $R^{7/3}$. But the receiver chain is, at best case, quantum limited. The quantum limited noise goes as $\sim 1/R$, so recovering the sensitivity loss from reducing the cavity size could never be fully recovered by reducing the temperature alone.

All axion searches are, in some way, investigating using smaller cavities while increasing the magnet strength and reducing the operating temperature of the detector. HAYSTAC recently published results [67] utilizing this technique to scan for axions at $\sim 24 \mu\text{eV}$ ($\sim 5.8 \text{ GHz}$). However, the experiment was only able to obtain a sensitivity of $2.3 g_{a\gamma\gamma}^{\text{KSVZ}}$ (i.e., less than half the sensitivity needed to detect KSVZ axions) despite scanning at a rate ~ 10 times slower than ADMX. Note, the scan rate scales as $g_{a\gamma\gamma}^4$; HAYSTAC would need to scan 28 times longer to obtain KSVZ sensitivity, or about 300 times slower than ADMX (an ADMX cavity search is $\sim 1/2$ a year). The results demonstrate the need for further research and development of microwave cavity technology to search for axions at frequencies above 1 GHz.

Another way to improve on the sensitivity of a reduce-sized cavity is to combine the power from several cavities. Each cavity could be run as independent searches and the power spectra from each search would be added analytically. Assuming the power of each cavity is roughly the same at a given frequency, the combined power would be [106]

$$P \approx \frac{\sum P_i}{\sqrt{N}}, \quad (3-35)$$

where N is the number of cavities and the summation is over all cavities.

A haloscope detector has a finite volume for which to fit the cavities, dictated predominately by the bore size of the magnet. N will instantaneously increase as R is decreased to a size where one or more cavities can just fit within the volume, so $N(R)$ is

a step function. Volume between the cavities is unused. If the aspect ratio is maintained, volume in the longitudinal direction would also be unused except for specific cases. The effective volume, $V_{eff} = N^{1/2}V$, of all the cavities therefore discontinuous, decreasing as R^3 for a constant N , until a discrete increase in N causes an instantaneous increase in effective volume (see Fig. 3-31).

Figure 3-28 shows a schematic of a 6-cavity packing (a) top view and (b) side view inside the available volume, depicting the loss in volume (white area) between and below the cavities. The cavities in (b) are pushed to the top to emphasize the unused volume. The aspect ratio of the cavities and the available volume is $L/R = 5$. Studies using different packing ratios have been conducted [106].

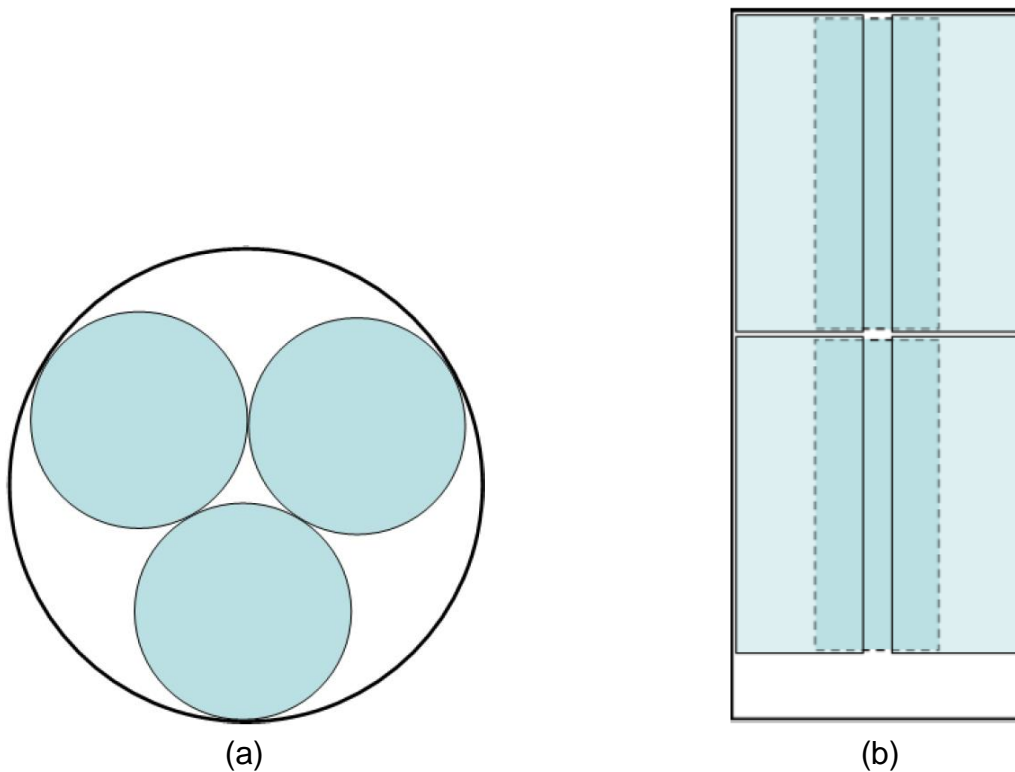


Figure 3-28. Schematic of a 6-cavity packing [78]. (a) Cross-section through the x - y plane. (b) Cross-section through the x - z plane. The inside of the cavity is in blue. The white area within the available volume (outer black lines) is unused volume. (a) and (b) are not at the same scale.

To utilize the available volume fully, partitioned cavities have been proposed. Partitioned cavities divide a large cavity that fills the available volume with solid dividers. Each cell would constitute a separate cavity. This technique increases the effective volume of the cavities, but maintain an aspect ratio of ~ 5 is considerably more challenging, resulting in more mode crossings typically. Figure 3-29 shows a photograph of the inside of a 2-cell partitioned cavity prototype. Limited testing has been conducted to advance the technology [106].



Figure 3-29. Photograph of the inside of a 2-cell partitioned cavity [68]. The cavity wall is copper plated stainless-steel and the divider is copper plate. All surfaces are electropolished. The electrical conduction between the divider and the walls is maintained with silver paint.

Figure 3-30 shows an image of the E_z field of the TM_{010} modes through a cross-section of an 8-cell partitioned cavity with one tuning rod in each cell. The white circle in each cell is the tuning rod. The black lines indicate the cavity walls and the partitions. Red indicates higher field and blue indicates lower field with zero field at the conducting boundaries. The green dots are \mathbf{E} vector arrow coming out of the page. The cells are at the same frequency.

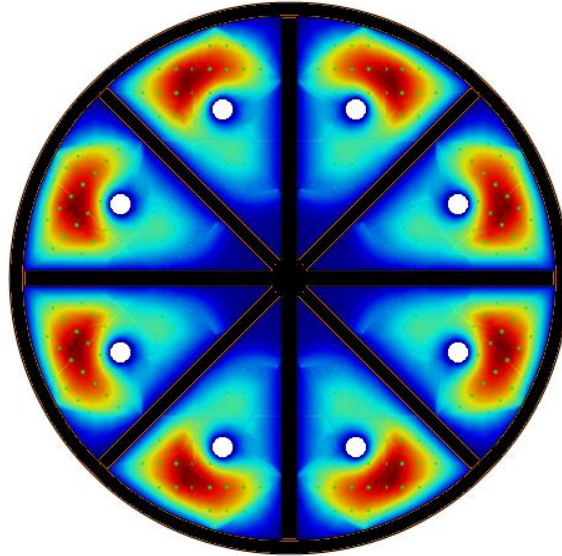


Figure 3-30. Cross-sectional images of the E_z field of the TM_{110} modes in a 8-cell partitioned cylindrical cavity. The cross-section is parallel to the cavity axis. Each cell has a single conducting rod. The white areas are the conducting rods; field inside the conductor is zero. The black lines show the outer cavity boundary and the cell dividers. Red indicates higher field and blue indicates lower field with zero field at the conducting boundaries. The green dots are the \mathbf{E} vectors out of the page.

Frequency gains of ~ 2.5 can be achieved with an 8-cell partitioned cavity, but the TM_{010} mode experiences many mode crossings unless the length of the cavity is $\sim 2R$. Several cavities must be stacked to maximize volume, reducing the sensitivity gain, as V_{eff} scales as $N^{3/2}$, and increasing complexity. Additionally, the proportional tuning range is considerably less that of the ADMX detector. Above ~ 8 partitions, each cell becomes very narrow and the tuning range becomes limited, minimizing the effectiveness of the concept.

Equation 3-35 assumes the power is combined from the different cavities or cells incoherently. At high numbers of cavities, the sensitivity gain from using multiple cavities tappers off. Alternatively, if the power is combined coherently, the total power is approximately the sum of all the power from all the cavities, $\sum P_i$, assuming the individual

powers are approximately the same. The effective volume is the sum of the volume of all the cavities, $V_{eff} = NV$.

Figure 3-31 shows a plot of the effective volume of multiple cavities versus TM_{010} frequency when the power is combined coherently and incoherently. The effective volume is normalized by the available volume (V_{max}) and the frequency is normalized by the TM_{010} frequency of an equivalent cavity that fills the available volume ($f_{V_{max}}$). The spikes in the plot represent discontinuities where N incrementally increases at a given R . The plot shows coherent power combining produces a higher gain in sensitivity, especially at higher frequencies (i.e., higher M). Because scan rate is proportional to V_{eff}^2 , incoherently combined cavities would need to scan N times as long as the same coherently combined cavities to obtain the same sensitivity.

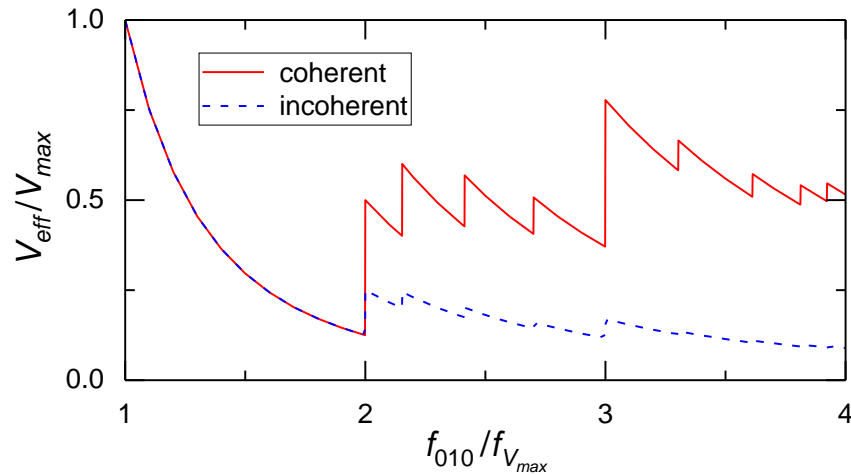


Figure 3-31. Plot of effective volume versus TM_{010} frequency for power combined cavities. Results are shown for power combined coherently (red solid line) and incoherently (blue dashed line). The volume is normalized by the available volume. The frequency is normalized by the TM_{010} frequency of a single cavity that fills the available volume. Combining power coherently is much more effective at increasing the detector sensitivity.

Coherent power-combining is accomplished by frequency-locking the cavities (cells) together and combining the analog signal measurements in phase. Frequency

locking is accomplished with a feed-back system that controls the tuning rod(s) and/or an auxiliary tuning device to match the search mode frequency of all the cavities. The power produced from axion conversion within haloscope cavities within close proximity will always be in phase, because the de Broglie wavelength of the axion is tens of meters or greater.

The combined power from two cavities close in mode frequency, neglecting losses through the combiner, is [107]

$$P \approx \frac{1}{2} \left[\frac{\bar{f}^2}{Q^2} + \frac{\delta f^4 Q^2}{\bar{f}^2} \right]^{-1} \left[P_1 \left(\frac{\bar{f}^2}{Q^2} - \delta f^2 \right) + P_2 \left(\frac{\bar{f}^2}{Q^2} - \delta f^2 \right) + 2 \sqrt{P_1 P_2} \left(\frac{\bar{f}^4}{Q^4} - \delta f^4 \right) \right], \quad (3-36)$$

where δf is the difference between the mode frequencies and \bar{f} is the average frequency of the two modes. P_i is the power extracted from the two cavities. The quality factor is assumed to be approximate the same for both cavities. When $\delta f < \bar{f}/Q$, Eq. 3-36 simplifies to

$$P \approx \frac{1}{2} (1 - \beta^4) \left[P_1 (1 - \beta^2) + P_2 (1 - \beta^2) + 2 \sqrt{P_1 P_2} \left(1 - \frac{\beta^4}{2} \right) \right], \quad (3-37)$$

where

$$\beta = Q \frac{\delta f}{\bar{f}}. \quad (3-38)$$

If a frequency-matching criterion is set at $\delta f < \bar{f}/10Q_L$, Eq. 3-37 is expanded for N cavities as

$$P \approx \frac{(\sum \sqrt{P_i})^2}{N}, \quad (3-39)$$

where the sum is over N .

Power is lost from phase shifting of the signal between the cavities and the combiner if the cable lengths from the cavities/cells to the combiner are not the same. Power is lost from the combiner's impedance as well, and should be minimized. ADMX

is currently developing frequency-locked cavities and in-phase power combining receivers for high-frequency axion searches.

A separate method of searching for axions at higher frequencies is to scan higher-order modes. Though the TM_{010} has the highest form factor by a considerable amount, with a large volume cavity, a strong magnetic field, and a very low temperature, KSVZ sensitivity could be achieved with higher-order TM modes within a viable time frame. ADMX has recently instrumented their detector with a receiver channel dedicated to scanning higher-order modes. No results have been released to date.

The next higher search mode above the TM_{010} mode yields a form factor of $\sim 0.05-0.25$ depending on the tuning rod(s) configuration. The mode is often referred to as the TM_{020} mode, though the desired search mode is quite commonly another mode (see Fig. 3-11). Figure 3-32 shows a scatter plot of form factor versus frequency for the three lowest TM_{mn0} modes of ADMX.

The results are from a 2-dimensional eigenfrequency solver [96]. The values shown are for various rod configurations (not specified), but are not all inclusive. The frequency on the x-axis is multiplied by the cavity radius (0.21 m) for scalability. The TM_{010} and both broken degeneracies of the TM_{110} modes are shown. The TM_{110} mode(s) is the next higher search mode above the TM_{010} for the ADMX haloscope, though the experiment calls the mode $TM_{020(A)}$ [100]. The true TM_{020} mode is the third highest search mode for ADMX, having a frequency of $fR \approx 0.275$ ($f_{020} \approx 1.3$ GHz for ADMX) and a form factor of $\sim 0.05-0.10$ [108].

At first glance, scanning higher-order TM modes with adequate form factors might appear to be the simplest method to search for high-frequency axions. To scan

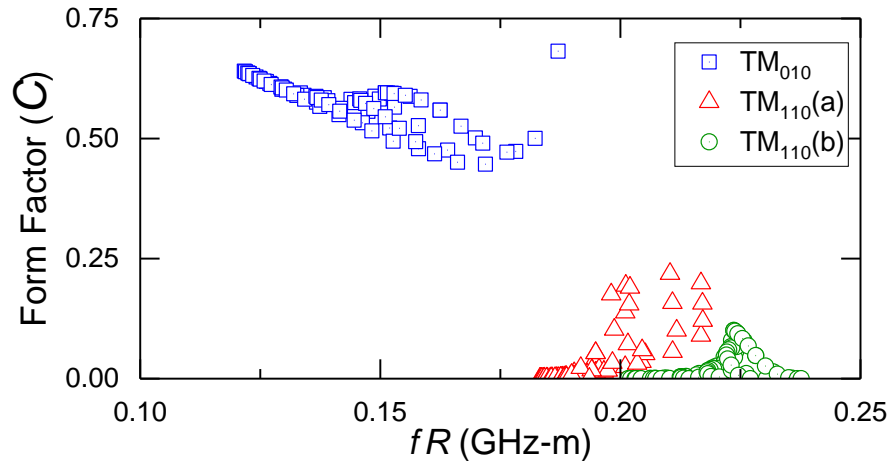


Figure 3-32. Plot of form factor versus frequency for the three lowest search modes of ADMX. The frequency on the x-axis is multiplied by the cavity radius for scaling; for ADMX, $R = 0.21$ m. The TM_{010} and broken degeneracies of the TM_{110} modes are shown. Due to transverse symmetry breaking, the TM_{110} mode is a viable search mode, and has a higher form factor than the TM_{020} mode, which is higher in frequency (not shown). ADMX refers to the mode as $TM_{020(A)}$ [100].

higher-order modes, the only hardware change is the receiver chain electronics to account for the higher frequency signal. But the same changes would be required of a higher frequency search regardless of method. No new cavity technology would seemingly be required. However, as demonstrated by Fig. 3-25, mode density around higher-order mode is very high. Mode identification and tracking becomes extremely challenging.

Characterizing the search mode prior to a search and having an in-situ technique of verifying the mode is a necessity. Mode identification techniques to support searching higher-order modes are being developed (see Chapter 3.3 and Chapter 5.0). HAYSTAC is investigation using a dielectric cylindrical ring to spoil parts of higher-order modes to improve the form factor, but the technique will not mitigate the mode identification problem.

The most effective method of elevating the search modes of a cavity for axion detection is to use additional conducting tuning rods [15]. As Fig. 3-6 alludes to, increasing the number of rods will increase the curvature of the field in the TM_{010} modes, driving up the frequency. Higher-order modes will also increase, though field localization will result in a lesser increase than TM_{010} , proportionally. The complex solutions of higher-order modes require analytical computation to evaluate the frequencies and form factors. Further, additional tuning rods increase mode density. TE mode frequencies are not significantly altered, driving search modes into highly crowded frequency ranges.

In collaboration with HAYSTAC, a cavity study was conducted to evaluate using higher number of tuning rods to elevate the TM_{010} frequency of the cavity [16]. The study initially evaluated linear translation and off-axis rotation of the rods. However, linear translation was deemed too difficult to implement and the initial results were not notably better than the initial results of the off-axis rotation concept. So, the study focused primarily on off-axis rotating rods. In addition to circular cross-section rods, the study included wedge-shaped rods, or vanes.

The study was conducted using a 2-dimensional FEM and an eigenfrequency solver in COMSOL version 4.2 [96]. The study analyzed 99 tuning configurations, consisting of 4, 6, 7, and 8 tuning rods, and 4 and 6 tuning vanes. For each configuration, a finite number of rods/vanes were stationary and a finite number rotated about the center axis. The configurations are commonly referred to as periodic arrays of tuning rods or vanes. The TM_{010} tuning range for the various configurations were computed as well as C_{010} and Q throughout the range.

Figure 3-33 shows the geometry of example (a) 6-rod and (b) 4-vane cavities. The diameter of the rods is d , and circle radii ρ_S and ρ_R are the location of rotating and stationary rods, respectively, measured from the center of the cavity. The vanes have an angle of θ and rounded ends. The circle radii ρ_I and ρ_O are the location of center of the inner and outer vane end-rounds, respectively, measured from the center of the cavity. The outer circle are the cavity walls. The solid hatched rods/vanes depict the maximum TM_{010} frequency configuration. The arrows show the direction of the rotating rods/vanes, and the dashed hatched rods/vanes depict configuration of the rotating rods/vanes in the minimum TM_{010} frequency configuration.

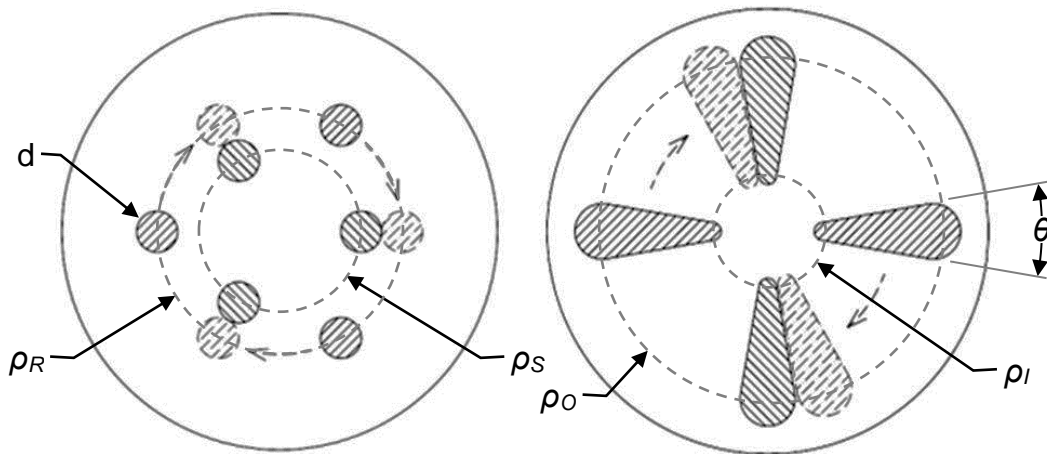


Figure 3-33. Geometry of example cavities from periodic array study. (a) 6-rod. (b) 4-vane. Three rods move in (a) and two vanes move in (b). The solid hatched lines show the maximum frequency configuration for the TM_{010} mode. The dotted hashed lines show the rotating rods/vanes in the minimum frequency configuration. The arrows show the direction of the moving rods/vanes.

Figure 3-34 shows images of the E_z field of the TM_{010} mode through a cross-section of a (top) 6-rod and (bottom) 4-vane cavities. The (left) minimum frequency and (right) maximum frequency configurations are shown. The white area is the location of

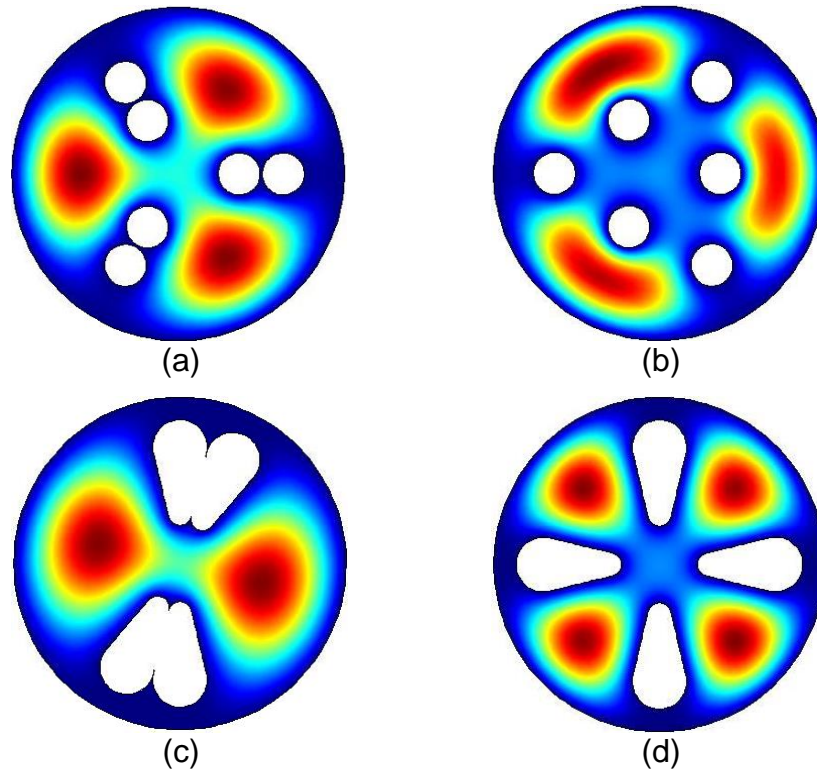


Figure 3-34. Cross-sectional images of the E_z field for the TM_{010} mode in periodic arrays. (a) 6-rod minimum frequency configuration. (b) 6-rod maximum frequency configuration. (c) 4-vane minimum frequency configuration. (d) 4-vane maximum frequency configuration. The cross-section is parallel to the cavity axis. The white areas are the location of the conducting rods/vanes; a field solution is not included in the images as there is zero field inside the conductor. The outer edge of the images and white areas are the conducting boundaries. Red indicates higher field and blue indicates lower field with zero field at the boundaries.

the rods/vanes with no field solution. Red indicates higher field and blue indicates lower field, with zero field at the boundaries.

The study revealed that periodic arrays are extremely sensitive to transverse localizations. Small changes in the configuration can drive the predominance of the field to a very small area(s) of the cavity cross-section, causing C_{010} to be reduced greatly. The study highlighted the importance of discrete transverse symmetry in haloscope cavities, and demonstrated the need for A well distributed E_z field, like those shown in

Fig. 3-34. As a result, many of the 99 configurations analyzed proved to be unusable, as large sections of their tuning range had too low of a form factor.

The study identified 13 configurations that yields the highest scan rates. Table 3-1 shows the tuning rod/vane configurations of the 13 cavities, normalized by the cavity radius for scaling. The number of tuning rods/vanes is N , and the subscripts R and S indicates rotating and stationary rods/vanes.

Table 3-1. Configuration of cavities with the highest scan rates from the periodic array study.

Rods						
Design	N	N_R	N_S	ρ_R/R	ρ_S/R	d/R
A	4	2	2	0.413	0.413	0.350
B	4	2	2	0.425	0.425	0.300
C	4	2	2	0.454	0.454	0.350
D	6	3	3	0.375	0.625	0.250
E	6	3	3	0.375	0.750	0.375
F	6	3	3	0.400	0.675	0.275
G	6	3	3	0.400	0.800	0.300
H	7	3	4	0.450	0.450	0.200
J	7	3	4	0.525	0.525	0.175
K	8	4	4	0.550	0.550	0.200
Vaness						
Design	N	N_R	N_S	ρ_l/R	ρ_o/R	θ (°)
L	4	2	2	0.250	0.800	27.0
M	4	2	2	0.300	0.700	27.0
N	6	3	3	0.300	0.600	9.0

The results of the study showed that periodic array cavities could be used to conduct high-frequency axion searches. The configurations shown in Table 3-1 obtained a frequency range of $0.2 \text{ GHz-m} \gtrsim f_{010}R \gtrsim 0.3 \text{ GHz-m}$ ($\sim 1.0\text{-}1.5 \text{ GHz}$ for an ADMX-size cavity) and form factors of $0.3 \gtrsim C_{010} \gtrsim 0.7$. Scan rates approximately equivalent to that of four coherently power-combined cavities that fit in the same allowable space were also achieved, demonstrating the method detection potential.

Higher frequencies could be attained with more conducting rods/vanes, but at a cost of greater sensitivity to localization. See Stern et al. [16] for detailed results of the study.

The study did not evaluate the effects of longitudinal symmetry breaking or mode crossings. At the time of the study, the significant effects of longitudinal localization were not fully realized; only after prototype development was the extreme sensitivity of periodic array discovered (see Chapter 4.0). Mode crossing was expected to be an unavoidable problem. The increase of mode crossings due to mode crowding from longitudinal symmetry breaking was also not realized until prototype testing.

As a result of the study, 6-rod and 12-vane prototype cavities were developed by HAYSTAC and ADMX, respectively. The 6-rod prototype testing was unsuccessful, causing the experiment to utilize the single tuning rod cavity described above. The 12-vane prototype was tested in cryogenic temperatures to advance the scientific understanding of longitudinal symmetry breaking and identify technology needs for expanding the capabilities haloscope detectors (see Chapter 4.0).

A 19-rod periodic array was also evaluated. Higher frequency ranges were obtained as expected, but localization of the field caused the form factor to drop to an unusable value during the frequency tuning. Figure 3-35 shows images of the E_z field of the TM_{010} mode through a cross-section of a 19-rod cavity concept. The (a) minimum frequency and (b) maximum frequency configurations are shown. The minimum frequency configuration demonstrates how transverse localization can greatly hinder the form factor, where $C_{010} = 0.26$. The lowest form factor observed throughout the tuning range was < 0.1 (not shown).

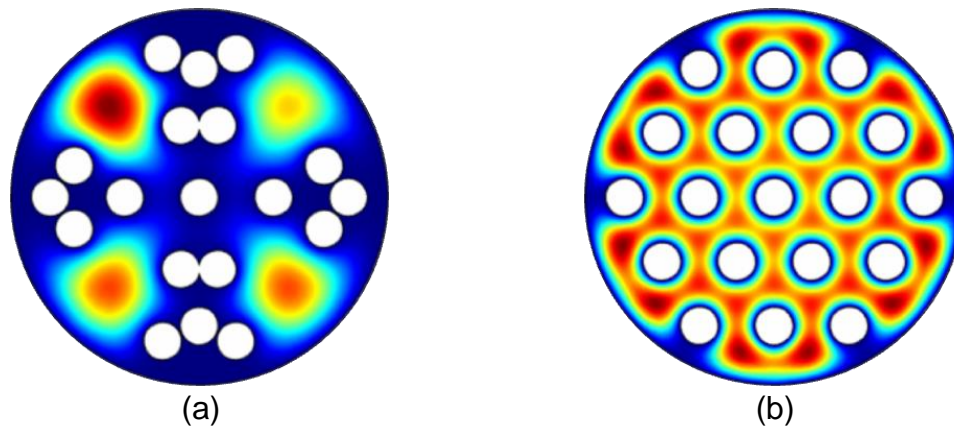


Figure 3-35. Cross-sectional images of the E_z field for the TM_{010} mode in a 19-rod periodic array cavity. (a) Minimum frequency configuration. (b) Maximum frequency configuration. The cross-section is parallel to the cavity axis. The white circles are the conducting rods; a field solution is not included as there is zero field inside the conductor. The outer edge of the images and white areas are the conducting boundaries. Red indicates higher field and blue indicates lower field with zero field at the boundaries. A form factor of $C_{010} < 0.1$ was computed during a significant part of the tuning range.

ADMX is researching dielectric coatings for tuning. A variable dielectric layer would be fixed to the cavity wall's conducting boundary. Applying an electric potential across the dielectric changes the dielectric constant, which alters the fields and frequency of search modes. Because the coating runs the entire length of the cavity, longitudinal symmetry is maintained. No mode repulsion would be observed at mode crossings, eliminating holes in the frequency search spectrum. However, in order to obtain an even change in property across the entire coating, only a modest dielectric layer can be used. Thus, very small tuning can be obtained with the concept under the best circumstances, and the method could likely only be used for fine tuning of a cavity.

Superconducting thin-film hybrid cavities are being developed by HAYSTAC and ADMX. The cavity surfaces normal to the magnetic field would utilize superconducting films while the surfaces perpendicular to the field would maintain copper or aluminum

boundaries. If superconductivity of the longitudinal surfaces is maintained, a gain of ~ 10 can be achieved in Q .

3.5 Superconducting Hybrid Cavities

One potential technique of recapturing some of the loss in sensitivity from utilizing small-volume cavities is to significantly increase the quality factor of the cavity. The scan rate is proportion to Q_L (see Eq. 2-15) up to $Q_L = Q_a$, believed to be $\sim 10^6$ or greater. Holding the aspect ratio constant, increasing Q_L as R^{-6}/N will maintain the same detection sensitivity. Superconducting hybrid cavities may enable such a gain.

Superconductivity, first discovered in 1911 [109], demonstrated that select metals below a critical temperature T_c allow current to flow with zero resistance.

Superconductivity originates from the pair correlation of electrons through electron-phonon interaction, a mechanism of the Bardeen-Cooper-Schrieffer (BCS) theory [110], with each “Cooper” pair having opposite momentum and spin. Two types of superconductors exist. Type I superconductors expel magnetic flux up to a critical field, $H_c \ll 1$ T, and above H_c the superconductivity is destroyed. Type II superconductors typically have a much higher H_c and allow partial flux penetrations below H_c . Each flux penetration results in a local current vortex, which incrementally increases the overall lossiness of the material [111].

Microwave cavities with superconducting boundaries, such as those used in particle accelerators, are well developed and have demonstrated $Q > 10^{10}$. However, such cavities use type I superconductors which are not suitable for use in a strong magnetic field. Placing a type I cavity in a haloscope detector would fully destroy the superconductivity, resulting in the energy dissipating through the base material which is

more lossy than copper or aluminum. Even a cavity using a type II superconductor would experience many vortexes, which would result in the material being more lossy.

Recent experiments, which directly confirmed the pair-breaking theory of Abrikosov and Gor'kov for the optical conductivity of superconducting thin-films [112], have led to the prospect of using type II superconducting thin-film coatings on haloscope cavities [113]. The cylinder walls and tuning rods/vanes surfaces are coated with the film, while the end-caps remain uncoated conductors. In order to avoid flux penetration, the thickness of the coating needs to be less than the lattice constant of the flux lattice,

$$a = \sqrt{\frac{8\pi\Phi_0}{3B}}, \quad (3-40)$$

where Φ_0 is the magnetic flux quantum. This configuration is often referred to as a hybrid cavity.

The ideal hybrid cavity in a haloscope would maintain perfectly superconducting vertical surfaces while operating in a magnetic field with no radial field strength, resulting in no magnetic flux penetrating the superconducting surfaces. From Eq. 3-26, the unloaded quality factor of the hybrid cavity is

$$Q_H = L \left[\bar{\delta}_{ends} + \bar{\delta}_{SC} \sum \xi_i^{(r)} \frac{L}{R} \right]^{-1}, \quad (3-41)$$

where $\bar{\delta}_{SC}$ is the skin depth in the superconducting surfaces and the summation is over all superconducting surfaces. Equation 3-41 can be recast in the form $Q_H = [1/Q_{end} + 1/Q_{SC}]^{-1}$, where

$$Q_{ends} = \frac{L}{\bar{\delta}_{ends}} \quad (3-42)$$

$$Q_{SC} = \frac{R}{\bar{\delta}_{SC}} \left[\sum \xi_i^{(r)} \right]^{-1}. \quad (3-43)$$

When no magnetic field penetrates the superconducting surfaces, $\delta_{SC} \ll \delta_{ends}$ and $Q_H \approx Q_{ends}$. Note, Q_H is no longer dependent on the R , or the rods/vanes configuration and size. The gain in Q_H is

$$\frac{Q_H}{Q} = 1 + \frac{L}{R} \xi_{eff}, \quad (3-44)$$

where $\xi_{eff} = \sum \xi_i^{(1)}$. For an empty cavity, $\xi_{eff} = 1$; for a cavity with two tuning rods, such as ADMX, $\xi_{eff} \approx 1.5$. In general, ξ_{eff} will increase with more surface area, and thus more tuning rods/vanes, though the mode configuration also contributes significantly (see Eq. 3-27).

A superconducting hybrid cavity similar to the ADMX cavity would see a gain in Q of ~ 10 . From 2-dimensional analyses, a periodic array cavity using superconducting films could obtain gains as high as ~ 50 . The results are intuitive. Each additional tuning rod adds significant surface for which power is lost through resistive heating. Superconducting currents have no resistance, so no heating occurs and, thus, no loss in power.

The results assume longitudinal symmetry. The interaction of the capacitive effect with the superconducting films has yet to be investigated and could prove problematic. The rods/vanes must be superconducting or Q reverts to Eq. 3-41 with the absence of the walls in the summation. The gain in Q would not be significant as the influence of the rods/vanes on ξ_{eff} is considerably greater than the that of the walls. So, the capacitive effect is unavoidable.

Misalignments of the cavity relative to the magnetic field, and radial components of the magnetic field may result in flux penetrations, which will diminish Q_H . First order

approximations of the effects can be computed by relating Q_H to the optical conductivity of the surface. The classical skin depth is

$$\delta = \sqrt{\frac{2}{\mu\omega\sigma}}. \quad (3-45)$$

where σ is the conductivity at the boundary. Maxwell-Garnett theory estimates the effective conductivity of superconductors at frequencies of axion searches as

$$\sigma_{eff} = \sigma_{SC} \frac{(1 + \chi)(1 - \sigma_{SC}/\sigma_n) + 2(\sigma_{SC}/\sigma_n)}{(1 - \chi)(1 - \sigma_{SC}/\sigma_n) + 2(\sigma_{SC}/\sigma_n)}, \quad (3-46)$$

where σ_n and σ_{SC} are the classical (non-superconducting) and superconducting conductivity of the thin film, and $\chi = B_{\perp}/\alpha$ is the volume fraction of the vortices, with B_{\perp} the magnetic field strength perpendicular to the surface. Experimental data has estimated $\alpha \approx 10.9$ T for niobium-titanium nitride ($\text{Ni}_{0.5}\text{T}_{0.5}\text{N}$) [114], a promising candidate for thin-film materials of hybrids.

For an angular misalignment, φ , of the cavity relative to the field, the effective perpendicular field is estimated

$$B_{\perp} \approx \frac{1}{2}B \sin(\varphi). \quad (3-47)$$

Equations 3-45 through 3-47 are solved backwards to resolve the effective skin depth of a misaligned hybrid cavity. The skin depth is entered into Eq. 3-43 to find Q_H for the cavity. When $\delta_{SC} = \delta_{ends}$, Q_H becomes same Q . Because the classical conductivity of a type II superconducting material is lower than that of conventional cavity conductors (e.g., copper and aluminum), a sizable misalignment can cause Q_H to be lower than Q .

For fields that are inhomogeneous, Eq. 3-47 can be used to estimate the effective perpendicular field where φ is now the angle of the field relative to the cavity at the endcap interfaces. Figure 3-36 shows a schematic of a hybrid cavity (a) with an

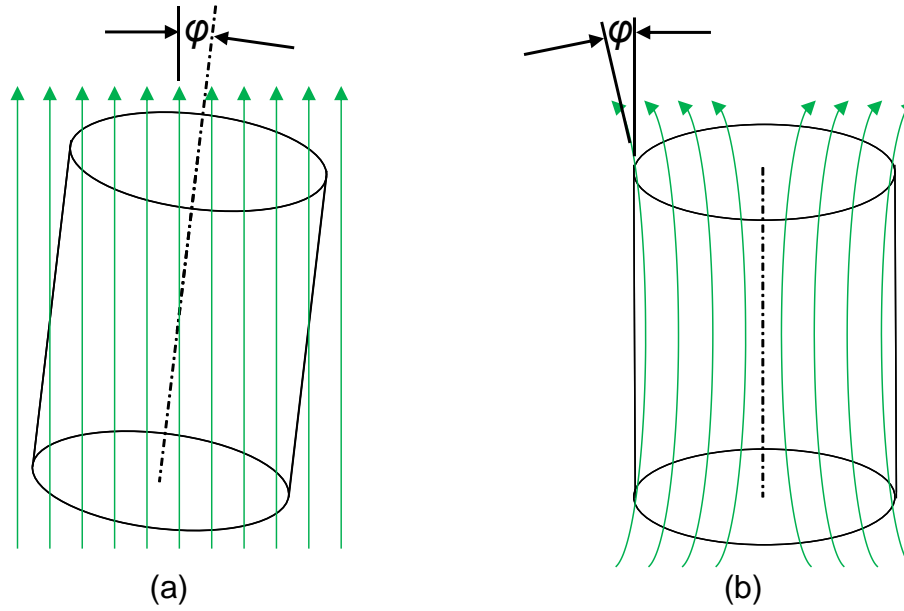


Figure 3-36. Schematic of perpendicular magnetic fields in superconducting hybrid cavities. (a) Cavity tilted relative to the field. (b) Inhomogeneous magnetic field. The magnetic field is depicted as green arrows.

angular misalignment relative to the magnetic field and (b) in an inhomogeneous magnetic field. The magnetic fields are depicted by green arrows.

CHAPTER 4 12-VANE CAVITY PROTOTYPE

4.1 Design

The results of a study of 2-dimensional periodic array cavities showed that using multiple tuning rods/vanes in microwave cavities has high potential for use in high-frequency axion searches. Based on the findings of the study, various periodic array configurations using rods and vanes were investigated to evaluate the search range and sensitivity throughout the range. Though most of the concepts yielded moderate sensitivity and/or range, a 12-vane configuration demonstrated significantly greater sensitivity across a considerable range.

The 12-vane design used 4 stationary vanes and 8 vanes that rotated about the center axis, with 4 rotating clockwise and 4 counterclockwise, symmetrically. In the minimum f_{010} frequency configuration, four sets of three vanes are grouped together, forming four cells of equal size. As the vanes move, the vanes in each set fan out, forming 12 cells. The cells are of two different sizes, with four cells of one size and eight cells of another, until the maximum f_{010} frequency configuration, where the 12 cells are equal in size.

Figure 4-1 shows a schematic of a cross-section of the 12-vane cavity in the (a) minimum f_{010} frequency configuration and (b) maximum f_{010} frequency configuration. The white area represents the vanes. The stationary vanes are on the x -axis and y -axis as oriented in the figure. The grey arrows show the direction of rotation of the moving vanes between the configurations. The inner and outer tip of the vanes have sharp edges rather than rounds for ease of fabrication.

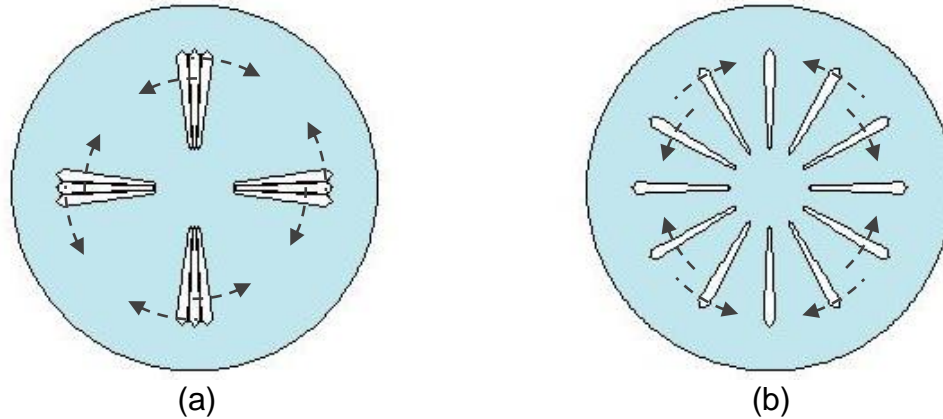


Figure 4-1. Schematic of a cross-section through the x - y plane of the 12-vane prototype. (a) Minimum f_{010} frequency configuration. (b) Maximum f_{010} frequency configuration. The resonant area of the cavity is in blue; the white areas are the vanes. The gray arrows indicate the direction of the moving vanes between configurations.

The 12-vane configuration was optimized for tuning range, while keeping a lower bound on $C > 0.3$, using a 2-dimensional FEM eigenfrequency solver in COMSOL version 4.2 [96]. At the time of the simulations, the significant effects of longitudinal symmetry breaking on periodic arrays were not realized.

The analysis yielded a cavity with a search range of $0.27 \text{ GHz}\cdot\text{m} \geq f_{010}R \geq 0.46 \text{ GHz}\cdot\text{m}$ (1.1-1.8 GHz for an ADMX-size cavity) and form factors of $0.32 \geq C_{010} \geq 0.59$. The profile-angle of the vanes was $\theta = 5^\circ$ (see Fig. 3-33) and a tip-to-tip length of the vane-profile was $0.138R$. Figure 4-2 shows C_{010} verses $f_{010}R$ as resolved from the 2-dimensional simulations. The results indicated that the 12-vane design used in the ADMX haloscope would yield similar sensitivity as the current ADMX detector with equivalent scan times, but at about double the frequency coverage. Higher modes were not extensively evaluated, but the simulations showed C_{020} in the range of 0.1-0.2.

A radius of $R = 6.826 \text{ cm}$ was selected for the prototype to fit the available cryogenic equipment; the vane geometry was scaled appropriately (see Fig. 4-11)

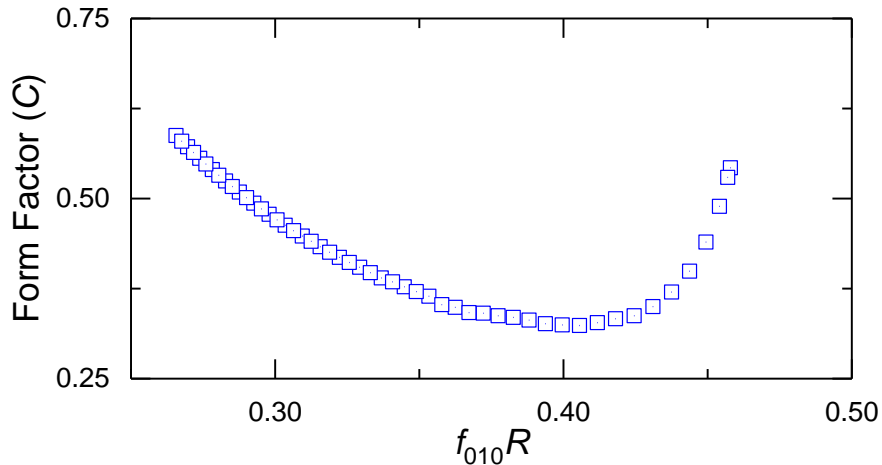


Figure 4-2. Plot of C_{010} versus f_{010} for the 12-vane cavity. The frequency is multiplied by the cavity radius for scaling. The form factor is comparable to ADMX with a frequency range that is about twice as high.

yielding a predicted TM_{010} frequency range of 3.9-6.7 GHz. An aspect ratio of $L/R = 4$ was used to reduce mass and cost of the cavity. The analytical mode predictions were initially done with a 2-dimensional simulation. Figure 4-3 shows the analytical predictions from the 2-dimensional model. The TM_{010} mode frequency is shown as red triangles. The angle of vane rotation is θ , with the minimum f_{010} position $\theta = 0^\circ$ and the maximum f_{010} position $\theta = 25^\circ$.

The analysis predicted only 14 modes crossings, which is higher than ADMX, but not so great as to expect the configuration to be unworkable. However, the 2-dimensional model does not evaluate modes with subscripts $p > 0$, as those modes require 3-dimensional boundary conditions. So, a greater number of mode crossing was anticipated.

Successful testing of the prototype was dependent on verifying an evenly dispersed E_z field throughout the cavity to ensure a high form factor; localization in one or two cells would significantly degrade C_{010} . The cavity was fitted with eight antenna probes, six on the bottom-plate and two on the top-plate. The antennas on the bottom-

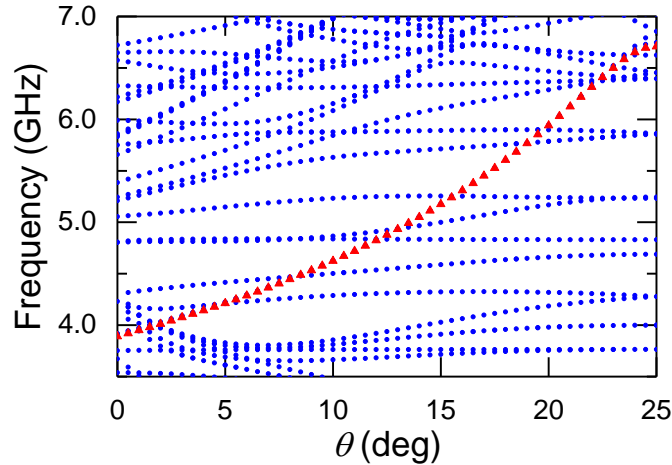


Figure 4-3. Frequency predictions for the 12-vane prototype from a 2-dimensional analysis. The blue circles show all predicted mode frequencies while the red triangles show the predicted f_{010} . The vane rotation is shown on the x-axis from the minimum f_{010} position ($\theta = 0^\circ$) to the maximum f_{010} position ($\theta = 25^\circ$). The simulation predicted 14 mode crossings.

plate are positioned to measure the field in 4 cells; the antennas on the top-plate are in line with two of the antenna on the bottom-plate to compare the field at opposite ends of the cavity.

Figure 4-4 shows images of the E_z field through a cross-section of the 12-vane cavity for the TM_{010} in the (a) minimum and (b) maximum frequency configurations. The locations of the bottom antennas are overlaid as small black circles, labeled A-F. The top antennas are in the same location as antennas B and E, and are identified as antennas G and H, respectively.

To enable mechanical motion of the rotating vanes, each set of four rotating vanes were physically connected with a cross bracket at the top and bottom of the cavity, for a total of four cross brackets. The cross brackets have a hole in the middle to accommodate a drive shaft or an idler shaft (for stability). A coaxial drive shaft is inserted through the top-plate and connects to the holes in each of the top cross brackets to drive the sets of 4 vanes in opposite directions. A mechanical gap of

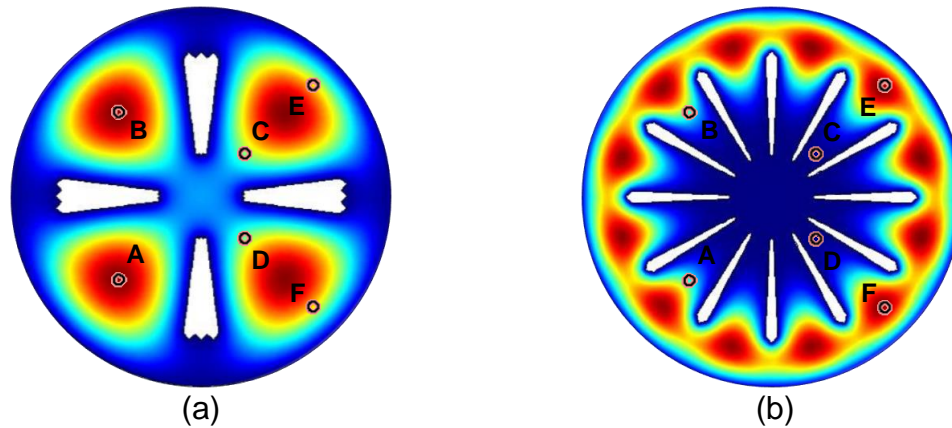


Figure 4-4. Cross-sectional images of the E_z field for the TM_{010} mode of the 12-vane prototype design with bottom antenna positions overlaid. (a) Minimum frequency configuration. (b) Maximum frequency configuration. The cross-section is parallel to the cavity axis. The black circles indicate the location of the bottom antennas, labeled A-F. The white wedges are the conducting vanes; a field solution is not included as there is zero field inside the conductor. The outer edge of the images and white areas are the conducting boundaries. Red indicates higher field and blue indicates lower field with zero field at the boundaries.

0.13 cm between each moving piece and endcaps was maintained to allow sufficient clearance for the parts to move. The stationary vanes were rigidly connected to both endcaps.

Figure 4-5 shows a computer-aided design (CAD) model of the cavity prototype (a) complete and (b) with the top-plate and half of the cavity wall removed. Antennas G and H are seen on the top-plate of (a). The vanes are in the maximum f_{010} frequency configuration in (b). The idler shaft is just visible in (b) at the bottom center of the cavity. Additional holes and assembly components (e.g., screws) are also visible; the holes/hardware are for assembly or interfacing to the test equipment.

During the initial testing of the complete cavity (see Chapter 4.2), significantly more modes were detected than were predicted. As a result, 3-dimensional FEM simulations using COMSOL version 4.3b [96] were employed to identify the $p > 0$

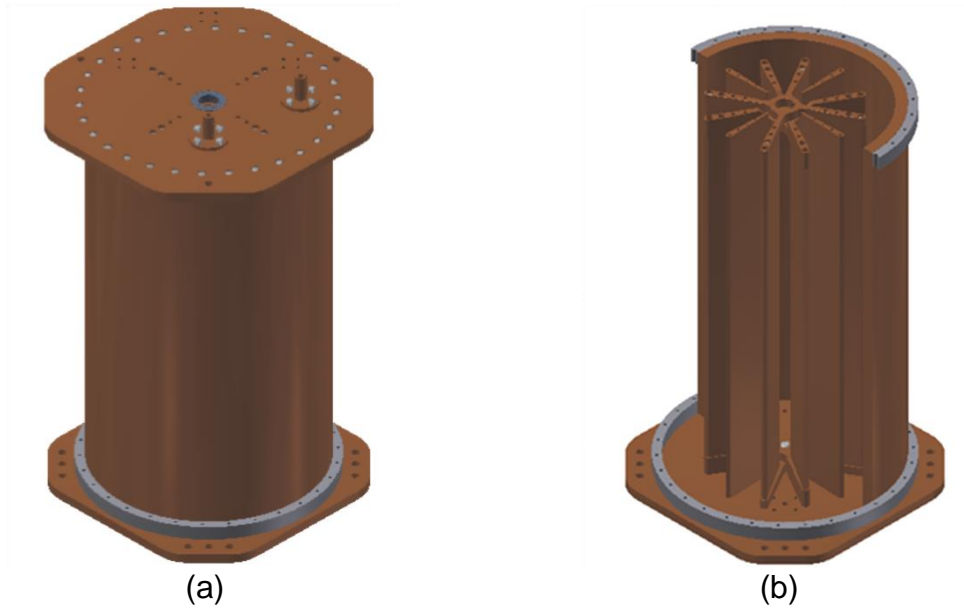


Figure 4-5. CAD models of the 12-vane prototype. (a) Complete model. (b) Model with top-plate and half of the wall removed. The maximum f_{010} frequency configuration is shown in (b).

modes. Two models were developed. The simplified model consisted of the outer boundaries and the vanes. The stationary vanes ran the entire length of the cavity while the rotating vanes maintained a mechanical 0.13 cm gap at either end. The more complex model included basic geometry of the cross brackets with the 0.13 cm gaps maintained between all moving components like the cavity design. Figure 4-6 shows the geometry of the (a) simplified and (b) complex 3-dimensional FEMs. The top-plate and half of the wall is removed.

The simplified 3-dimensional model was initially used to evaluate mode crossings and form factor discrepancies from the 2-dimensional model. The first results from the simplified model showed a significantly greater mode density than the 2-dimensional model. Upon inspecting the details, an unexpected mode solution was observed. The electric field was localized in the center of the x - y cross-section of the model at both ends. While some small localization was expected, at the time of the simulations a

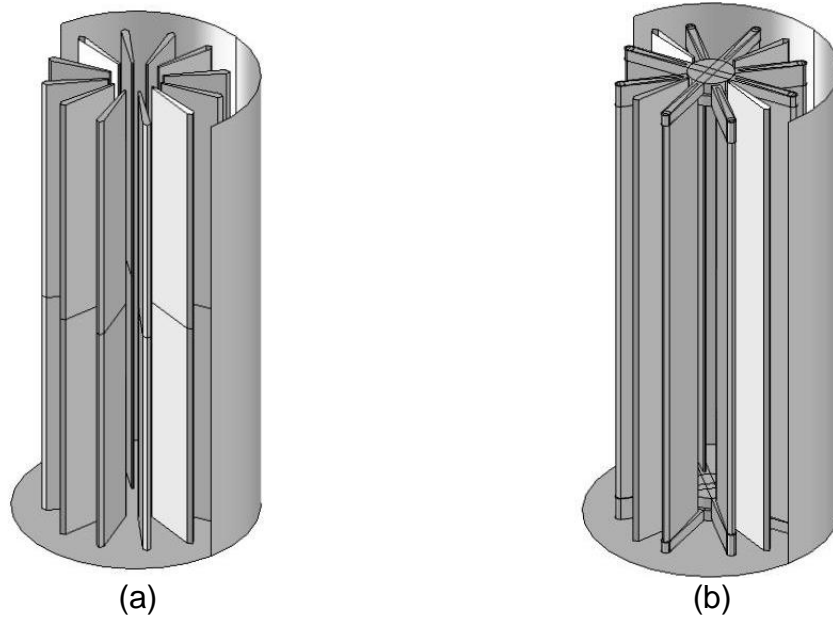


Figure 4-6. FEMs of the 12-vane prototype. (a) Simplified. (b) Complex. The top-plate and half of the wall is removed. The maximum f_{010} frequency configuration is shown.

mechanical gap of $g/L \approx 0.005$ was assumed to have a negligible effect on the mode.

The ADMX cavity has maintained a mechanical gap of $g/L = 0.007$ though all the experiment's searches.

Figure 4-7 shows images of $|\mathbf{E}|$ of the TM_{010} mode in a cross-section as resolved by the 3-dimensional FEM simulations using (a) the simplified model and (b) the simplified model with no mechanical gaps (all vanes run the full length of the cavity). The model is in the maximum f_{010} frequency configuration. The cross-section is through the z-axis and is 45° to x-z planes, symmetrically cutting between the vanes. For visualization, the cut would go through antennas A, C, and E in Fig. 4-4(b), thus avoiding all vanes.

A large localization of the field can be seen at either end of (b). The localization was greater than expected and was not exclusively within the mechanical gaps, as was demonstrated in previous studies [15]. Careful review of the image shows a small field

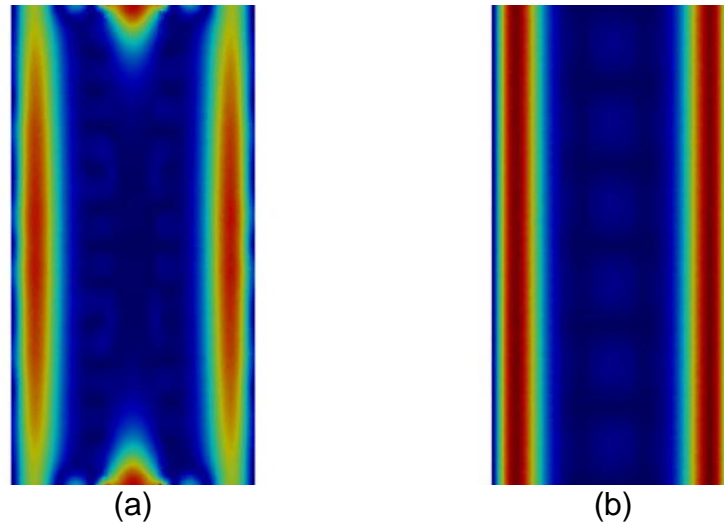


Figure 4-7. Cross-sectional images of $|\mathbf{E}|$ of the TM_{010} mode in 12-vane prototype as resolved by FEM simulation. (a) Simplified model. (b) Simplified model with mechanical gaps removed. The cross-section is through the z -axis and at a 45° angle to the x - z plane. The cross-section does not cut through any vanes. Red indicates higher field and blue indicates lower field. The first observations of localization induced by the capacitive effect is seen at the top and bottom of (a).

between the center localizations and the main field running the length of the cavity, depicted by four light blue areas. Further study of the results exposed the small fields to be fringing fields coming off the nearest mechanical gaps. Inside each of the gaps was a very high electric field, uncovering the previously-unknown capacitive effect. The large field in the center of the cavity near the endcaps resulted from a large charge buildup at the ends of the vanes on their inner tip. The findings lead to an investigation of the capacitive effect, which, in turn, developed into a more comprehensive evaluation of symmetry breaking in microwave cavities (see Chapter 3.2).

Due to discovering the capacitive effect, the complex 3-dimensional model was created to further gauge how the phenomenon affects the cavity. The center component of the cross brackets and each vane in the complex model act as capacitors. Figure 4-8 shows images of $|\mathbf{E}|$ of the TM_{010} as resolved by the complex 3-dimensional simulations

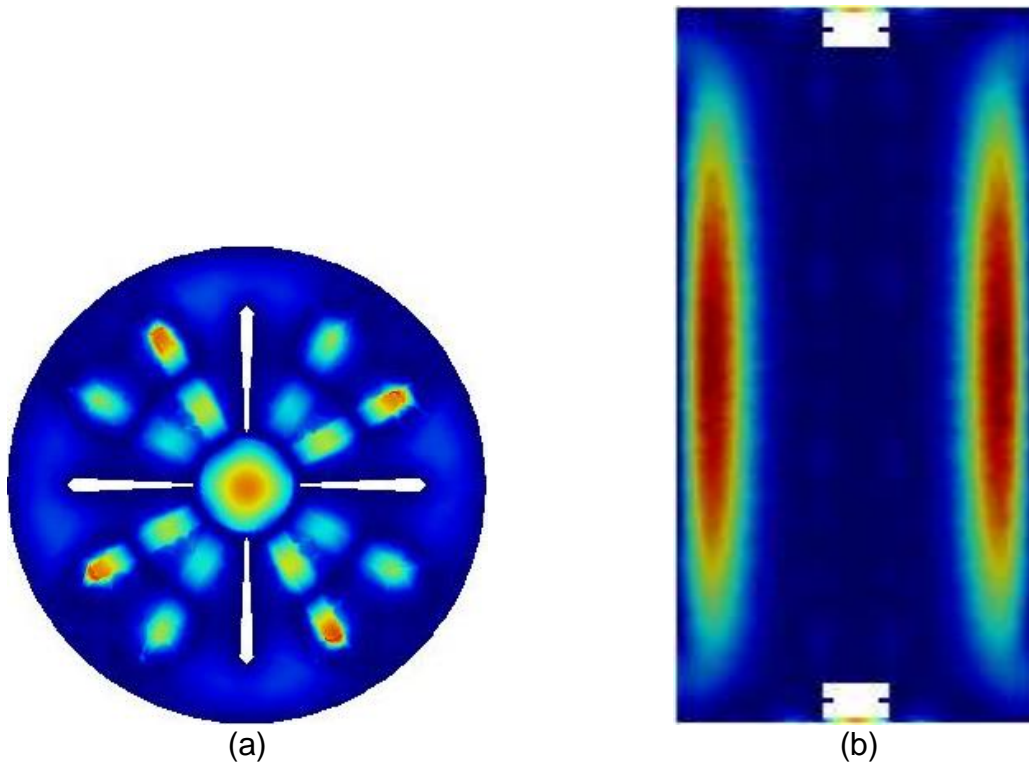


Figure 4-8. Cross-sectional images of $|\mathbf{E}|$ of the TM_{010} mode in the 12-vane prototype as resolved by the complex FEM simulation. (a) Through the x - y plane. (b) Through the z -axis and at a 45° angle to the x - z plane. The white areas are the conducting vanes in (a) and the center of the cross brackets in (b); a field solution is not included as there is zero field inside the conductor. The outer edge of the images and white areas are the conducting boundaries. Red indicates higher field and blue indicates lower field. (a) and (b) are not the same scale. The capacitive effect is visible in both images.

through a cross-section in the (a) x - y plane and (b) through the same plane as Fig. 4-7.

The model is in the maximum f_{010} frequency configuration. The x - y plane is cut through the center of the upper gap in (b).

Localization due to the capacitive effect can be seen in both images. In (a), each vane and the center section is a capacitor, and the cross-section shows localization between every rotating vane and the endcap as well as between the center of the cross bracket and the endcap. A blue ring can be seen depicting a node along a constant ρ , indicative of the subscript $m = 1$. This was the first prediction of mode hybridization

caused by symmetry breaking. In (b), the capacitive effect can be seen in the small mechanical gaps at the top and bottom of the cavity.

The model took ~24 hours to solve one vane configuration with only 20 modes, where the 2-dimensional model took ~1 minute to solve per configuration with 100 modes each. In an effort to reduce computation time, a convergence study was conducted. The resolution of the FEM mesh, measured in degrees of freedom (DOF) of the numerical problem, was varied to evaluate the computed f_{010} and C_{010} . The finer the mesh, the more DOF and the longer the computation time. Figure 4-9 shows the results of the convergence study. The plot shows that ~2M DOF are required to obtain convergence on frequency, and ~1M DOF are need for convergence of C . The simulation time was reduced to ~12 hours, but still very high for extensive modeling.

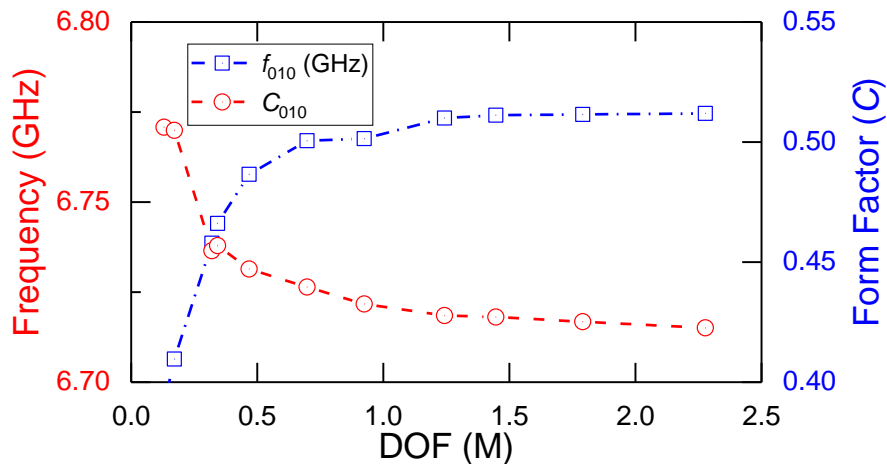


Figure 4-9. Plot of the results from a convergence study for the complex 12-vane FEM model. The number degrees of freedom (DOM) in millions is on the x-axis. The TM_{010} frequency (red) and form factor (blue) are on the y-axes.

A coarse mode-prediction was constructed to compare to the 2-dimensional model. The simulation computed an extremely high number of modes around the TM_{010} , far more than were measured (see Chapter 4.4). Figure 4-10 shows the coarse mode-prediction computed by the complex model. The frequency of 20 modes near the f_{010}

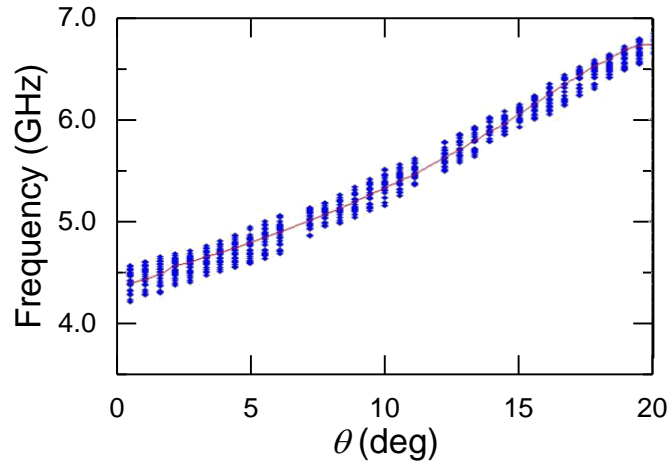


Figure 4-10. Frequency predictions for the 12-vane prototype from complex FEM simulations. The blue dots show the predicted mode frequencies at each interval while the red line traces the f_{010} . The vane rotation is shown on the x-axis. The modes are indistinguishable.

were calculated at 0.5° incremental steps. Due to geometry interference in the model when the cross brackets are closed, only $\sim 20^\circ$ of rotation could be simulated. The TM_{010} is identified by a red line. The two holes in the data are configurations where the model failed.

The modes are too close together to distinguish one from the other. Many of these modes are evanescent modes which would not be detected in the cavity prototype, while others are too low in power or have insufficient E_z field to be detected by the probe antenna. Regardless, the modes are computed by the simulations with no way of removing them, causing computational time to increase further for mode mapping. Additionally, identifying modes that would not be detected from the analytical results is extremely challenging and would require a significant exploration beyond the scope of this study.

Thus, the scientific and technical value of additional simulations of the 12-vane prototype were deemed not worthy of the time requirements presently. Additional

simulations on less complex structures need to be evaluated before such a complex structure as the 12-vane cavity should be considered for axion detection (see Chapter 6.1). Because the prototype testing demonstrated the complications of identifying and tracking modes in a periodic array cavity (see Chapter 4.4) and the issues caused in fabrication made simulating the cavity with sufficient accuracy not feasible (see Chapter 4.2), a complete mode-predict mapping across the entire tuning range from a 3-dimensional FEM simulation was never constructed. Mode predictions from the complex model were computed over limited range to support cryogenic testing (see Fig. 4.32).

4.2 Fabrication

The 12-vane cavity prototype utilized a stainless-steel tube that was electroplated [115] with oxygen-free high thermal conductivity (OFHC) copper as the cavity walls. The endcaps and vanes were made from pure OFHC copper. To allow for repeated access inside the cavity, a standard bolted interface instead of a knife-edge seal [107] was chosen to connect the endcaps to the cavity wall at a cost to Q . The decision removed the possibility of using the prototype for axion searches in the future, but enhanced the prospect for science discovery.

Figure 4-11 shows views from the drawings of (a) the cavity wall and (b) a vane. A cross-section of the side view of the cavity is shown, oriented with the z -axis horizontal. The profile of the vane is shown. The dimensions are shown in inches, which was used for fabrication in the U.S. The flanges on the cavity wall are used to connect the endcaps. The notes on the cavity wall are for electroplating and attaching the flange. The threaded holes in the vanes are used to connect to the endcaps for stationary vanes or the cross brackets for the rotating vanes.

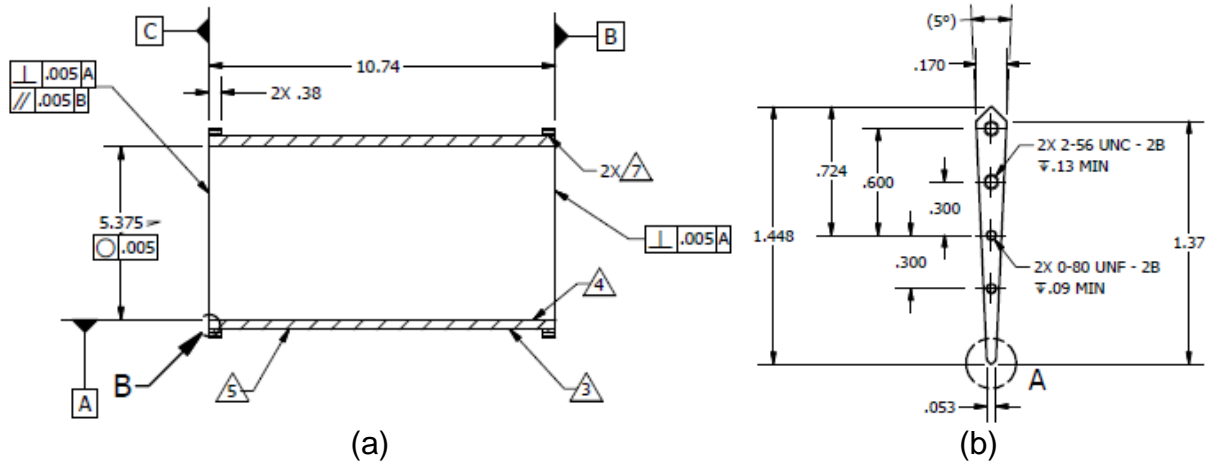


Figure 4-11. Select views from fabrication drawings of the 12-vane prototype. (a) Cross-sectional side view of the cavity wall. (b) Top view of a vane. Dimensions are in inches. The views are not to the same scale.

Several fabrication errors led to issues during testing. The boundary surfaces were intended to be electropolished to reduce surface resistance [116]. However, due to funding limits, the electroplating was made $\sim 10 \mu\text{m}$ thick, which is insufficient to electropolish as the entire coating could be removed in the process.

The vanes were wet-sanded with 1000-grit sandpaper to prepare for electropolishing. The electropolishing was conducted with Electro-Glo #200 [117] solution, but inadequate controls were used to maintain the proper surface current across the anode for polishing. OFHC copper polishing is highly sensitive to the current which is dependent on the surface resistance. But the surface resistance changes as the surface of the copper is polished [118], requiring a feedback system to obtain a proper finish. The temperature and flow-rate of the solution affect the surface resistance [119], which were not controlled during polishing. Lastly, the wedge-shape of the vanes made is more difficult to obtain an even surface current and to remove bubbles that form, which cause pitting. As a result, the current was often too high, causing pitting, or too low, causing etching or dulling. The endcaps were not electropolished as a result.

Figure 4-12 shows a plot of a generic electropolishing current density curve. The “best polishing” zone, between points C and D, for OFHC copper is narrower than typical metals and the zone moves due to surface polishing and/or heating more rapidly than typical metals. Figure 4-13 shows a photograph of four vanes assembled to two cross brackets. Some pitting is just visible on the outer tip of the vanes as small dots.

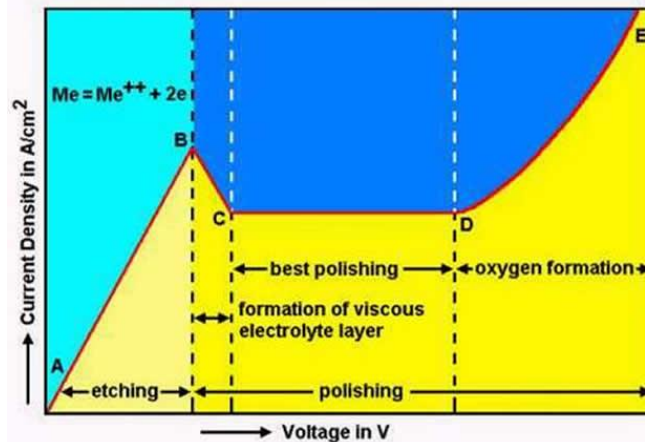


Figure 4-12. Plot of a generic electropolishing current density curve. The voltage applied is on the x-axis and the surface current density of the anode is on the y-axis. The “best polishing” zone is between points C and D. The zone is narrower for OFHC copper than for most metals.

ADMX electroplates stainless-steel tubes/rods with OFHC copper to fabricate their cavity walls and tuning rods. The experiment does not electropolish the cavity. Rather, the components of the cavity are heated individually at 400°C for 12 hours and cooled at room temperature [120]. The annealing causes the copper to soften, but the temperature is too low to significantly alter the stainless-steel stiffness; the stainless-steel maintains the shape of the electroplated parts. The process causes new grains to grow in the copper, destroying defective grains and yielding larger average grain sizes [121]. The result is a longer mean-free path in the copper and a lower surface impedance at the cavity boundaries.

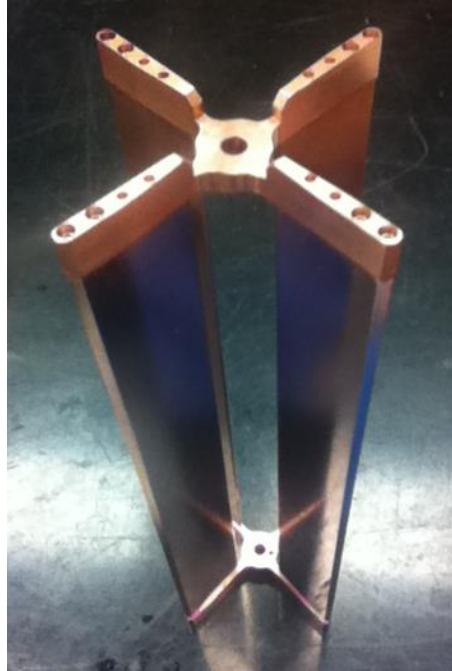


Figure 4-13. Photograph of four vanes partly assembled. The vanes are attached to two cross brackets at each end forming one 4-vane set. The tips of the vanes show some pitting.

The annealing process was performed on the 12-vane cavity prototype components. All parts were placed in an autoclave for annealing simultaneously. To conserve volume in the autoclave, the vanes were placed upright within the center of the cavity wall, with no supporting structure. Because the vanes are solid OFHC copper, the components softened at the annealing temperature and buckled under their weight. When the pieces cooled to room temperature, the vanes were noticeably curved along the longitudinal axis. Additionally, the process further dulled the finish of several vanes, causing severe discoloration.

The deformed vanes were used for the prototype testing, which led to a deeper understanding of longitudinal symmetry breaking in periodic array cavities, though not intentionally. Figure 4-14 shows a photograph of the vanes assembled together with the cross brackets and attached to the bottom-plate. The assembly is lying sideways.



Figure 4-14. Photograph of prototype vanes assembled to the cross bracket and the bottom-plate. The assembly is turned sideways from the operational orientation. The vanes are attached to two cross brackets on the left, with nominal 0.013 cm mechanical gaps. Significant discoloration from the annealing is visible on several vanes. The vanes are curved along the z-axis of the prototype (horizontally in the picture).

Discoloration from the annealing process is visible. The vanes are also curved, though not as obviously from the photograph. The mechanical gaps between the moving vanes can also be seen on the left side of the picture.

The annealing process improved the quality factor of the empty cavity. Prior to annealing, $Q = 11,800$ for the TM_{010} mode; after annealing, $Q = 15,100$. The theoretical quality factor is $Q = 34,300$. However, the Q of the cavity with the vanes was not measured prior to annealing due to disassembly issues with the design. The effect of annealing on the vanes' surface resistance is unknown.

The stationary vanes were fastened to the bottom-plate. The rotating vanes were attached to the crossing brackets and assembled to the bottom-plate via an idler shaft. An alignment pin was used to initially align the vanes in the maximum f_{010} frequency configuration. The cavity wall and top-plate was integrated and the drive shaft of the gearbox (see Chapter 4.3) was installed to hold the vanes location. Figure 4-15 shows a

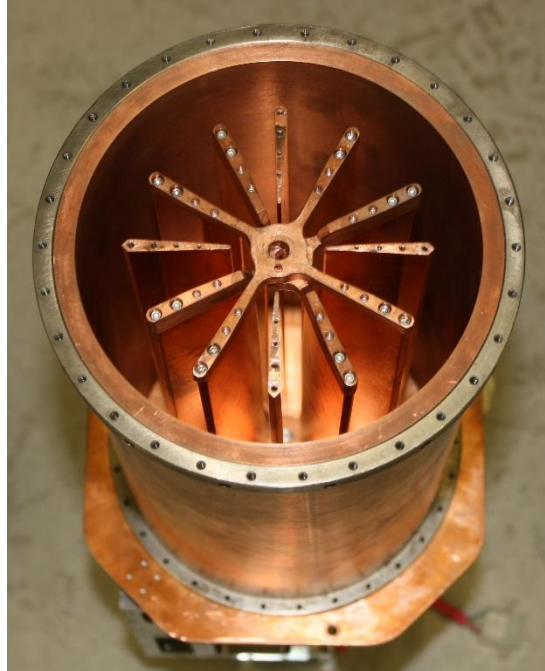


Figure 4-15. Photograph of prototype assembly with the top-plate removed. The vanes are in the initial alignment configuration.

photograph of the cavity prior to installation of the top-plate and gearbox, displaying the vanes in the initial alignment configuration.

Antennas were produced by exposing 1.5 mm of the center conductor of a rigid copper coax cable. All antennas were installed such that the cut in the cable was flush with the cavity boundary, similar to Fig. 3-4(a). The antenna coupling was intentionally made weak to minimize the perturbation effects to the cavity modes. The losses in the antennas were assumed to be the same.

The vanes were realigned by taking power measurement in the various cells and adjusting the vanes location to best-fit the predicted power values for the maximum f_{010} frequency configuration. As each vane subassembly moved as unit, only relative alignment could be achieved. The final alignment of the vanes was made by rotating all the vanes together clockwise and counterclockwise until the cluster contacted the

stationary vanes, and centering the subassembly between the two bounds. Due to physical interference of the cross brackets, the tuning rods could only be rotated $\sim 21^\circ$. Figure 4-16 shows a photograph of the prototype fully assembled, except the bottom antennas. Stands are attached to the cavity for testing, and part of the gearbox is visible on top.



Figure 4-16. Photograph of 12-vane prototype assembly. The bottom antennas have been removed. Four posts are used as stands for testing. Part of the gearbox is visible at the top.

4.3 Test Apparatus

The 12-vane cavity prototype was tested in room temperature, within a liquid nitrogen (LN_2) bath, and within a liquid helium-four (L^4He) bath. The test apparatus was composed of a cryostat that contained the prototype, a drive system and controls, and measurement instrumentation and a data recording system. Figure 4-17 shows a schematic of the apparatus. The schematic includes the mechanical systems such as

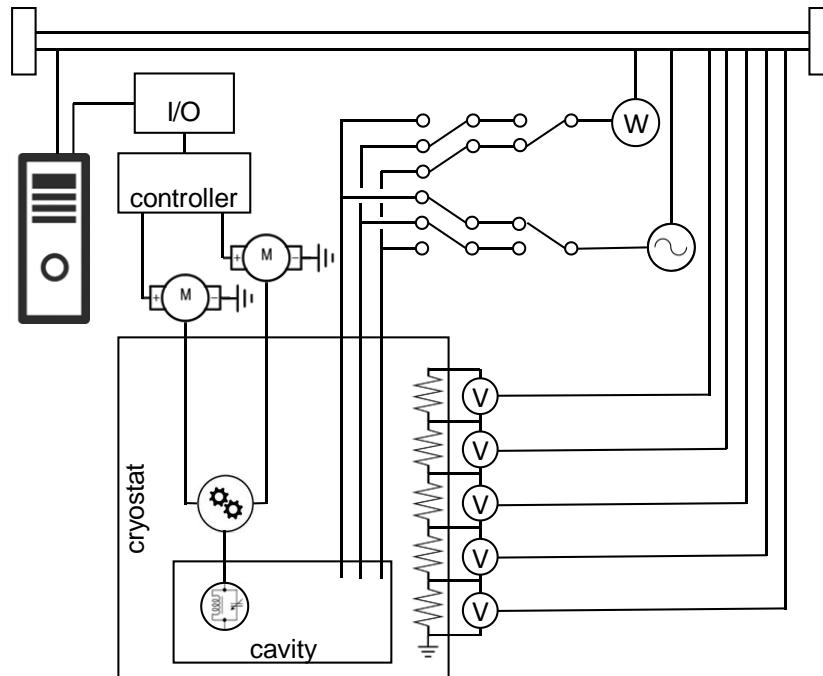


Figure 4-17. Schematic of 12-vane prototype test apparatus. A computer system controls the drive system and signal generator, and stores the instrumentation measurements. The data is transmitted over a GPIB while the drive system is controlled analogically. Only three antennas and associated switches are shown; the cavity has a total of eight antennas that the signal generator and power meter can couple to. Components are not to scale.

the motors and a gearbox, and the electrical components such as a power meter and signal generator. The tuning rods are represented by an adjustable LC circuit within a circle to symbolize the frequency-adjusting capability.

The cryostat is indicated by a labeled box. The temperature inside the box is at the test temperature while everything outside the box is at room temperature. The double lines at the top represent a general-purpose interface bus (GPIB). Only three antennas and two three-way switches are shown to simplify the figure; the experiment had eight antennas and two eight-way switches (see below).

The cavity prototype was attached at the bottom of a cryostat insert, which was sealed inside a vacuum dewar. The insert was designed for L⁴He bath testing, and

consisted of a top-plate, six radiation baffles, an aluminum interface plate to attach the cavity, and support structure. Five resistors were characterized at L⁴He (4.2 K), LN₂ (77 K), and room (300 K) temperatures. The resistors were attached at differing heights of the insert to serve as a liquid level detector. The resistances were measured with voltmeters, and the data was saved to the computer. The liquid/gas filling and evacuation of the cryostat was done manually.

The drive system was controlled by a computer using an analog input/output (I/O) device which applies voltages across a motor controller to operate two DC stepper motors [122]. The motors were mounted to the top of the cryostat and rotated two stainless-steel shafts that passed through the top-plate. The metal shafts were attached with flex couplers to G10 shafts [123] that passed through all the radiation shields of the cryostat. Teflon bushing were used to keep the G10 shafts in place.

The stepper motors had a single step size of 1.8°. The frequency step size of a haloscope cavity needs to be $< f/5Q_L$, so a gear reduction is required to meet the tuning requirements. The reduction required for cavity with a single tuning variable is estimated

$$\frac{1}{GR} > \frac{5Q_L}{f_{min}} \frac{f_{max} - f_{min}}{\theta_{max}} \theta_s, \quad (4-1)$$

where θ_s is the step size of the motor, θ_{max} is the maximum rotation of the vanes, f_{max} and f_{min} are the maximum and minimum frequencies of the search mode, respectively. A minimum gear reduction of ~1:10,00 was needed for the testing, assuming anomalous skin effects (ASE).

To enable finer adjustability, a gear reduction of 1:19,600 was used. The gearbox was divided into two sections, each composed of two worm-gear pairs [124] in series, for total of four worms/gears. The gears had 140 teeth each. The gearbox had two

separate input shafts, but the two output shafts were coaxial, allowing one gearbox to drive both 4-vane sets simultaneously. Anti-backlash gears were used to minimize the dead-space when reversing direction with the motors. Figure 4-18 shows a photograph of the gearbox. The gears are made of bronze to wear faster than the worms. The output shaft of the upper section is nestled in the output shaft of the bottom section; during operation, the shafts would rotate in opposite direction at the same rate.



Figure 4-18. Photograph of the gearbox for the 12-vane prototype. The gearbox was divided into two sections, each with two worm-gear pairs in series for a 1:19,600 gear ratio. The output shafts are coaxial.

The G10 shafts were attached to the gearbox input shafts with flex couplers to account for misalignments. The gearbox was attached to the top-plate of the cavity with three flex-rods to accommodate dissimilar thermal expansions at cryogenic temperatures. The coaxial output shafts penetrate the prototype through a center bearing (see Fig. 4-5(a)). The testing required 8 cable lines from each antenna to transfer the input and output signals, since the switches were outside the cryostat. To

reduce the thermal load, semi-rigid coax cables with beryllium-copper center conductors [125] were installed.

Figure 4-19 shows the cryostat insert with the 12-vane cavity prototype at the bottom. The top-plate of the insert is fixed to a frame; the dewar sits inside the pit beneath the insert (not visible), and was lifted by a hoist and bolted to the top-plate for cryogenic testing (see Fig. 4-20). The six radiation baffles sit below the top-plate. Three resistor rest on the baffles and one lies on the interface plate above the prototype. The gearbox is seen between the interface plate and the cavity. The cavity is attached below the interface plate with three rods. Eight flexible cables [126] connect the semi-rigid cables to the cavity antennas.

The testing required taking S_{12} measurements across a relatively wide frequency spectrum though the tuning range of the cavity. A signal generator [127] produced a narrow bandwidth signal at a frequency controlled by the computer system. A power meter [128] sensitive to 0.1 nW measured the average power across the bandwidth and transmit the data digitally to the computer. The process would be repeated over a frequency range to obtain a power spectrum at a given cavity configuration.

The signal generator and power meter could be connected to any of the eight antennas to obtain any S_{12} measurement combination. The switching of the connections was done manually. Antennas lines that were not being use as input or output ports were terminated at the cryostat top-plate. The test configuration did not accommodate injecting signal and taking measurements from the same port (S_{11}).

The motor drive and instrumentation was controlled using visual code written in LabVIEW version 2016 [129]. The code also identified modes using a peak-search



Figure 4-19. Photograph the 12-vane cavity cryostat insert. The top-plate of the insert is mounted to a frame. All electrical and mechanical feedthroughs are in the top-plate. The dewar is below the cryostat (not visible).

program with a minimum-power threshold and recorded the measurements from the power meter and voltmeter, as well as converted the resistance measurements to an approximate liquid level height. The liquid height was used to determine the test temperature and plan cryogenic operations.

Figure 4-20 shows the test apparatus with the insert sealed inside the orange dewar. The monitor of the control-computer is in the center of the picture and the computer sits behind it. Four voltmeters are on the left side of the screen. The signal generator is on top of the blue frame facing to the right; the power meter is hidden

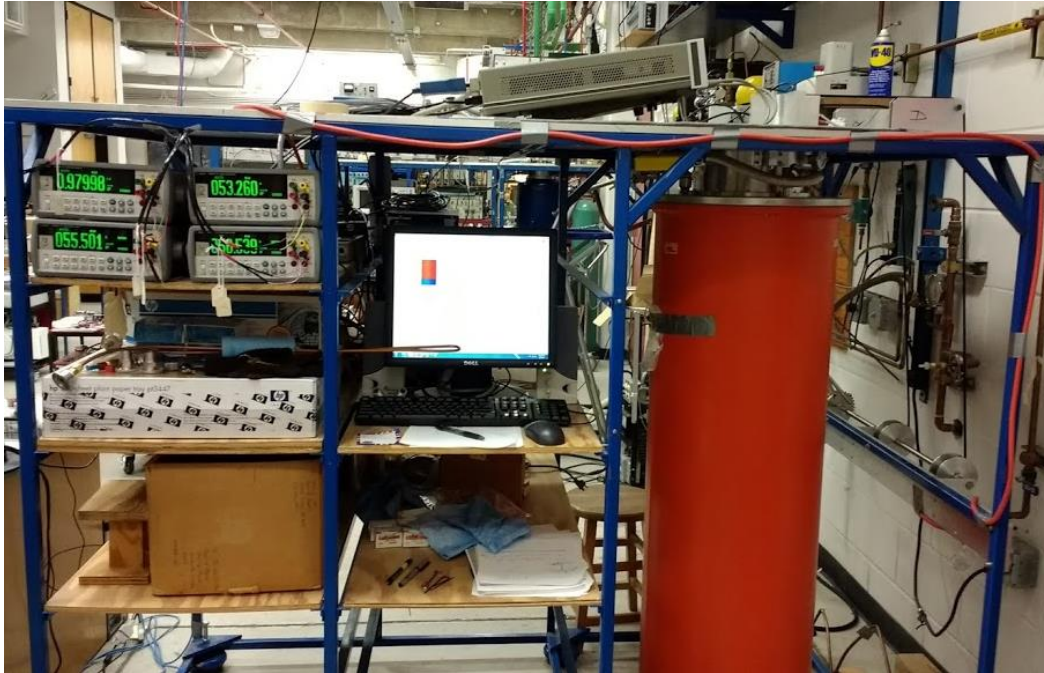


Figure 4-20. Photograph the 12-vane cavity test apparatus. The cryostat is on the right of the picture and the controlling computer is in the center. Four voltmeters (on the left) and the signal generator (at the top) can also be seen.

behind the signal generator. The motor controllers and I/O device are on the backside of the blue frame, not visible in the photo.

4.4 Test Results

The cavity prototype was initially tested at room temperature with only the four stationary vanes installed. The vanes run the length of the cavity, so no mechanical gap is present. Figure 4-21 shows an image of the predicted E_z field for the TM_{010} mode through a cross-section of the 4-vane cavity with the bottom antenna locations overlaid. The cross-section is parallel to the cavity axis. The white areas are the vanes with no field solution. The outer edge of the images and the white areas are the conducting boundaries. Red indicates higher field and blue indicates lower field, with zero field at the boundaries. Antenna ports G and H are on the top-plate in line with antennas B and E, respectively.

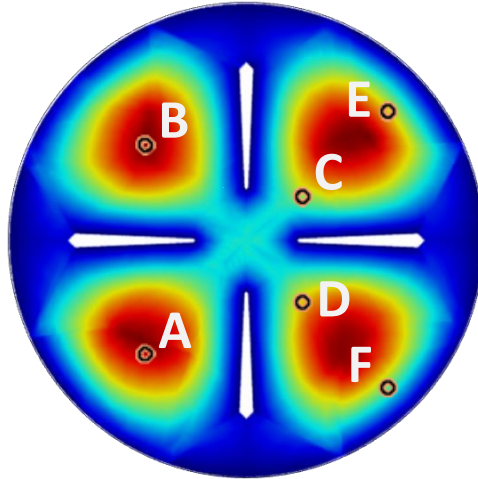


Figure 4-21. Cross-sectional images of the E_z field of the TM_{010} mode in the 4-vane cavity with bottom antenna positions overlaid. The cross-section is parallel to the cavity axis. The white areas are the vanes; a field solution is not included in the images as there is zero field inside the conductor. The outer edge of the images and white areas are the conducting boundaries. Red indicates higher field and blue indicates lower field with zero field at the conducting boundaries.

S_{12} measurements of the 4-vane cavity were made with a spectrum analyzer for various antenna input/output configuration. Figure 4-22 shows the power spectrum measurements of the 4-vane cavity for (a) S_{GA} , (b) S_{GB} , (c) S_{GC} , and (d) S_{GD} . The subscripts for the S_{12} measurements use the antenna location nomenclature to indicate the input (1) and output (2) antennas, respectively. The power is in dBm. The green vertical lines show the predicted TM eigenfrequencies from a 3-dimensional COMSOL [96] simulation. The predicted frequencies for the TM_{010} and TM_{013} are labeled.

The measurements provided several important findings that were gateways to understanding symmetry breaking effects. The most notable observation is all the modes detected could be identified as a TM mode from simulations, supporting the later discovery that mechanical gaps cause mode repulsions. Mode repulsions are seen only when TE/TEM modes are detected by the probe antenna, which is a result of mode mixing. Because no TE/TEM modes appeared to be detected by the probe antenna, no

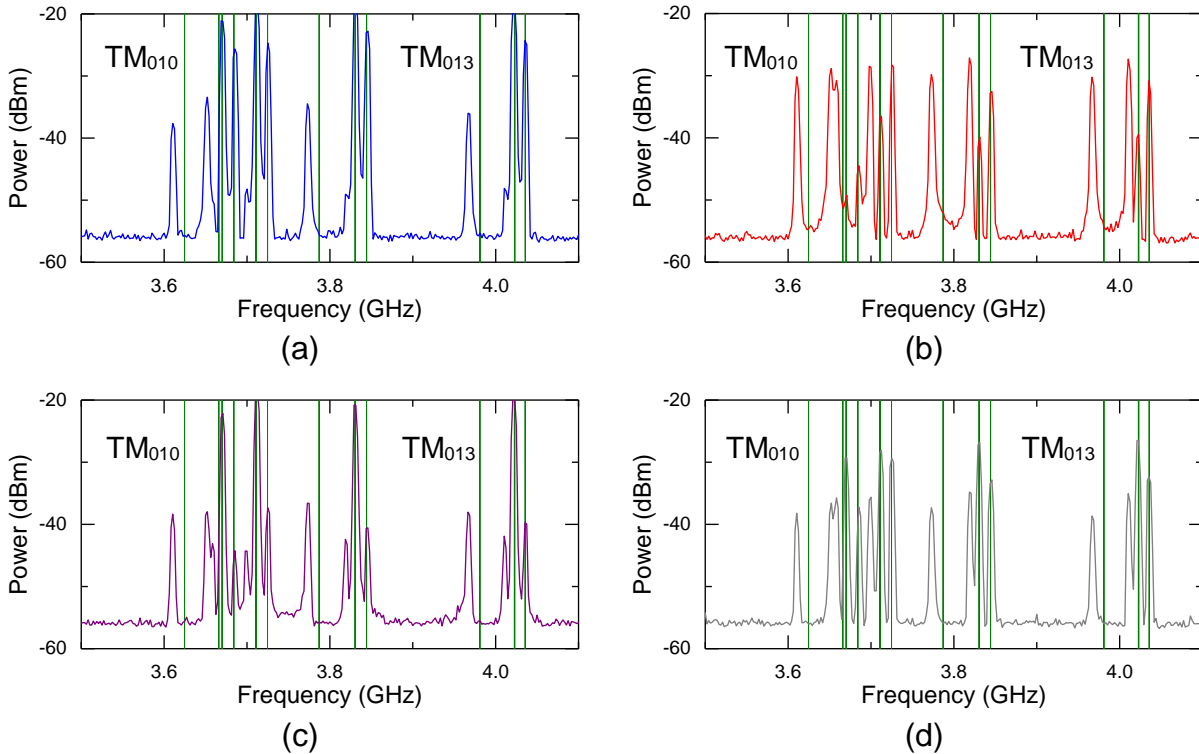


Figure 4-22. Power spectrum plots for the 4-vane cavity prototype. (a) S_{GA} . (b) S_{GB} . (c) S_{GC} . (d) S_{GD} . The predicted TM mode frequencies are shown as green vertical lines in all plots. The TM_{010} and TM_{013} mode predictions are labeled. The results helped explain various symmetry breaking phenomena.

mode mixing appears to be occurring. The conclusion of no mode mixing matches the predictions of simulations (see Fig. 3-13).

Most of the modes' peak power lined up closely to the predicted TM modes. However, all the TM_{01p} frequencies were lower than the predictions by ~ 15 MHz. The shift can be seen in the plots at the labeled modes. The lowest detected mode in the plots is the TM_{010} , which is 15 MHz less than the prediction. The mode to the left of the green line labeled " TM_{013} " is the TM_{013} mode, which is ~ 13 MHz less than predicted. Similar discrepancies are seen for the TM_{011} and TM_{012} modes.

The frequency shifts are due to a symmetry breaking that caused transverse localization, which always reduces the TM_{01p} mode frequencies, possibly due to the

curvature of some vanes. Modes with $m > 0$ oriented so that a node passes through the symmetry breaking, greatly reducing the localization effects (see Fig. 3-5) on their frequency. Degeneracy breaking was also observed for modes with $m > 0$ in several of the plots, further suggesting a break in the discrete rotational invariance.

The power measured for the broken degeneracies was different in each cell, and the power measured for the TM_{01p} mode in the S_{GB} channel was greater than the other channels. The discrepancies further demonstrate localization of the modes caused by symmetry breaking. Note, the B and G antennas are in the same cell, so power was lost transferring the signal from the injection cell to the other cells. However, the basic fingerprint of the modes is similar regardless of which antenna pair was used. This pattern was repeated in other measurement configurations, suggesting that the input and output ports of S_{12} measurements are significant in periodic array cavities.

After final assembly and alignment, the 12-vane cavity prototype was tested at room temperature. The initial test runs immediately showed that a much higher number of modes was detected by a weakly coupled probe antenna than were predicted. Figure 4-23 shows the power spectrum for the 12-vane prototype in the maximum TM_{010} frequency configuration (see Fig. 4-4(b)) for channels (a) S_{GB} and (b) S_{GE} . The predicted TM_{010} frequency from a 2-dimensional simulation is depicted as a vertical green line. The x-axis is power in mW on a log scale.

The 2-dimensional simulation predicted only two TM modes in the frequency range shown in the plots. The measurement showed ~20-30 modes. Though a few more modes with $p > 0$ were expected to be observed than predicted, the discrepancy was significantly more than anticipated. Also, the number of modes in the different cells

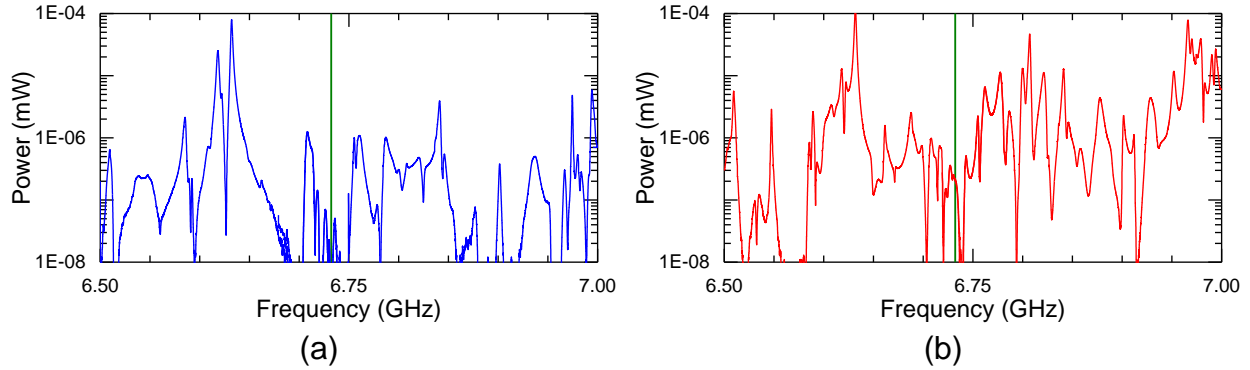


Figure 4-23. Power spectrum plots for the 12-vane prototype at room temperature. (a) S_{GB} . (b) S_{GE} . The predicted TM_{010} frequency is shown as a green vertical line. Power is shown on a log scale in mW.

were not the same and very few modes were seen in both channels. No mode appeared more or less likely to be the TM_{010} .

Several variables were eliminated as causes for the discrepancy. The injection and receiver chains were investigated for standing waves. A small number of standing waves were identified, but were determined not a significant contributor as they were not within the frequency range or did not have high enough energies to alter the power spectrum in the cavity. The non-operating antennas were removed and holes were plugged to identify power leaks or local localized modes, but the experiments showed no notable change in the spectrum. Terminations were removed from non-operating antennas which yielded inconsistencies in measurements, justifying the use of terminations on unused antennas.

Two 3-dimensional simulations were developed to identify the unknown modes (see Chapter 4.1). However, the complex simulations demonstrated that ~ 100 modes existed in the frequency range of the measurements and small adjustments to the model moved modes up and down in frequency significantly. The curvature of the vanes was never measured, as the expectation of their impact was not significant prior to the

testing. Because the exact geometry of the as-built prototype was not known, properly modeling the cavity to identify the modes was impossible. Even bounding the symmetry breaking would yield no valuable data, as the frequency range of a single mode within the bounds would overlap many other modes, making them indistinguishable from S_{12} measurements alone.

Simulations were also used to predict which modes were more likely to couple to a probe antenna with no success. The coupling of the non-TM modes to a probe antenna was discovered to be caused by modes mixing with TM modes. But the mixing of the modes was highly sensitive to the symmetry breaking. Without exact geometry inputs for the simulation, predicting which TE/TEM modes mixed with TM modes was not possible, providing no value in mode identification. The finding, however, was significant and contributed to a deeper understanding of the effects of symmetry breaking (see Chapter 3.2).

Measurement mode maps were developed using the threshold method. Figure 4-24 shows mode maps for the entire tunable range of the 12-vane prototype for channels (a) S_{HE} and (b) S_{HF} . The maps are typical of the channels. The tuning is from the minimum TM_{010} frequency configuration, dictated by the interference of the cross brackets, to the maximum TM_{010} frequency configuration.

The maps show the S_{HE} channel is more mode-dense than the S_{HF} channel, showing how localizations cause varying results in different cells. It is not clear if the modes measured in one channel and not another are too low in power or just don't couple to the antennas sufficiently in the cells where they were not observed. Note, antennas E and H are in the same cell, suggesting that power was a factor in the

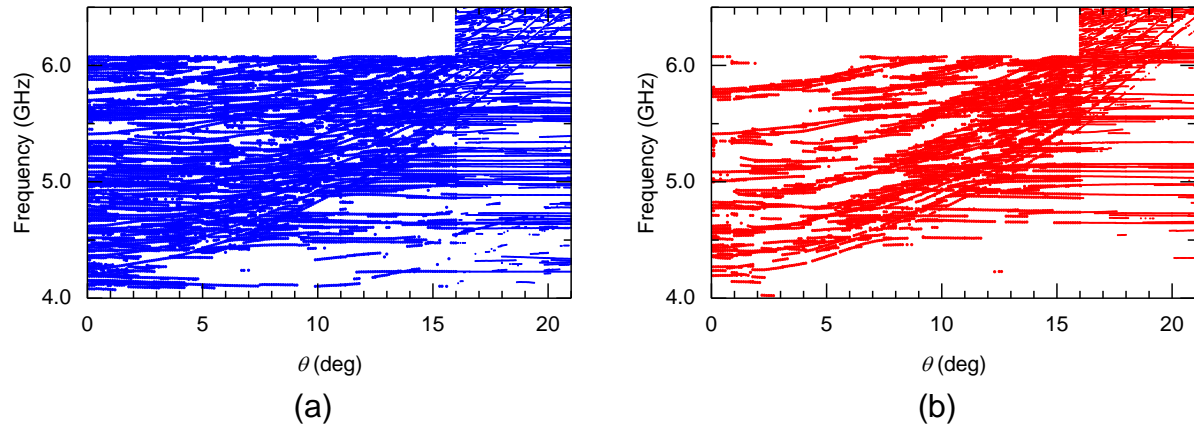


Figure 4-24. Mode maps for the 12-vane prototype. (a) S_{HE} . (b) S_{HF} . The vane rotation is on the x-axis in degrees, where 0° is the minimum TM_{010} frequency configuration. The threshold method is used to identify modes. Analytical predictions are not shown.

measurements. The results again showed that the location of the input and output antennas are not negligible in exciting and detecting a mode, and would not be trivial in an axion search.

Tuning of several modes is seen in the maps; this is the first known demonstration of tuning a microwave cavity using vanes. The lowest frequency mode, which tunes (~ 4.2 - 6.3 GHz) is believed to be the TM_{010} , but being the lowest frequency does not guarantee the highest form factor (see Chapter 3.2). Without additional confirmation, the TM_{010} is not sufficiently known to ensure adequate sensitivity for axion searches. The lowest frequency mode that is tuned does not align well with the 2-dimensional or 3-dimensional predictions, and has several very large gaps in the map, especially in the S_{HE} channel.

Figure 4-25 shows the mode maps from Fig. 4-24 together, zoomed in on the lower left corner. The 2-dimensional TM_{010} frequency predictions are shown in green. The lowest tuned mode lines up well between the channels, but in much of the tuning

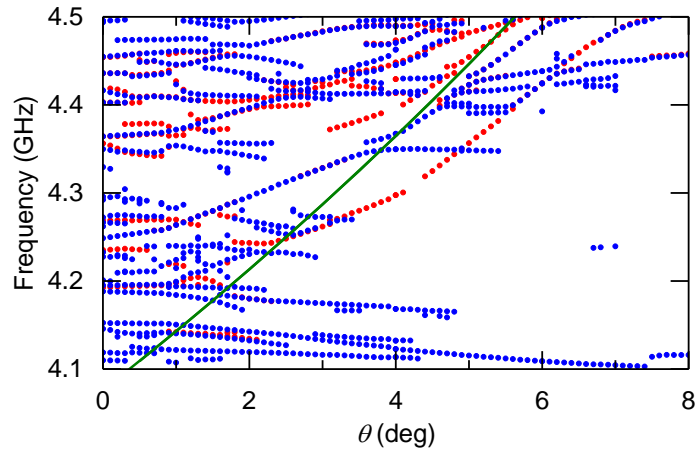


Figure 4-25. Mode map for the 12-vane prototype for channels S_{HE} and S_{HF} . The vane rotation is on the x-axis in degrees, where 0° is the minimum TM_{010} frequency configuration. 2-dimensional analytical predictions are shown as a green line.

range shown, only one of the channels detects the mode. The mode does not align well with the predictions. Many mode crossings are seen, as are some mode repulsions.

Because the threshold method of identifying mode peaks can miss modes when the peak is below the threshold, color-plot mode maps were constructed to determine if the lower frequency tuned modes are more observable throughout the tuning range.

Figure 4-26 shows the color-plot mode map for the 12-vane cavity prototype for channels S_{GA} and S_{GB} . Light yellow is higher power and dark blue is lower.

As seen before, the cell with the injection port has recorded higher power than the other cell. Mode repulsions are more visible than in Fig. 4-24, as seen by the vertical lines that disrupt the tuning modes. However, no additional information was presented in the color-plots that aided mode identification. In particular, holes in the maps did not appear to be just below the threshold, but seem to be not present in the measurement at all. The lowest mode appears to completely vanish above 4° in channel S_{GB} and has

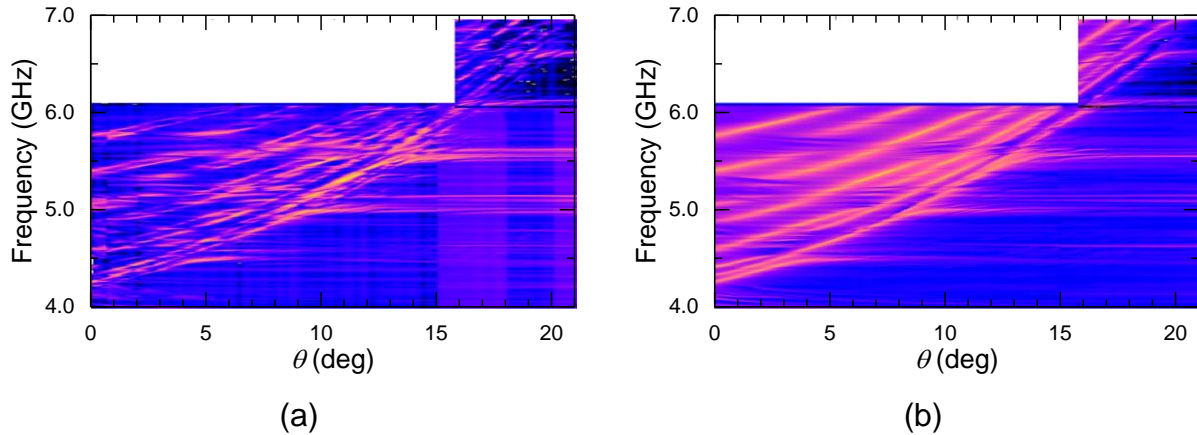


Figure 4-26. Color-plot mode maps for the 12-vane prototype. (a) S_{GA} . (b) S_{GB} . The vane rotation is on the x-axis in degrees, where 0° is the minimum TM_{010} frequency configuration. Analytical predictions are not shown.

many large holes in S_{GA} . If this mode were the TM_{010} , it would be unusable for axion searches as is.

Perturbation techniques for mode identification (see Chapter 3.3) were implemented to determine the TM_{010} mode. A copper rod was inserted in $\sim L/4$ increment into various cells to determine which modes increased in frequency. The technique was not able to distinguish modes very well. Specifically, vane configurations where mode repulsions did not occur in one cell often occurred in another, so it was not possible to separate TM modes from mixed modes and the process resulted in data that could not be correlated between cells.

A coarse bead-pull test was also conducted. An alumina bead about 1 mm in diameter was translated in the cavity z-axis in increments of $\sim L/10$. The results were too coarse and inconsistent to yield meaningful results. A more sophisticated experiment was considered, but was decided not worthy of the time investment. The apparatus for the experiment was not local and the set-up is extremely involved. Due to the extensive symmetry breaking causing a lack of equivalency in the cells, a fine bead-pull

experiment seemed no more probably to identify the TM_{010} , yielding likely zero fruit for considerable time.

Mode correlation was also attempted. By assuming a mode is the TM_{010} , higher-order TM modes could be estimated based on Eq. 3-16. The mode calculations are compared to the measurement at various tuning configurations to determine if any combination provides a superior match in modes. The process did not positively identify the TM_{010} .

Because of the failed attempt to identify the TM_{010} mode conclusively, and the growing awareness of the need for a nonperturbative in-situ mode identification technique, the in-situ mode test was developed (see Chapter 5). However, though the process was proven with cavities where no longitudinal symmetry is broken, it was not able to positively confirm the TM_{010} mode. After all mode identification methods were exhausted, the TM_{010} was not identified with sufficient confidence need for an axion dark matter search. Because a significant information about advanced tuning of microwave cavities had been obtained, the planned testing was continued to glean any further knowledge from the prototype.

The frequency step size was measured over a short tuning range. Figure 4-27 shows the frequency tuning for the smallest vane rotation of the apparatus for channels S_{HE} and S_{HF} . The rod was rotated $\sim 0.002^\circ$ around $\theta = 14.25^\circ$. The mode shown is the third lowest tuning mode. The mode and the form factor of the mode are not known. The mode and vane angle were selected because the tuning was identifiable and no mode crossing was observed. The average frequency step size for the prototype at the configuration was $\Delta f \approx 9$ KHz, below the required $f/5Q_L \approx 27$ KHz using the theoretical Q

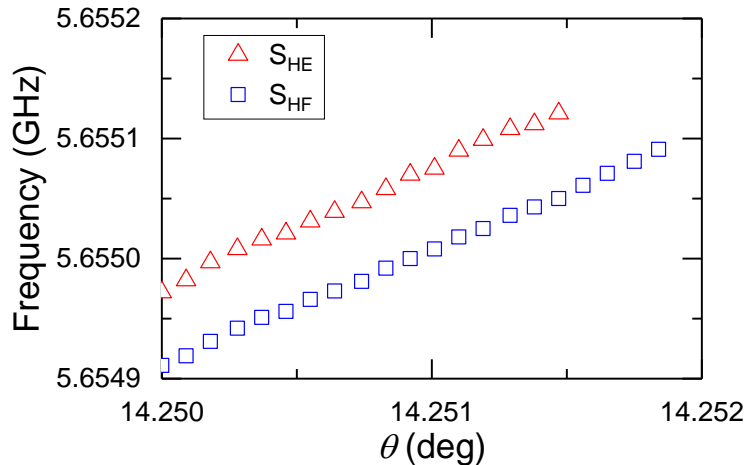


Figure 4-27. Plot showing the frequency step size of the 12-vane prototype. Channels S_{HE} and S_{HF} are shown. The vane rotation is on the x-axis in degrees, where 0° is the minimum TM_{010} frequency configuration. The average minimum step size is ~ 9 KHz. Q_L of the measurements was ~ 1200 .

value in ASE. (Q for the prototype was much less than the theoretical value, discussed below.)

The step size plot clearly demonstrates the frequency mismatch between cells. The mode in the two channels are believed to be the same, but their peak frequencies are ~ 70 KHz different due to symmetry breaking between the cells. The measurements in both channels were taken simultaneously. The frequency mismatch would cause a reduction in power generated by the axion conversion, on the order of Eq. 3-37.

Effectively, the cells can be considered individual cavities with the area that joins them as short waveguides that couple the cavities. When the area is zero, the cavities are completely decoupled, allowing the modes to be completely distinct in each cavity. When a hole is introduced between cavities, similar modes begin to couple, forcing their frequencies closer together even when geometrical difference exist. When the partition between the cells is removed, a single empty cavity remains (i.e., complete coupling).

The 12-vane prototype demonstrated partial coupling, but consistently, measurements of what appear to be the same TM mode had slightly different frequencies in the cells. The discrepancies are exacerbated due to mode repulsions. TE/TEM modes in the cells were also not at the same frequency, so mode repulsions would occur at differing frequencies in the cells. When a slightly higher frequency TM mode begins a mode repulsion at a vane angle lower than the other cells, the mode repulsion will drive the TM mode frequency even higher relative to the other cells, making the variation greater.

Figure 4-28 shows the power spectrum of the 12-vane prototype for the third lowest tuning mode across a small frequency range. The vanes are at $\theta \approx 14.0^\circ$. Channels S_{GA} and S_{GB} are shown in red and blue, respectively. The curved lines are the power spectrum and the vertical lines identify the peak power of each channel, coordinated by color. Difference between the peaks is $df \approx 300$ KHz. If such a discrepancy was observed within a high- Q cavity, it would be of order f/Q_L . The measurements were taken simultaneously.

The mode is at a mode repulsion in the cell with antenna A, but not in the cell with antenna B. A TE mode is to the right of the plot in both channels (not shown), but it is only mixing with the S_{GA} channel, pushing the peak frequencies farther apart. This has the effect of further widening the hole in the frequency search spectrum of a detector than would exist with transverse symmetry maintained. However, this phenomenon could only be detected with multiple antenna ports, which suggests that multiple antenna ports are necessary for testing periodic array cavities. Multiple antennas are also necessary for the in-situ mode test (see Chapter 5).

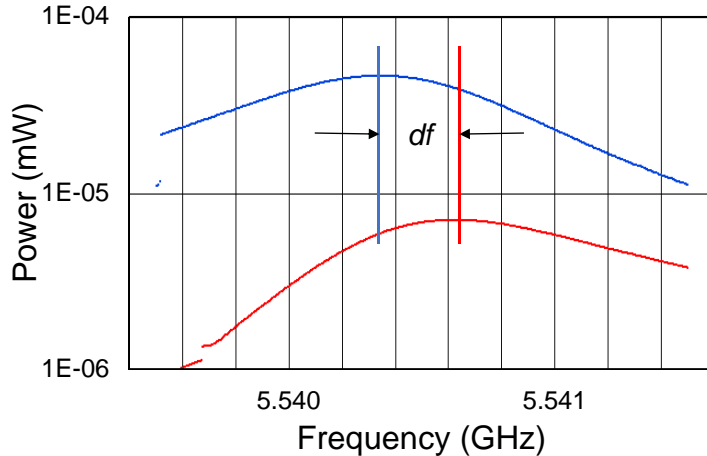


Figure 4-28. Power spectrum plots for the 12-vane prototype showing frequency discrepancies of a mode. Channels S_{GA} and S_{GB} are in red and blue, respectively. Power is shown on a log scale in mW. The different between the frequency peaks is ~ 300 KHz.

The 12-vane prototype testing was conducted in a LN_2 bath to verify the apparatus for L^4He testing. Frequency shifts in the modes due to the change in the dielectric constant was used to ensuring the cavity was submerged in the bath and validate the level detector. At LN_2 temperatures (77 K), one of the drive systems locked. Modifications to the cryostat insert were made to minimize friction, but did not relieve the problem. The rotation speed of the motors was reduced to increase their torque. This foreshadowed issues that would occur during L^4He testing.

Tuning was verified at LN_2 temperatures and Q_L was measured (see below). A small range of tuning at $\sim 14^\circ$ was verified for the third lowest tunable mode because tuning was clearly identifiable. Figure 4-29 shows the mode tuning for channels (a) S_{HD} and (b) S_{HE} . Other channels showed the tuning but less clearly. The mode is labeled TM_3 to indicate the third lowest (assumed) TM mode; the subscripts have no relation to the conventional m , n , and p subscripts.

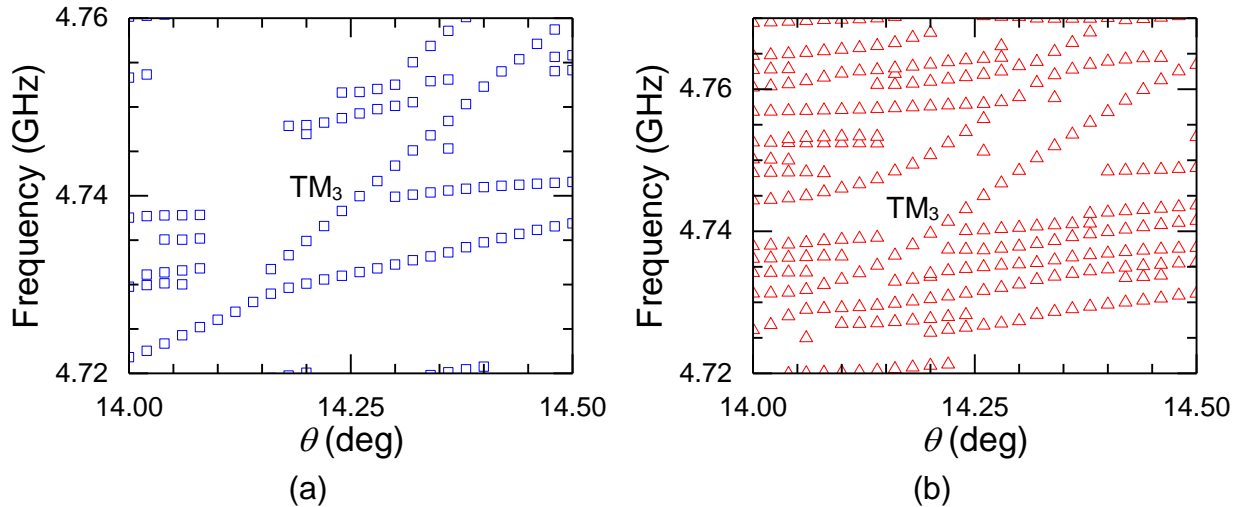


Figure 4-29. Partial measurement mode map in a LN₂ bath for the 12-vane prototype. (a) S_{HD}. (b) S_{HE}. The vane rotation is on the x-axis in degrees, where 0° is the minimum TM₀₁₀ frequency configuration. The third lowest tuning mode is labeled TM₃. Analytical predictions are not shown.

The frequencies are lowered by the refraction index of LN₂, which is 1.199 at the boiling point [131]. A mode repulsion is visible in channel S_{HD} around 14.15° (4.73 GHz) and in S_{HE} around 14.05° (4.73 GHz). Note, as the mode repulsions are at differing vane angles, the frequency mismatch of the mode between the cells will be enlarged as in Fig. 4-28 in the repulsions. Because antenna E and H are in the same cell, the power of the modes was larger in S_{HE} than S_{HD}, resulting in more modes exceeding the threshold. Adjusting the threshold for modes for different channels was not performed. Adjusting the threshold for periodic array cavities depending on the antenna location, cell coupling, and symmetry breaking will be necessary for axion searches.

The LN₂ tests were repeated in L⁴He to confirm tuning near axion search temperatures and compare Q_L measurements across temperatures. The level detector was used to confirm the temperature of the cavity. Figure 4-30 shows the resistance measurements of the four resistors on the insert during a L⁴He fill. The resistors are numbered by height from top to bottom of the insert, at ~18 cm intervals. The cavity sat

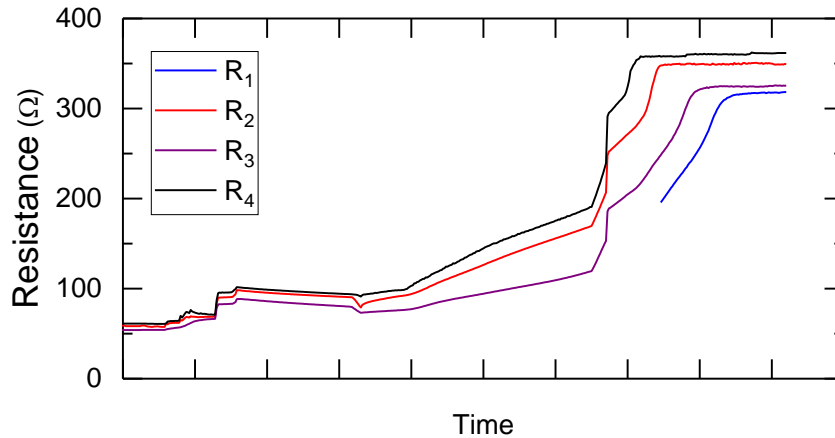


Figure 4-30. Cryostat level detector reading during a L⁴He fill. The resistors are labeled by location from top to bottom. The time scale is arbitrary. The cavity sat below R₄. When the resistance is constant, the liquid level is above the resistor.

~40 cm below R₄. The fifth resistor sat at the bottom of the dewar and was not recorded during testing. When the measured resistance is constant, the resistor is submerged in the liquid. Resistance of R₁ was not recorded until R₄ was submerged. The resistances were also compared to characterization data to verify the values were as predicted.

At L⁴He temperatures (4.2 K), the same motor that locked up during the LN₂ testing again locked up. However, reducing the motor speed did not allow the motor to drive the vanes and the testing was conducted with only one 4-vane set rotating during the tuning measurements. After cryogenic testing, the motor was verified operational at full speed at room temperature and at an estimated 240 K, based on resistor readings and characterization.

Figure 4-31 shows the maximum motor speed verses temperature for the motor that locked. The maximum speed capability is 60 RPM. The results show a linear relationship with temperature suggesting a misalignment due to thermal mismatch or some semi-viscous fluid (e.g., grease) solidifying. As the drive system was inspected multiple times for wear and any signs of high friction were removed, the gearbox is most

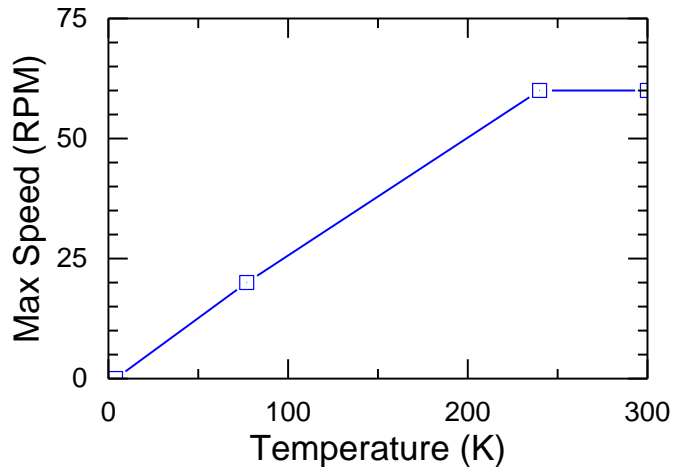


Figure 4-31. Maximum motor speed of the failing motor as a function of temperature. The temperature at ~240 K was estimated based on resistor measurements.

likely the cause for the lockup. No grease was used intentionally in the gearbox, but was used for vacuum sealing the cryostat and may have gotten into a gearbox accidentally. Additional testing of the gearbox has not been conducted to confirm the issue, as it was deemed unnecessary at the present time.

Analytical predictions for the L⁴He testing were computed using the complex FEM simulation [96] (see Chapter 5.1) for the tuning range used in the cryogenic testing. However, the predictions were based on all rotating vanes moving and do not correlate to the test results. As the modeling time is considerably long (see Chapter 4.1), time did not permit computing analytical predictions with only one vane set moving.

Figure 4-32 shows the analytical predicts from the complex model. The TM₀₁₀ mode is identified as red triangles. A few mode crossings and mode repulsions are seen in some of the tuned modes, but the simulation step size was too coarse to clearly discern crossings from repulsions. The frequency is reduced by 1.026 to account for the refraction index of L⁴He [132].

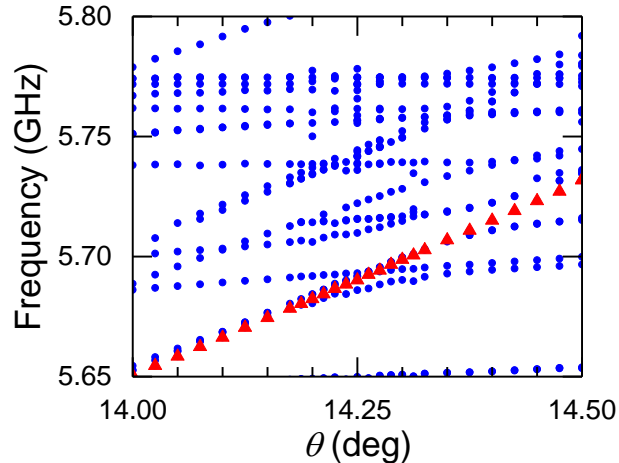


Figure 4-32. Analytical predictions for the 12-vane prototype during L⁴He testing. The vane rotation is on the x-axis in degrees, where 0° is the minimum TM₀₁₀ frequency configuration. The predictions are based on the complex model and rotate both set of vanes as designed.

The tuning of the cavity (df/θ) measured during the LN₂ testing was $\sim 2/3$ that of the model predictions. To account for only one vane set rotating, measurements were made with the unmovable vane set fixed at $\theta_2 = 14.0^\circ$ and $\theta_2 = 14.25^\circ$ while the other set tuned the cavity. Thus, the tuning observed during the L⁴He testing was $\sim 1/2$ that of the LN₂ tests, but the tuning was not observed across the entire vane rotation in most channels.

Figure 4-33 shows the mode tuning for channels (top) S_{HE} and (bottom) S_{HB} with θ_2 fixed at (left) 14.0° and (right) 14.25°. The vane rotation on the x-axis is for the vane driven by the motor (θ_1). The third lowest tuning mode is labeled TM₃. The plots are not to the same scale, as changing the non-moving vane set will shift the tuning range of the modes. Additionally, relocating θ_2 was done manually, so some repeatability errors occurred, causing select test runs to not align well with others.

Tuning was observed in all cells and with all channels measured, but some channels observed TM₃ noticeably less across the vane rotation. For example, TM₃ is

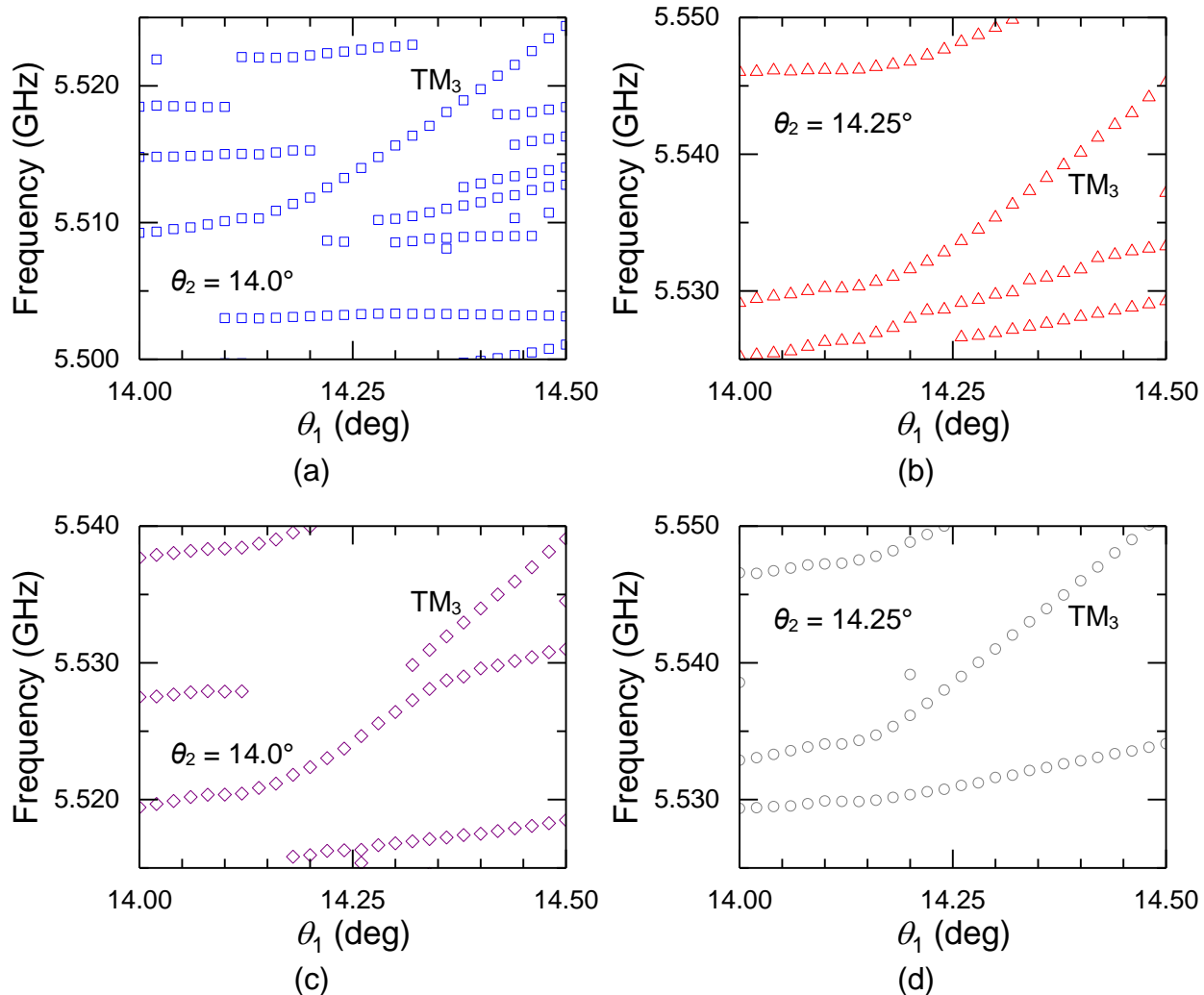


Figure 4-33. Partial measurement mode map in a $L^4\text{He}$ bath for the 12-vane prototype. (a) S_{HE} with $\theta_2 = 14.0^\circ$. (b) S_{HE} with $\theta_2 = 14.25^\circ$. (c) S_{HB} with $\theta_2 = 14.0^\circ$. (d) S_{HE} with $\theta_2 = 14.25^\circ$. The vane rotation for only one 4-vane set is on the x-axis in degrees, where 0° is the minimum TM_{010} frequency configuration. The third lowest tuning mode is labeled TM_3 . The plots are not to the same scale. Analytical predictions are not shown.

not observed in (a) at $\theta_1 < 14.15^\circ$. The reason for the disappearance of the mode in one cell is not precisely known, though the root cause is breaking discrete rotational invariance. Mode repulsions are seen in (b), (c), and (d). Tuning below $\theta_1 \approx 14.2^\circ$ was very limited in all channels.

The quality factors of the cavity were measured at various configuration during the tests. Table 4-1 shows the measured quality factor at the three test temperatures for the third lowest tunable mode. The vane sets were both at $\theta = 14.25^\circ$ during the measurements. The measurements are Q_L with weakly coupled input and output antennas, so the value will be close to the unloaded Q . The measurement for S_{HF} at 4.2 K is blank because the mode was not observed in the configuration during L^4He testing.

Table 4-1. Quality factors of the 12-vane prototype for different channels during testing.

Channel	Q_L (300 K)	Q_L (77 K)	Q_L (4.2 K)
S_{GA}	920	3131	4302
S_{GB}	968	3719	4073
S_{HC}	1665	2676	4278
S_{HD}	1439	3085	3968
S_{HE}	1161	2594	3453
S_{HF}	1373	2829	N/A

The theoretical Q for room temperature and 4.2 K is $\sim 15,000$ and $\sim 83,000$, respectively. The increase in Q at low temperature is due to ASE (see Chapter 3.1). The table shows that the measured Q is more than an order of magnitude lower than predicted. Figure 4-34 shows the measured values for channels S_{GB} , S_{HC} , and S_{HE} from the 12-vane prototype testing. A gain of $\sim 3-4$ in Q_L was achieved at 4.2 K, revealing the cavity boundaries entered the ASE regime, despite extensive issues during fabrication.

The prototype testing demonstrated the first cryogenic tuning of a periodic array cavity using vanes, though the results were modest. Tuning was less than predicted and mode crowding made identifying the TM_{010} mode impossible with current technology. Significant findings from simulations were supported or confirmed by the results of the tests, such as longitudinal symmetry breaking is the mechanism for mode mixing and frequency decoupling between cavity cells is enhanced by variances in mode repulsion frequencies between cells.

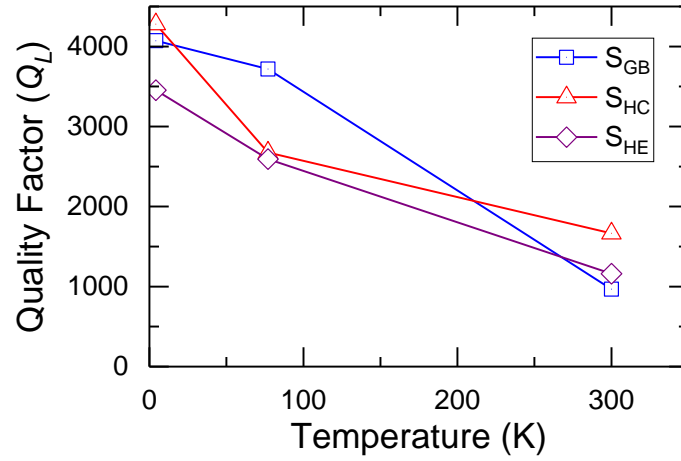


Figure 4-34. Measured Q_L of the 12-vane prototype versus temperature. Channels S_{GB} , S_{HC} , and S_{HE} are shown. The vanes are at $\theta = 14.25^\circ$. The cavity boundaries entered the ASE regime.

CHAPTER 5 IN-SITU MODE TEST

5.1 Test Methods

Based on the results of the 12-vane prototype testing at room temperature and high-frequency axion searches conducted by HAYSTAC and ADMX, an in-situ mode identification method was developed. The method compares the power measurements from combining the signal in two antenna lines to measurements from the lines individually. The comparison provides information about the local phase and relative power of modes at the antenna locations. Repeating the process with multiple antennas pairs at various locations provides a mapping of modes within the cavity at a given tuning configuration. Pass-fail criteria based on the analytical predictions are used to determine the desired search mode.

Probe antennas respond primarily to the electric field parallel to the probe axis (see Fig. 3-4). In a haloscope cavity, the probe must be oriented parallel to the externally applied magnetic field, because the electric field in the cavity must be oriented in the same direction (see Eq. 2-10), typically defined as the z-axis. For cylindrical haloscope cavities, probe antennas are mounted to the endcaps.

At every location on the endcaps, E_z is either in-phase, 180° out-of-phase, or nonexistent (for TE/TEM modes) due to the boundary conditions (see Chapter 3.1). The phase of the field is dependent on the mode configuration. For the TM_{010} mode, the signal extracted by weakly coupled antennas at any point on the same endcap will be effectively in-phase, while weakly coupled antennas on opposing endcaps will be effectively 180° out of phase. Slight discrepancies will occur due to the differences in

coupling. The use of weakly coupled antennas will typically keep the discrepancies below the error bars of the measurement, as well as minimize perturbations.

For higher-order TM modes in cylindrical cavities, the phase will be dictated by the mode order. For example, modes with even values of subscript p will yield 180° out-of-phase signals extracted by two inline antennas on opposite endcaps, while modes with odd values will yield in-phase signals from the same antennas. The m and n subscripts will dictate the phase of signal extracted from the same endplate, but in a more complicated way than the p subscript. In general, the number of nodes between two antennas determines the phase, with an odd number producing in-phase signals and an even number producing 180° out-of-phase signal. However, with tuning rods, the mode configurations become complex, and the previous “rule” does not always hold. Simulations are then required to determine the phase of the signals.

By predicting the phase of signals at various antenna ports, patterns can be determined that can be used to discern a search mode from other modes. In particular, the TM_{010} mode often maintains known parity symmetries that can be exploited for mode detection. Figure 5-1 shows images of the E_z field of the TM_{010} mode through a cross-section of various tuned cavity geometries and illustrates the symmetries. The symmetries provide ideal mode configurations the in-situ measurements to identify the mode. Antennas on the same endcap at points of symmetry would extract identical signals, providing confirmation of the mode.

Signals extracted from symmetry points of a TM_{010} mode on the same endcap would combine coherently if the cable lengths between the antenna and combiner are identical. The combined power would be double the power from a single antenna. Using

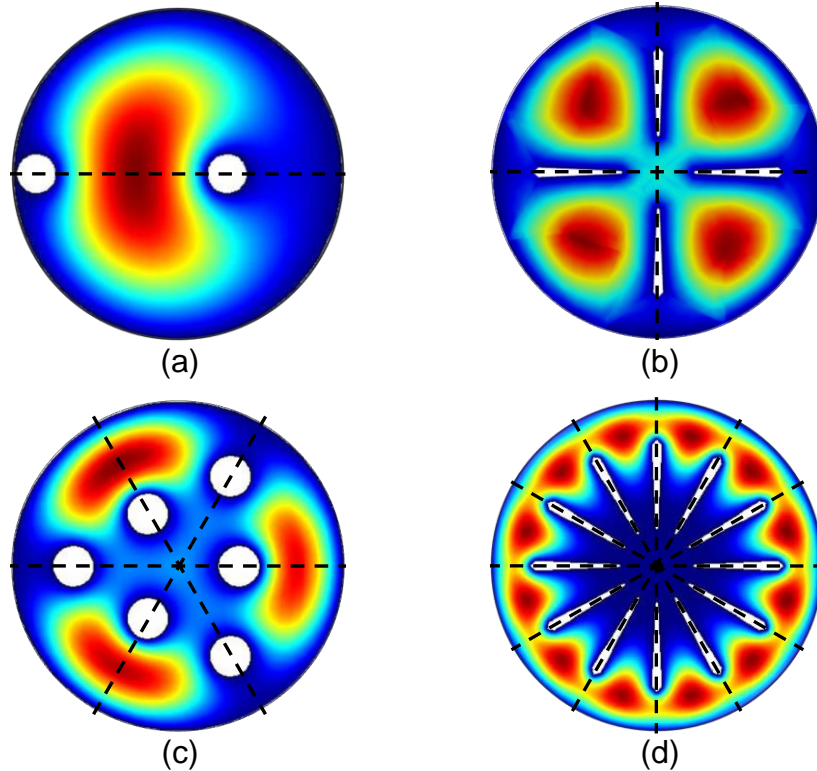


Figure 5-1. Cross-sectional images of the E_z field for the TM_{010} mode in cylindrical cavities with various tuning configurations depicting parity symmetries. (a) Two conducting rods. (b) Four conducting vanes. (c) Seven conducting rods. (d) 12 conducting vanes. The cross-section is parallel to the cavity axis. The white areas are the location of the conducting rods/vanes; a field solution is not included in the images as there is zero field inside the conductor. The outer edge of the images and white areas are the conducting boundaries. Red indicates higher field and blue indicates lower field with zero field at the boundaries. The dotted black lines depict the symmetries.

antenna locations that are not on symmetry points would produce a combined power given by Eq. 3-39. The TM_{010} mode does not need parity symmetry for this relation, and Eq. 3-39 is valid for combining any two TM_{010} signals coherently from the same endcap. Analytical predictions can estimate the power ratio of differing locations, are also used as part of the mode evaluation.

Higher-order modes can be assessed in a similar way. When signals are combined coherently, Eq. 3-39 dictates the power output. When signals are combined

180° out-of-phase, the power combines as

$$P_{12} \approx \frac{1}{2}(\sqrt{P_1} - \sqrt{P_2})^2, \quad (5-1)$$

where P_i is the power extracted in each antenna. Figure 5-2 shows images of the E_z field through a cross-section of a cylindrical cavity with two conducting tuning rods in a non-symmetric configuration for the (a) TM_{010} , (b) TM_{110} , (c) TM_{210} , and (d) TM_{020} . Two arbitrary antenna locations are depicted as black circles and labeled A and B.

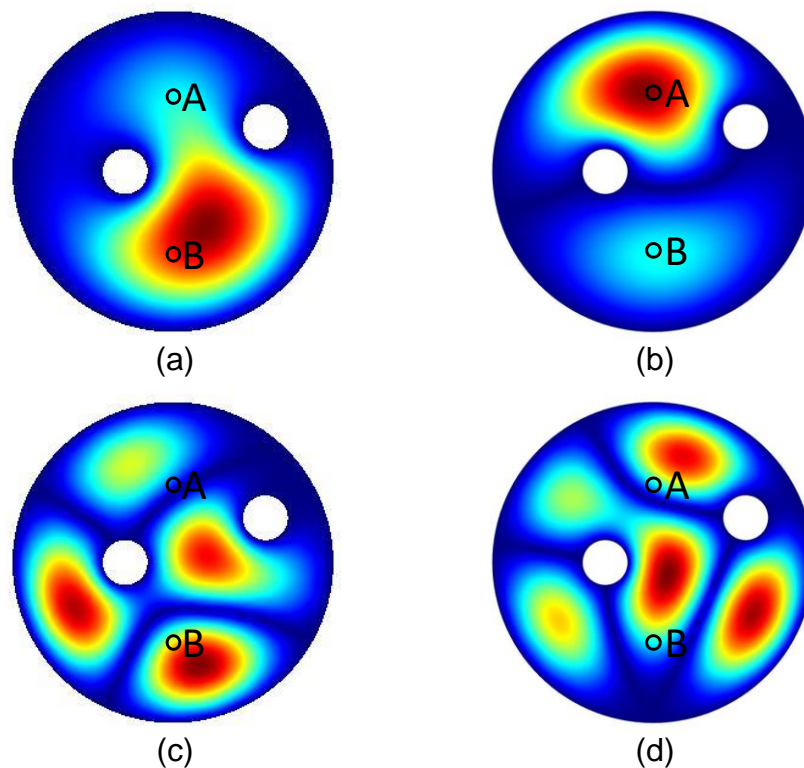


Figure 5-2. Cross-sectional images of the E_z field of various modes in cylindrical cavities with two non-symmetric, conducting tuning rods and two antenna locations. (a) TM_{010} . (b) TM_{110} . (c) TM_{210} . (d) TM_{020} . The cross-section is parallel to the cavity axis. The antennas are depicted as black circles. The white areas are the location of the conducting rods; a field solution is not included in the images as there is zero field inside the conductor. The outer edge of the images and white areas are the conducting boundaries. Red indicates higher field and blue indicates lower field with zero field at the boundaries.

Ratios of P_A/P_B can be estimated from the simulations as can the combining of the powers, assuming phase is maintained. Table 5-1 shows the predicted power-ratios, predicted relative phase, and predicted combined power of the modes in Fig. 5-1. The combined power is normalized by the maximum power from the individual antennas ($\max(P_A, P_B)$). The power is assumed to come from antennas on the same endcap and maintain phase through combining. The TM_{010} and TM_{210} signals would combine coherently while the TM_{110} and TM_{020} would combine destructively. The power-ratios of the TM_{110} and TM_{020} are distinct enough, that measurements could be used to distinguish them, but the power-ratios of the TM_{010} and TM_{210} are probably too close to discern the two modes conclusively.

Table 5-1. Predicted combined power variables of modes shown in Fig. 5-2.

Mode (Fig.)	Relative Phase (Φ)	$\sim P_A/P_B$	$\sim P_{AB}/\max(P_A, P_B)$
TM_{010} (a)	0°	0.5	1.5
TM_{110} (b)	180°	2.5	0.2
TM_{210} (c)	0°	0.3	1.2
TM_{020} (d)	180°	1.0	0.0

TE and TEM modes would not excite a weakly coupled probe antenna sufficiently to produce a signal that could be mistaken for a TM mode, but mixed (hybrid) modes could. The configurations of hybrid modes are much more challenging to predict, but, with a properly built cavity, accurate modeling should provide sufficient estimates to separate hybrid modes from TM modes using power combining and power ratio comparisons. However, testing is yet to confirm the method with mixed modes (see Chapter 5.2).

As observed during the 12-vane prototype testing, symmetry breaking can cause what appears to be one mode to resonate at differing frequencies in various locations in the cavity (see Chapter 4.4). The frequency shift will cause coherently combined power

to be reduced, given by Eq. 3-37. Comparing peak frequency measurements from the two antennas can predict the power loss. An alternative or augmenting method is to measure the phase directly. When the cavity geometry is reasonably simple, this approach may suffice without the combiners. But when the configuration is more complex or the mode density is high, power combining will likely be necessary for positive mode identification.

The configuration of the in-situ mode test is reasonably simple. Two weakly coupled antennas measure the peak power of a mode individually and combined. The individual measurements must go through the power combiner to account for insertion losses. Figure 5-3 shows a schematic of the test. The switches are arranged to measure the power from each antenna and the combined power. The power ratio and the normalized combine power are compared to predictions and pass-fail criteria are used to systematically determine the desired search mode.

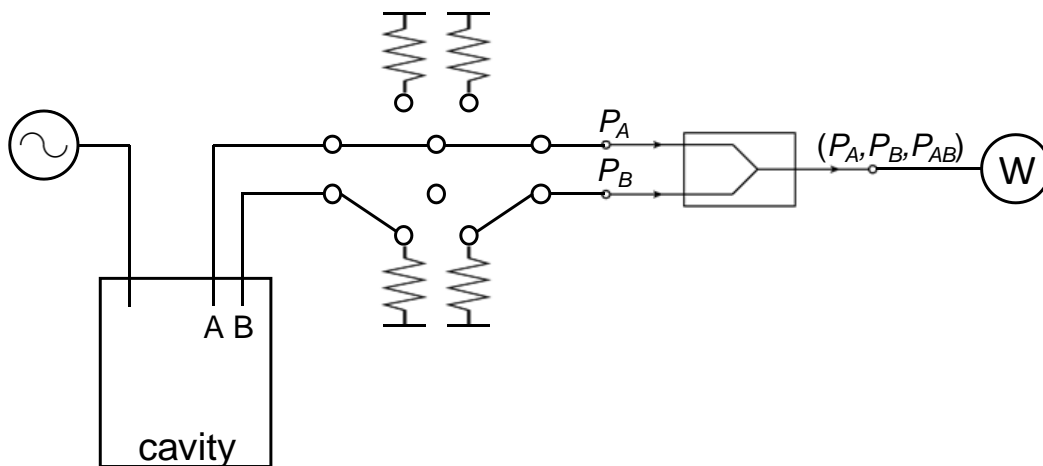


Figure 5-3. Schematic of in-situ mode test. The antennas are weakly coupled. The configuration shown is for measuring P_A ; changing the switch configuration enables measuring P_A , P_B , or P_{AB} . The power meter can be replaced by a network or spectrum analyzer. A phase-sensitive detector can also be added in parallel to the receiver chain.

Antenna pairs on the same endplate are used to determine the subscripts m and n , as demonstrated in Table 5-1. Multiple pairs will typically be needed to positively identify a search mode. The location of the antennas needs to be preplanned using analytical predictions to maximize mode identification throughout the cavity tuning range. Utilizing antenna pairs that are in line on opposite endcaps will reveal the parity (not to be confused with parity symmetry) of subscript p as even or odd.

Ideally, the test is conducted prior to use in a haloscope to calibrate the pass-fail algorithm for in-situ use. The precision of the measurement can be used to gauge the error bars for the criteria. The calibration will also verify the antenna configuration are adequate and provide evidence of positive mode identification.

5.2 Test Results

The in-situ mode test was assessed to varying degrees with four cavity configurations: an empty circular cylindrical cavity, a cylindrical cavity with two tuning rods, a cylindrical cavity with four tuning vanes, and the 12-vane prototype (see Chapter 4). The two-rod and empty cavities maintained longitudinal symmetry, while the 4-vane and 12-vane cavities did not. The experiments were used to prove the concept as well as gauge the applicability and technical challenges of implementation in haloscope detectors.

The four cavity configurations utilized the same boundary conditions. A stainless-steel tube of radius $R = 6.826$ cm and length of $L = 5R$ was electroplated with OFHC copper [115]. The endplates, rods, and vanes were made of solid OFHC copper. The components for the vane cavities were annealed (see Chapter 4.2). The endplates for the empty cavity were electropolished.

The empty cavity was used for the initial demonstration of the method. Four weakly coupled antennas were used in the testing. Two antennas were mounted 6.5 cm ($0.95R$) apart on the top-plate in the x - z plane of the cavity, identified as A and B. The other two antennas were mounted on the bottom-plate, identified as A' and B', in line with the first antennas with the letter same letter (without the prime) designation. Figure 5-4 is a reproduction of Fig. 3-1 with the top-plate antennas overlaid. The orientation of the TM_{110} mode is assumed, because the opposite polarized degeneracy, rotated 90° , will have the node in line with the antennas, due to small perturbations from the probes.

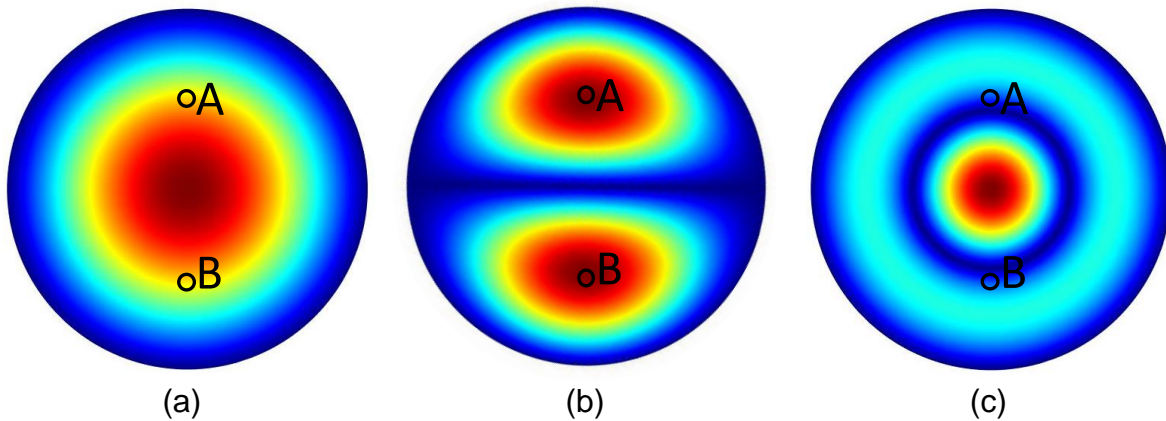


Figure 5-4. Cross-sectional images of the E_z field in an empty cylindrical cavity depicting the location of the top-plate in-situ mode test antennas. (a) TM_{010} . (b) TM_{110} . (c) TM_{020} . The cross-section is parallel to the cavity axis and the outer edge of the images are the conducting boundaries. The antennas are depicted as black circles. Red indicates higher field and blue indicates lower field with zero field at the outer boundaries.

The number of nodes between the antennas in (a) is zero, in (b) is one, and in (c) is two. From this, we can conclude that the power from antennas A and B will add coherently for the TM_{010} and TM_{020} , and destructively for the TM_{110} , when phase is maintained. Extending this over all TM modes in an empty cavity shows that coherent combining indicates an even value for the subscript m and destructive combining indicates an odd value. As stated above, the subscript p will be odd when the powers

from inline antennas combine coherently and even when they combine destructively (see Chapter 5.1).

The initial test only evaluated the ratio of the combined power to the independent power measurements, and did not use analytical predictions to compare P_A/P_B . The measurements include S_{12} of the top-plate antennas (A and B) combined and independent, and S_{12} of one top-plate (A) and one bottom-plate (A') combined and independent, for a total of six measurements. The power measurements were swept from 1.5 GHz to 4 GHz to capture the lowest 15 TM modes of the cavity. Antenna A' was used as the input antenna for the A, B, and AB power measurements, and antenna B was used for the A, A', and AA' power measurements.

The results were used to predict the parity of subscripts m and p . When $P_{AB} > \max(P_A, P_B)$, m is even, and $P_{AB} < \max(P_A, P_B)$, m is odd. Similarly, when $P_{AA'} > \max(P_A, P_{A'})$, p is odd, and $P_{AA'} < \max(P_A, P_{A'})$, p is even. A few modes were observed during the measurements to have a maximum power considerably lower in power than other modes. Those modes were removed from the algorithm and assumed to be TE modes.

Table 5-2 shows the results of the test compared to the predicted frequencies of the TM modes. The modes are ordered in ascending frequency. The predicted frequencies are from Eq. 3-16. The measured frequencies are from the modes not eliminated from the algorithm. The right two columns show the parity of the subscripts as determined by the algorithm. The frequency of the measured modes closely matched the predicted frequencies of the TM modes. The algorithm matched the parity of the m

Table 5-2. Results of the empty cavity in-situ mode test.

Mode	Predicted f_{mnp} (GHz)	Measured f (GHz)	Algorithm m	Algorithm p
TM ₀₁₀	1.6773	1.6783	even	even
TM ₀₁₁	1.7645	1.7651	even	odd
TM ₀₁₂	2.0035	2.0060	even	even
TM ₀₁₃	2.3483	2.3532	even	odd
TM ₁₁₀	2.6726	2.6752	odd	even
TM ₁₁₁	2.7282	2.7304	odd	odd
TM ₀₁₄	2.7596	2.7671	even	even
TM ₁₁₂	2.8885	2.8920	odd	even
TM ₁₁₃	3.1375	3.1430	odd	odd
TM ₀₁₅	3.2119	3.2220	even	odd
TM ₁₁₄	3.4561	3.4638	odd	even
TM ₂₁₀	3.5821	3.5861	even	even
TM ₂₁₁	3.6237	3.6276	even	odd
TM ₂₁₂	3.7459	3.7028	even	even
TM ₁₁₅	3.8269	3.8372	odd	odd

and p subscripts of every TM mode. As the test matched the subscripts for all predicted TM modes, the assumption that the modes with low power were TE modes is justified.

Figure 5-5 shows the S_{12} measurements using antennas A and B as outputs. The blue line shows the $S_{A'A}$, the purple line shows $S_{A'B}$, and the red line shows $S_{A'\{AB\}}$, where $\{AB\}$ indicates the combined signal from antennas A and B. The blue squares, purple diamonds, and red triangles depict P_A , P_B , and P_{AB} for each mode, respectively. Select modes are identified for visualization. The two low-power modes around 3 GHz are TE modes that were removed from the algorithm. The data can be traced back to the results shown in Table 5-2 for subscript m . The S_{12} measurement using antennas A and A' are not shown, but are similar in nature, yielding the results for subscript p . Equations 3-39 and 5-1 could predict P_{AB} to within ~20%, which was deemed acceptable for initial testing.

The in-situ mode test was conducted on a cylindrical cavity with two tuning rods. The rods ran the length of the cavity and attached to both endplates, maintaining

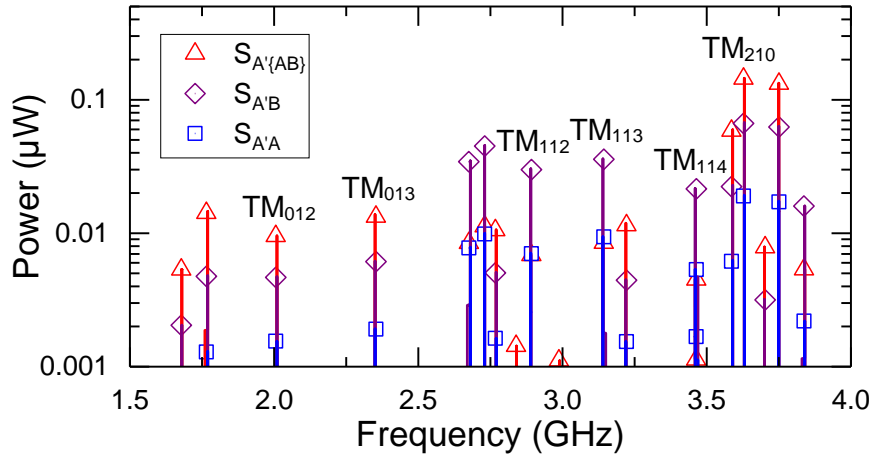


Figure 5-5. Power spectrum plots for the empty cavity in-situ mode test. Power is shown in μW on a log scale. S_{12} measurements are shown using antenna A' as the input antenna. $S_{A\{AB\}}$ indicates the output is the combined signal from antennas A and B. The blue square, purple diamond, and red triangle show the peak powers from antennas A, B, and {AB}, respectively, for each mode.

longitudinal symmetry. The rods' diameter was $d = 0.28R$. The rods were repositioned manually. Three weakly coupled probe antennas were used on each endcap for a total of six antennas. Two antennas were attached in line with the cavity axis on either endcap. The remaining four antennas were mounted in the y - z plane, with two on each endplate, spaced $1.15R$ apart.

Figure 5-6 shows images of the E_z field for the TM_{010} mode through a cross-section of the cavity in the three configurations tested with the top-plate antenna locations overlaid. The configurations are the (a) minimum TM_{010} frequency, (b) mid-range TM_{010} frequency, and (c) maximum frequency TM_{010} . The antennas are indicated by black circles and labeled A, B, and C. A prime is used to indicate the antennas inline on the bottom plate.

The test used several antenna combinations to identify the TM_{020} mode in the minimum and maximum TM_{010} frequency configurations. Figure 5-7 shows the S_{BA}

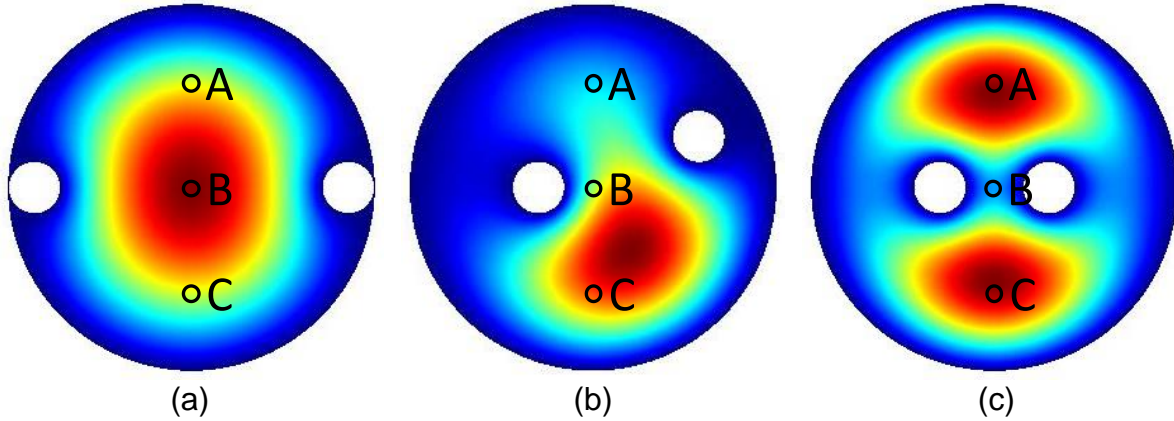


Figure 5-6. Cross-sectional images of the E_z field for the TM_{010} in a cylindrical cavity with two conducting tuning rods in the in-situ test configurations depicting the location of the top-plate antennas. (a) Minimum TM_{010} frequency configuration. (b) Mid-range TM_{010} frequency configuration. (c) Maximum TM_{010} frequency configuration. The cross-section is parallel to the cavity axis. The antennas are depicted as black circles. The white areas are the location of the conducting rods; a field solution is not included in the images as there is zero field inside the conductor. The outer edge of the images and white areas are the conducting boundaries. Red indicates higher field and blue indicates lower field with zero field at the boundaries.

spectrum in the minimum TM_{010} frequency configuration at around the predicted frequency range of the TM_{020} mode ($f_{020} = 4.269$ GHz). The three candidate modes are identified as TM_i from minimum to maximum frequency.

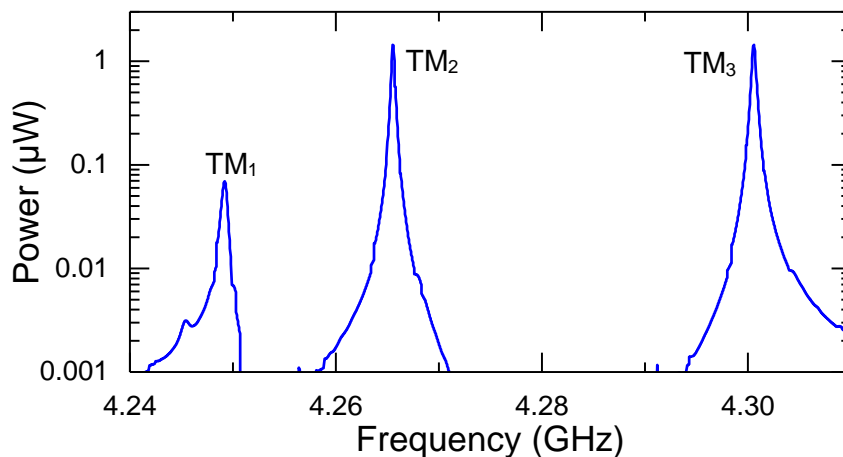


Figure 5-7. Power spectrum plots for the 2-rod cavity in-situ mode test in the minimum TM_{010} frequency configuration. Power is shown in μW on a log scale. S_{BA} measurements are shown.

For each configuration, three output antenna pairs were used to conduct the mode identification. The input antenna was varied based on the output pairs. The measurement sets were: S_{BA} , S_{BC} , $S_{B\{AC\}}$; $S_{B'A}$, $S_{B'B}$, $S_{B'\{AB\}}$; S_{AB} , $S_{AB'}$, $S_{A\{BB'\}}$. The first two sets were used to match the mode profile, and the third set determines the parity of ρ . The measurements were also made on the TM_{010} mode to adjust the predictions for systematic errors. The power ratio of the individual antennas and the power ratio of the combined power to maximum individual power were used to identify the TM_{020} .

Figure 5-8 shows images of the E_z field for the TM_{020} mode through a cross-section of the cavity in the (a) minimum and (b) maximum TM_{010} configurations with the top-plate antenna locations overlaid. The antennas are indicated by a black circle and labeled A, B, and C.

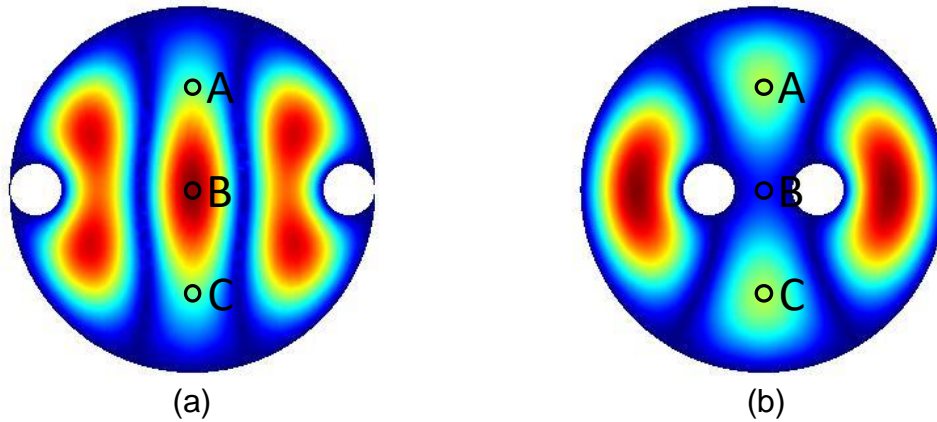


Figure 5-8. Cross-sectional images of the E_z field of the TM_{020} in a cylindrical cavity with two conducting tuning rods in the in-situ test configurations depicting the location of the top-plate antennas. (a) Minimum TM_{010} frequency configuration. (b) Maximum TM_{010} frequency configuration. The cross-section is parallel to the cavity axis. The antennas are depicted as black circles. The white areas are the location of the conducting rods; a field solution is not included in the images as there is zero field inside the conductor. The outer edge of the images and white areas are the conducting boundaries. Red indicates higher field and blue indicates lower field with zero field at the boundaries.

Table 5-3 shows the test results for the minimum TM₀₁₀ frequency configuration.

The measurement ratios are shown for the TM₀₁₀ and three candidate modes. Because the predicted power ratios for the TM₀₂₀ match the values for the TM₀₁₀, the measured values of the TM₀₁₀ are used as predicts for the TM₀₂₀ to account for systematic error.

Table 5-3. Results of the 2-rod cavity in-situ mode test in the minimum TM₀₁₀ frequency configuration.

Mode	P_A/P_C	$P_{AC}/\max(P_A, P_C)$	Predicted P_A/P_C	Predicted $P_{AC}/\max(P_A, P_C)$	Pass/Fail
TM ₀₁₀	0.59	2.41	1.0	2.0	N/A
TM ₁	4.03	2.49	0.59	2.4	F
TM ₂	0.52	2.77	0.59	2.4	P
TM ₃	0.61	2.34	0.59	2.4	P
	P_A/P_B	$P_{AB}/\max(P_A, P_B)$	Predicted P_A/P_B	Predicted $P_{AB}/\max(P_A, P_B)$	
TM ₀₁₀	0.34	2.20	0.6	1.5	N/A
TM ₁	0.90	4.74	0.34	2.2	F
TM ₂	0.22	2.43	0.34	2.2	P
TM ₃	0.21	1.99	0.34	2.2	P
	$P_B/P_{B'}$	$P_{BB'}/\max(P_B, P_{B'})$	Predicted $P_B/P_{B'}$	Predicted $P_{BB'}/\max(P_B, P_{B'})$	
TM ₀₁₀	0.29	0.14	1.0	0.0	N/A
TM ₁	0.34	3.39	0.29	0.14	F
TM ₂	0.41	0.15	0.29	0.14	P
TM ₃	0.36	2.04	0.29	0.14	F

TM₁ failed the criteria in the first two data sets, because the P_A/P_C and P_A/P_B measurements were more than triple the predicted values (i.e., the values measured for TM₀₁₀). TM₁ and TM₃ failed the criteria in the third set, because the $P_{BB'}/\max(P_B, P_{B'})$ measurements were more than triple the predicted values. TM₃ pass the criteria in all data sets as the measured ratio values were within a factor of three (above or below) of the predictions. Thus, the test conclude TM₂ was the TM₀₂₀ mode. TM₂ had a measured frequency of 4.265 GHz, almost exactly matching the analytical prediction. Based on the results, TM₃ was likely the TM₀₂₁, which has a predicted frequency of 4.304 GHz; the

measured frequency for TM_3 was 4.301 GHz. TM_1 had odd values for p , but the parity for m and n could not be established.

The pass/fail criterion was made broad to account for the error bars on the prediction values and large systematic error observed in the testing. For example, the ratio of P_A/P_C for the TM_{010} mode should be 1.0 but was measured at 0.59. The discrepancy could be due to inconsistencies in the combiner ports, attenuation in a receiver line, or longitudinal symmetry breaking in the cavity. An investigation into the source was not conducted, as the test consistently predicted the TM_{020} when the TM_{010} measurements were used for the predicted values.

The measured combined power for all the configurations was considerably higher than predicted by Eq. 3-39 and Eq. 5-1. This behavior was observed across all the in-situ mode testing of the 2-rod cavity. The discrepancy may have been due a loss in power at the terminations, but the cause of the difference was not investigated.

Table 5-4 shows the test results for the maximum TM_{010} frequency configuration. The configuration had four candidate modes for the TM_{020} . The measurement ratios are shown for the TM_{010} and the candidates. The measured values of the TM_{010} are used as predictors for the TM_{020} to account for systematic error like Table 5-3. A factor of three was used for the pass/fail criteria as well.

The test conclude TM_2 was the TM_{020} mode. TM_2 had a measured frequency of 4.009 GHz, almost exactly matching the analytical prediction of 4.012 GHz. The criterion for $P_{BB}/\max(P_B, P_{B'})$ was opened to a factor of 10 to account for the very low prediction value, but a factor of three would have yielded the same conclusion. Unlike the results in Table 5-3, where the third data set would have been sufficient to identify

Table 5-4. Results of the 2-rod cavity in-situ mode test in the maximum TM₀₁₀ frequency configuration.

Mode	P_A/P_C	$P_{AC}/\max(P_A, P_C)$	Predicted P_A/P_C	Predicted $P_{AC}/\max(P_A, P_C)$	Pass/Fail
TM ₀₁₀	0.53	3.87	1.0	2.0	N/A
TM ₁	0.18	4.63	0.53	3.9	F
TM ₂	0.51	3.05	0.53	3.9	P
TM ₃	0.44	3.11	0.53	3.9	P
TM ₄	0.54	3.42	0.53	3.9	P
	P_A/P_B	$P_{AB}/\max(P_A, P_B)$	Predicted P_A/P_B	Predicted $P_{AB}/\max(P_A, P_B)$	
TM ₀₁₀	13.64	1.55	4.0	1.6	N/A
TM ₁	3.17	0.17	14	1.6	F
TM ₂	22.54	1.70	14	1.6	P
TM ₃	0.10	0.46	14	1.6	F
TM ₄	15.98	1.71	14	1.6	P
	$P_B/P_{B'}$	$P_{BB'}/\max(P_B, P_{B'})$	Predicted $P_B/P_{B'}$	Predicted $P_{BB'}/\max(P_B, P_{B'})$	
TM ₀₁₀	1.35	0.01	1.0	0.0	N/A
TM ₁	1.66	0.10	1.4	0.01	P
TM ₂	1.10	0.02	1.4	0.01	P
TM ₃	1.28	0.01	1.4	0.01	P
TM ₄	1.51	3.53	1.4	0.01	F

the TM₀₂₀ mode, the second and third data sets are needed in Table 5-4. In general, the greater the number of candidates, the more data sets will be needed to detect a search mode.

Based on the results, TM₄ was likely the TM₀₂₁, which has a predicted frequency that exactly matches the measured value of 4.049 GHz. TM₁ had an even value for p , but the parity for m and n could not be established. TM₃ was discovered to be a TE mode that was not filtered out by the power threshold. The test method cannot be used to identify a TE mode with probe antennas.

The in-situ mode test positively identified the TM₀₂₀ mode in both 2-rod configurations tested. An additional check was conducted to verify the TM₀₁₀ mode in the mid-range frequency configuration (see Fig. 5-6(b)). Table 5-5 shows the results.

Table 5-5. Results of the 2-rod cavity in-situ mode test in the mid-range TM_{010} frequency configuration.

Output Antennas	P_1/P_2	$P_{12}/\max(P_1, P_2)$	Predicted P_1/P_2	Predicted $P_{12}/\max(P_1, P_2)$	Pass/Fail
A,C	0.19	1.68	0.5	1.5	P
A,B	0.44	2.51	0.6	1.6	P
B,B'	1.12	0.01	1.0	0.0	P

The measurements passed the pass/fail criteria of the algorithm identifying the mode as the TM_{010} . The measured frequency was 2.454 GHz and the predicted frequency is 2.458 GHz. The combined power was still considerably higher than predicted, particularly the measured value for the $S_{B\{AB\}}$ channel. The source of the discrepancy was not detected.

The in-situ mode test was conducted on the 4-vane cavity prototype (see Chapter 4.4) to verify that the powers combined as expected. Figure 5-9 shows the power spectrum of the 4-vane cavity for the S_{GE} , S_{GF} and $S_{G\{EF\}}$ channels (see Fig. 4-21). The power is in dBm. Select modes are labeled. The red line indicates the combined power P_{EF} , the peak of the red line is higher than the other channels only for the TM_{01p} modes. Thus, only the TM_{01p} mode signals combined constructively due to discrete transverse symmetry, as expected. Other antenna combinations were also tested yielding the same positive results.

Because the vanes were known to have some bend, longitudinal symmetry breaking existed in the cavity. The degeneracy breaking of the TM_{011} mode (second from the left) is distinctly depicted as two peaks conjoined, which is a direct result of longitudinal symmetry breaking. The 4-vane in-situ mode test demonstrated the mode identification method works with modest longitudinal symmetry breaking. But the extent

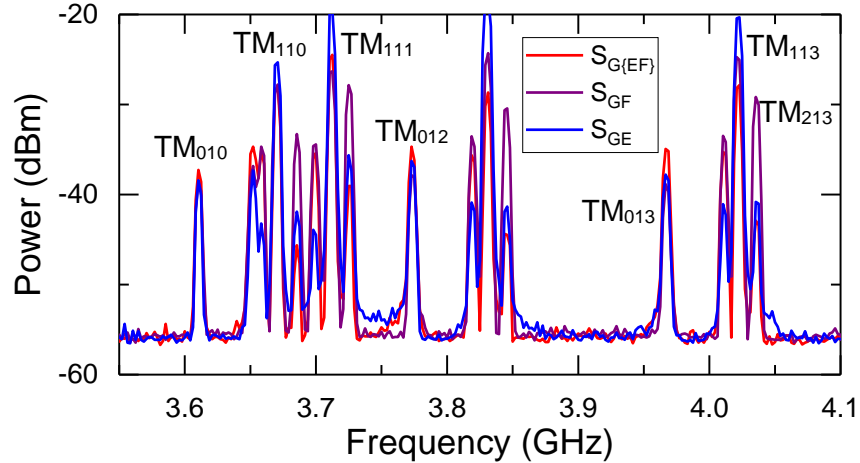


Figure 5-9. Power spectrum plot for the 4-vane cavity in-situ mode test. Power is shown in dBm. S_{12} measurements are shown using antenna G as the input antenna. $S_{A\{AB\}}$ indicates the output is the combined signal from antennas A and B. The blue square, purple diamond, and red triangle show the peak powers from antennas A, B, and $\{AB\}$, respectively, for each mode.

of allowable symmetry breaking is not known, since the test did not work on the 12-vane cavity prototype.

The mode test was conducted multiple times on the 12-vane prototype in an attempt to positively identify the TM_{010} mode. The test was conducted at room temperature in the maximum TM_{010} frequency configurations, in conjunction with course bead-pull and rod insertion tests (see Chapter 4.4). The in-situ test unfortunately eliminated all candidate modes, suggesting the TM_{010} mode was in some hybrid state in the test configuration.

The test was also run in LN_2 and L^4He on the third lowest TM mode with no success. The test used five antenna pair to measure the power ratios of TM_3 with the vane angles set at $\theta = 14.25$ (see Fig. 4-29 and Fig. 4-33). The measurements were compared to predictions for the TM_{010} . Equation 3-37 was also used to estimate the combined power with limited success. Table 5-6 shows the results from the LN_2 testing. The antenna labels are depicted on Fig. 4-4. Input lists the input antenna used and

Table 5-6. Results of the 12-vane prototype in-situ mode test.

Input	Output	P_1/P_2	Predicted P_1/P_2	$P_{12}/\max(P_1, P_2)$	Predicted $P_{12}/\max(P_1, P_2)$	Computed $P_{12}/\max(P_1, P_2)$
G	A,B	2.2	1.0	0.4	1.0	0.2
A	B,G	1.7	1.0	2.2	0.0	1.6
H	C,D	12.7	1.0	1.5	1.0	0.8
H	E,F	49.7	1.0	1.0	1.0	0.6
F	E,H	0.6	1.0	1.7	0.0	1.6

output list the output antennas that constitute the three channels use in each line of the table, with the first antenna list corresponding to subscript 1 and the second antenna corresponding to subscript 2.

The results suggest TM_3 is not the TM_{010} mode. Specifically, the $S_{A\{BG\}}$ and $S_{F\{EH\}}$ measurements showed coherent adding, signifying p has an odd value. The high values for P_1/P_2 indicate significant symmetry breaking. The cell with antennas D and F has an extremely weak field at the mode frequency. The computed P_{12} was less than the measured values in every channel, similar to the results seen in the other tests, suggesting an error in the test set-up. The error was not investigated further.

The in-situ mode tests showed the method has potential for identifying search modes in haloscope cavities. The test successfully identified parity of subscripts, could depict desired modes when no longitudinal symmetry was broken, and could assist in identifying the TM_{010} mode with modest symmetry breaking. However, the method was not able to identify the TM_{010} mode nor determine the subscripts of other TM modes in the 12-vane prototype, showing the method may have limited use in highly complex cavities without further development. The incorporation of a phase-sensitive detector could significantly improve the reliability of the testing.

CHAPTER 6 CONCLUSION

6.1 Future Work

The interest in searching for axion dark matter at masses above $\sim 4 \mu\text{eV}$ (~ 1 GHz) is growing tremendously in the science community. Every notable CDM axion experiment is currently researching techniques to conduct KSVZ-sensitive searches at higher masses. The advancement of tunable microwave cavities is a significant part of that effort.

The findings of the research presented herein furthers the progress of high-frequency axion detectors, but considerable more work must be done to elevate the search frequencies through the allowable mass-coupling phase space. Continuing the development of test methods and analysis techniques discussed above will be pivotal to successfully observing axion dark matter.

ADMX, HAYSTAC, and CAPP have a multitude of high-frequency cavity prototypes that are in various stages of fabrication and testing. Many of the lessons learned from the 12-vane cavity prototype yielded insight into potential issues and best practices for next-generation cavities. Additional analysis and testing of longitudinal symmetry breaking needs to be performed to better predict how the more complex cavities will be effected.

The correlation of the mechanical gap size (i.e., capacitive effect) and rod/vane misalignment to the frequency spectrum hole needs to be verified. A test cavity would provide an adjustable gap and/or tilt. Mode maps for varying gaps and tilt should be compared to the analytical predictions. The results will confirm the finding that longitudinal symmetry is the mechanism for mode repulsions. Further analysis would

look as surface currents, charge densities, and field lines in greater detail to better understand how their interaction alter the mode solutions.

Other symmetry breaking constructs should also be studied. The capacitive effect experience with tuning rod gaps will also be observed when the tuning rod passes through a slot in the endplates. However, the orientation of the resulting field lines is now transverse. How the change effects mode repulsions and mode mixing is not known. A deeper understanding of how the effects compare to tuning rod gaps in terms of holes in the frequency spectrum and losses in form factor is needed.

Additional analysis and testing of more nuanced discoveries must also to be conducted. The observation of mode decoupling should be modeled to verify cause is mode decoupling and provide predictability. A eigenfrequency simulation would provide such results. CAPP is investigating a multicell tuned cavity similar in fashion to the 12-vane prototype. Symmetry breaking between the cells is proposed to cause mode decoupling, resulting in each cell resonating at slightly differing frequencies. Verification of the mechanism with testing and correlation to modeling is necessary for the success of the design. Because the form factor is not measured, but is a critical value in the sensitivity of the detector, a high confidence in simulations is critical to detect CDM axions. Without justifying the simulation predictions of longitudinal symmetry breaking in complex cavities, the computed C will require high error bars.

The location of the input and output antennas have been shown to be nonnegligible, especially in periodic array cavities and for conducting in-situ mode testing. Additional studies need to focus solely on antenna placement and how losses between cells will affect axion signal absorption by the output antenna. A periodic array

prototype with multiple antenna ports could be built to observe the effects of varying input and output antenna on S_{12} measurements. Additionally, the perturbation effects of the output antenna on the mode configurations and form factors are not well known, and need further study. The location of the antenna will affect the penetration depth needed to critically couple to the mode.

The relationship between mode hybridization and longitudinal symmetry breaking is an area of study independent from axion searches. While hybridization in waveguides with inhomogeneous dielectric constants has been well explored, little is known about mode mixing in homogeneous conditions. Currently, no mode mixing has been observed between a TM mode and a non-degenerate TE mode. But insufficient evidence exists to postulate a theorem.

Understanding what causes some modes to mix and others not to mix could uncover new discoveries in waveguide and resonant cavities, as well as greatly enhance haloscope cavity development. The mechanism for mode mixing in cavities with homogeneous permittivity should be explored using various numerical analysis techniques to ensure consistent conclusions. Analytical expansion of the effects into particle accelerators, reentrant cavities, and microstrip resonators could open unknown potential.

Select FEM simulations have suggested that mode hybridization breaks the orthogonality condition of Eq. 3-17. During mode repulsions, the orthogonality condition appears to be violated in proportion to the strength of the repulsion. The orthogonality condition is maintained for the non-mixing broken degenerate TE mode. However, the results are not well vetted and seem to violate boundary conditions. Further study to

determine if this is a real phenomenon or a construct of numerical simulation is required.

Longitudinal symmetry breaking introduces evanescent modes to the observed frequency range. It is unknown if evanescent mode mix with other modes or are detectable with probe antennas. Further understanding of how these modes interact with conventional and reentrant modes and effect haloscope measurements is needed.

Findings of simulations should be confirmed with testing. Cavities with intentional symmetry breaking could be used to demonstrate mode hybridization. Such tests should be accompanied by bead-pull tests to clearly depict mode mixing. The effects of changing boundary conditions (e.g., mechanical gaps, rod tilt) should be quantified in terms of symmetry breaking and mixing parameters.

Mode identification methods are being advanced by many current haloscope experiments. In particular, HAYSTAC has made significant progress in utilizing bead-pull tests to characterize microwave cavities. Successfully implementing bead-pull testing will be critical in CDM axion detection as search frequencies continue to increase, and axion collaborations are beginning to incorporate the process into the cavity production flow. Rod insertion should also be reviewed as a tool for mode identification, especially for detectors with a separate vernier tuning device, such as HAYSTAC.

The in-situ mode test will be necessary to conduct searches with higher-order modes. The validation testing showed the method has potential for mode identification during data-taking runs. However, significant mode hybridization may plague the

method and issues need to be flushed out with additional testing. Conducting the test with varying symmetry breaking will expose the limits of the method.

Custom combiners should be used to minimize insertion losses when only one antenna signal is measured. The cause for the inconsistencies between predicted and measured combined power during testing (see Chapter 5.2) must be determined. Establishing the proper termination for the combiner ports is critical to verifying the power readings match predictions and can be repeatedly used for mode confirmation. The method should be tested with a network analyzer and phase-sensitive detector to improve reliability. Combining the bead-pull characterization with in-situ mode testing, prior to data-taking, will yield a powerful tool in ensuring the proper mode is tracked.

The antennal-location testing and in-situ mode testing could be performed in conjunction, as the test set-ups are essentially identical and the results are interconnected. Changing the location of the antennas alter the effectiveness of the mode test and the detection sensitivity. Periodic array cavities are particularly sensitive to symmetry breaking, both discrete transverse and longitudinal. Such cavities require a comprehensive understanding of how antenna locations translate into more repeatable mode identification and tracking.

Finally, the superconducting thin-film hybrid cavities have significant potential to increase the sensitivity of a detector. Most of the power loss in the cavity is through the surfaces that are oriented parallel to \mathbf{B}_0 . Eliminating those losses could boost Q_L by an order of magnitude or more. The gains are greatest in periodic array cavities which use many tuning rods, and thus have more longitudinal surfaces to dissipate energy. With the possible reduction in form factor and cell-coupling due to even modest symmetry

breaking, superconducting hybrids may be the only way to recover the losses in sensitivity.

Unfortunately, superconducting hybrids have proven to be tremendously challenging. Various thin-film coating techniques have been tested by HAYSTC, but have yield only modest progress in the last ~5 years. The collaboration has a homogeneous ~8 T magnet with a radial field of < 0.005 T developed specifically for testing superconducting hybrid cavities. However, no testing has been performed to date due to a lack of a test cavity.

Recent analyses have shown that a substrate with thickness comparable to the wavelength is required to maintain high reflectivity at the superconducting boundaries. But limited simulations have been conducted. The effects of flux penetrations on Q of hybrids was only briefly examined in this study, and a much more comprehensive investigation is warranted. But, until coating techniques are successful, testing the findings of such analyses will be impossible.

6.2 Summary

The detection of axion dark matter is of great interest to the physics community. While ADMX has successfully excluded CDM axions up to $\sim 4 \mu\text{eV}$ (~ 1 GHz) at KSVZ sensitivity, and is currently probing to the DFSZ model coupling at about the same mass range, no search has successfully achieved KSVZ sensitivity above 1 GHz. In order to observe axion dark matter at such masses, detector technologies must continue to advance. Developing microwave cavities with sufficient tuning range and detection parameters is the most critical component.

The findings of the study detailed within continue the march toward axion detection. The investigation uncovered intricacies of symmetry breaking not previously

known and revealed lesser realized challenges of complex microwave cavities such as periodic arrays. Several discoveries provide critical information to researchers as haloscope cavities evolve toward higher frequencies.

Most notably, uncovering that the mechanism for mode repulsion is longitudinal symmetry breaking enables cavity developments a point of entry for mitigating the problem. Longitudinal symmetry breaking was previously known to cause mode localization and degrade form factor [15], and mode repulsion has been documented before [100,101,107]. But the precise mechanism for mode repulsion had not been determined prior.

The results of the study strongly suggest that mode repulsion is due to mode mixing, which is directly caused by longitudinal symmetry breaking within the cavity. Cavities with no or little symmetry breaking demonstrated no mode mixing while cavities with considerable symmetry breaking were riddled with mode repulsions and hybrid modes. The finding was supported by simulations, power spectrum measurements, mode maps, and in-situ mode testing. Further, simulations showed a clear correlation between the amount of symmetry breaking and the strength of the mode repulsion, quantified by the hole size in the frequency search spectrum.

Longitudinal symmetry breaking was also discovered to be a source of mode crowding. Numerical simulations uncovered the finding, which was substantiated by experimentation. The revelation that, during a mode repulsion, only one broken degenerate TE mode mixes with a TM mode while the other remains pure was also new, leaving open the question of why to future studies.

While the 12-vane prototype testing failed to demonstrate conclusively the concept's feasibility for haloscope detectors, the testing yielded significant insight which supported the simulation results and revealed key aspects of periodic array cavities. The experiment demonstrated the first mode tuning with conducting vanes in room and cryogenic temperatures. The testing also displayed cell decoupling of modes, for which no previous documentation was found.

The extreme sensitivity of periodic arrays to longitudinal symmetry breaking could only have been realized through prototype testing. The unexpectedly large mode density in measurements and simulations showed the tremendous impact the capacitance effect has on mode crowding, with evanescent, reentrant, and broken degenerate modes filling the previously empty frequency space. And only through measurements did the need for more robust mode detection methods come to light.

The demonstration of the in-situ mode test is also significant for high-frequency haloscope detectors. ADMX had already experienced trouble tracking higher-order TM modes for axion searches. The need for mode identification techniques during data-taking is only going to grow as frequency ranges move up. The in-situ mode test conceived and proven in this study provides a noninvasive method of mode identification. The test demonstrated the capability of depicting a search mode out of select candidates and partially identifying multiple modes in various cavity configurations. Improving the instrumentation and components of the test could produce a robust tool for high-frequency axion searches.

Additionally, this research provided further guidance into tunable high-frequency cavities. Establishing quantifiable differences between cavity concepts that could be

used to establish a normalized figure-of-merit will help steer development programs in the field. The first-order approximation of the effects of flux penetrations on superconducting thin-film hybrid cavities can open the door to more complex simulations and can be validated with experimentation in the foreseeable future.

While the original intent of the investigation, to prove the feasibility of periodic array cavities for haloscope cavities, was not fully achieved, significant progress towards next-generation axion dark matter detectors at higher frequencies was obtained. The findings herein will continue the community march towards observation of the axion particle.

LIST OF REFERENCES

- [1] S. Weinberg, Phys. Rev. Lett. **40**, 223 (1978).
- [2] F. Wilczek, Phys. Rev. Lett. **40**, 279 (1978).
- [3] R. Peccei and H. Quinn, Phys. Rev. Lett. **38**, 1440 (1977).
- [4] J. Ipser and P. Sikivie, Phys. Rev. Lett. **50**, 925 (1983).
- [5] C. Patrignani *et al.* (Particle Data Group), Chin. Phys. C **40**, 100001 (2016).
- [6] A. Arvanitaki, S. Dimopoulos, S. Dubovsky, N. Kaloper and J. March-Russell, Phys. Rev. D **81**, 123530 (2010).
- [7] P. Sikivie, Phys. Rev. Lett. **51**, 1415 (1983).
- [8] H. Primakoff, Phys. Rev. **81**, 899 (1951).
- [9] M. Arik *et al.* (CAST Collaboration), Phys. Rev. Lett. **107**, 261302 (2011).
- [10] P. Sikivie, Phys. Rev. D **32**, 2988 (1985).
- [11] J. Preskill, M.B. Wise and F. Wilczek, Phys. Lett. B **120**, 127 (1983).
- [12] L. Abbott and P. Sikivie, Phys. Lett. B **120**, 133 (1983).
- [13] M. Dine and W. Fischler, Phys. Lett. B **120**, 137 (1983).
- [14] M. S. Turner, Phys. Rep. **197**, 67 (1990).
- [15] C. Hagmann, P. Sikivie, N. S. Sullivan, D. B. Tanner and S. I. Cho, Rev. Sci. Instrum. **61**, 1076 (1990).
- [16] I. Stern, A. A. Chisholm, J. Hoskins, P. Sikivie, N. S. Sullivan, D. B. Tanner, G. Carosi and K. van Bibber, Rev. Sci. Instrum. **86**, 123305 (2015).
- [17] J. E. Kim, Phys. Rept. **150**, 1 (1987).
- [18] S. L. Adler, Phys. Rev. **177**, 2426 (1969).
- [19] R. Jackiw and C. Rebbi, Phys. Rev. Lett. **37**, 172 (1976).
- [20] G. 't Hooft, Phys. Rev. D **14**, 3432 (1976).
- [21] V. Baluni, Phys. Rev. D **19**, 2227 (1979).
- [22] E. P. Shabalin, Sov. Phys. Usp. **26**, 297 (1983).

- [23] J. M. Pendlebury *et al.*, Phys. Rev. D **92**, 092003 (2015).
- [24] C. A. Baker *et al.*, Phys. Rev. Lett. **97**, 131801 (2006).
- [25] J. D. Bjorken *et al.*, Phys. Rev. D. **38**, 3375 (1988).
- [26] J. E. Kim, Phys. Rev. Lett. **43**, 103 (1979).
- [27] M. A. Shifman, A. I. Vainshtein and V. I. Zakharov, Nucl. Phys. B **166**, 493 (1980).
- [28] R. Zhitnitsky, Sov. J. Nucl. Phys. **31**, 260 (1980).
- [29] M. Dine, W. Fischler and M. Srednicki, Phys. Lett. B **104**, 199 (1981).
- [30] F. Zwicky, Helv. Phys. Acta **6**, 110 (1933).
- [31] F. Zwicky, Astrophys. J. **86**, 217 (1937).
- [32] Image provided by National Optical Astronomy Observatory website (https://www.noao.edu/image_gallery/html/im0549.html); image credit O. Lopez-Cruz and I. Shelton/NOAO/AURA/NSF.
- [33] Image provided by National Aeronautics and Space Administration, Goddard Space Flight Center website (<https://asd.gsfc.nasa.gov/blueshift/index.php/2011/10/17/blog-a-fond-farewell-to-rosat/>); image credit ROSAT/MPE/S. L. Snowden.
- [34] V. C. Rubin, W. K. J. Ford and N. Thonnard, Astrophys. J., **238**, 471 (1980).
- [35] E. Corbelli and P. Salucci, Mon. Not. R. Astron. Soc. **311**, 441 (2000).
- [36] Image courtesy of R. Lang, Purdue University; image credit E. Corbelli and P. Salucci/DSS POSS-II.
- [37] Image provided by Pearson Education Inc., publishing as Addison-Wesley (2004).
- [38] J. P. Kneib and P. Natarajan, Astron. Astrophys. Rev. **19**, 47 (2011).
- [39] C. Heymans *et al.*, Mon. Not. R. Astron. Soc. **427**, 146 (2012).
- [40] H. Y. Shan *et al.*, Astrophys. J. **748**, 56 (2012).
- [41] H. M. Abdelsalam, P. Saha and L. L. R. Williams, Astrophys. J. **116**, 1541 (1998).
- [42] Image provided by National Aeronautics and Space Administration website (<https://apod.nasa.gov/apod/ap011007.html>); image credit STScI/WFPC2/HST/NASA.

- [43] C. L. Sarazin, “The Physics of Cluster Mergers”, in *Merging Processes in Galaxy Clusters*, Astrophysics and Space Science Library **272**, edited by L. Feretti, I.M. Gioia and G. Giovannini, (Springer Netherlands, 2002), Chapter 1, pp. 1-38.
- [44] S. M. Molnar, *Front. Astron. Space Sci.* **2**, 7 (2016).
- [45] D. Clowe, A. Gonzalez and M. Markevitch, *Astro. Phys. J.* **604**, 596 (2004).
- [46] Image courtesy of R. Lang, Purdue University; image credit Chandra/D. Clowe *et al.*
- [47] L. Kawano, D. Schramm, and G. Steigman, *Astro. Phys. J.* **327**, 750 (1988).
- [48] G. Steigman, *Annu. Rev. Nucl. Part. Sci.* **57**, 463 (2007).
- [49] Image courtesy of R. Lang, Purdue University; image credit G. Steigman.
- [50] P. A. R. Ade *et al.* (Planck Collaboration), *Astron. Astrophys.* **571**, A16 (2014).
- [51] Image courtesy of R. Lang, Purdue University; Image credit Planck Collaboration.
- [52] V. Springel, C. S. Frenk and S. D. M. White, *Nature* **440**, 1137 (2006).
- [53] Image courtesy of R. Lang, Purdue University.
- [54] Z. Huang, J. R. Bond and L. Kofman, *Astrophys. J.* **726**, 64 (2011).
- [55] C. S. Frenk, and S. D. M. White, *Ann. Phys.* **524**, 507 (2012).
- [56] E. Kolb and M. Turner, *The Early Universe (Frontiers in Physics)* (Westview Press, 1990).
- [57] Image courtesy of T. M. P. Tait, University of California Irvine.
- [58] D. S. Akerib *et al.* (LUX Collaboration), *Phys. Rev. Lett.* **118**, 021303 (2017).
- [59] ATLAS Collaboration, “ATLAS releases new results in search for weakly-interacting supersymmetric particles”, Physics Briefing (May 2017), internet document (<http://atlas.cern/updates/physics-briefing/atlas-releases-new-results-search-weakly-interacting-supersymmetric>).
- [60] P. Sikivie, *Phys. Lett. B* **695**, 22 (2011).
- [61] A. Arvanitaki, S. Dimopoulos, S. Dubovsky, N. Kaloper, and J. March-Russell, *Phys. Rev. D* **81**, 123530 (2010).
- [62] L. D. Duffy and P. Sikivie, *Phys. Rev. D* **78**, 063508 (2008).
- [63] J. E. Kim and G. Carosi, *Rev. Mod. Phys.* **82**, 557 (2010).

- [64] L. D. Duffy *et al.*, Phys. Rev. D **74**, 012006 (2006).
- [65] I. Stern (on behalf of ADMX), in proceeding of “38th International Conference on High Energy Physics”, Proc. Sci. ICHEP2016, 198 (2017).
- [66] M. Arik *et al.* (CAST Collaboration), Phys. Rev. D **92**, 021101(R) (2015).
- [67] B. M. Brubaker *et al.*, Phys. Rev. Lett. **118**, 061302 (2017).
- [68] Image courtesy of ADMX.
- [69] P. W. Graham, I. G. Irastorza, S. K. Lamoreaux, A. Lindner and K. A. van Bibber, Ann. Rev. Nucl. Part. Sci. **65**, 485 (2015).
- [70] P. W. Graham and S. Rajendran, Phys. Rev. D **88**,035023 (2013).
- [71] P. Sikivie, N. Sullivan and D.B. Tanner, Phys. Rev. Lett. **112**, 131301 (2014).
- [72] G. Rybka *et al.*, Phys. Rev. D **91**, 011701(R).
- [73] Image reproduced from [101].
- [74] R. H. Dicke, Rev. Sci. Instrum. **17**, 268 (1946).
- [75] L. Krauss, J. Moody, F. Wilczek, and D. E. Morris, Phys. Rev. Lett. **55**, 1797 (1985).
- [76] J. V. Sloan *et al.*, Phys. Dark Univ. **14**, 95 (2016).
- [77] J. Hoskins *et al.*, Phys. Rev. D **94**, 082001 (2016).
- [78] Image reproduced from [106].
- [79] C. Hagmann *et al.*, Phys. Rev. Lett. **80** 2043 (1998).
- [80] S. Asztalos *et al.*, Astrophys. J. **571** L27 (2002).
- [81] S. J. Asztalos *et al.*, Phys. Rev. Lett. **104** 041301 (2010).
- [82] J. Hoskins *et al.*, Phys. Rev. D **84** 121302(R) (2011).
- [83] J. Jackson, *Classical Electrodynamics*, Third Edition (John Wiley & Sons, 1999) p.363-374.
- [84] S. A. Schelkunoff, *Electromagnetic Waves*, Tenth Reprint (D Van Nostrand Co, New York, USA, 1960) p.390-391.
- [85] H. Zucker and G. I. Cohn, IRE Trans. Microwave Theory Tech. **10**, 202 (1962).

- [86] A. S. Omar and K. F. Schunemann, IEEE Trans. Microwave Theory Tech. **35**, 268 (1987).
- [87] P. J. B. Clarricoats and B. C. Taylor, Proc. Inst. Elec. Eng. **111**, 1951 (1964).
- [88] K. A. Zaki, A. E. Atia, IEEE Trans. Microwave Theory Tech. **31**, 1039 (1983).
- [89] R. E. Collin, *Field Theory of Guided Waves*, Second edition (IEEE Press, New York, USA, 1991) p.416-417.
- [90] K. A. Zaki, S. Chen and C. Chen, IEEE Trans. Microwave Theory Tech. **36**, 1804 (1988).
- [91] J. H. A. Ragheb, A. Sebak and L. Shafai, IEE Proc. Microwaves Antennas Propag. **144**, 7 (1997).
- [92] D. M. Pozar, *Microwave Engineering*, Fourth Edition (John Wiley & Sons, 2012), p.309-311.
- [93] A.B. Pippard, Proc. R. Soc. London, Ser. A **191**, 385 (1947).
- [94] F. Wooten, *Optical Properties of Solids* (Academic Press, New York, USA, 1972), p.94-97.
- [95] A. Vishen, G.P. Srivastava, G.S. Singh and F. Gardiol, IEEE Trans. Microwave Theory Tech. **34**, 292 (1986).
- [96] COMSOL AB, Tegnérgatan 23 SE-111 40 Stockholm, Sweden.
- [97] G. Cardone, T. Durante, and S. A. Nazarov, SIAM J. Math. Anal. **42**, 2581 (2010).
- [98] A. Wexler, IEEE Trans. Microwave Theory Tech. **15**, 508 (1967).
- [99] W. C. Chew, *Waves and Fields in Inhomogeneous Media*, (John Wiley & Sons, 1999), p.411-441.
- [100] D. Lyapustin, An improved low-temperature RF-cavity search for dark-matter axions, Ph.D. Thesis, Univ. of Wash., Seattle WA (2015).
- [101] C. Hagmann, A search for cosmic axions, Ph.D. Thesis, Univ. of Flor., Gainesville FL (1990).
- [102] Image reproduced from [100].
- [103] H. Hahn and H.J. Halama, IEEE Trans. Microwave Theory Tech. **16**, 20 (1968).
- [104] S. Al Kenany *et al.*, Nucl. Instrum. Methods A **854**, 11 (2017).
- [105] G. Carosi, private communication, 2014.

- [106] J. Hoskins, A modulation sensitive search for non-virialized axions in the milky way halo, Ph.D. Thesis, Univ. of Flor., Gainesville FL (2014).
- [107] D. Kinion, First results from a multi-microwave-cavity search for dark-matter axions, Ph.D. Thesis, Univ. of Cal. Davis, Davis, CA (2001).
- [108] C. Boutan, A piezoelectrically tuned rf-cavity search for dark matter axions Ph.D. Thesis, Univ. of Wash., Seattle, WA (2017).
- [109] H. Kamerlingh Onnes, Comm.-Leiden, **120b** (1911).
- [110] J. Bardeen, L. N. Cooper, and J. R. Schrieffer, Phys. Rev. **106**, 162 (1957).
- [111] M. Tinkham, *Introduction to Superconductivity*, Second Edition, (McGraw-Hill Book Co., 1996), p.1-13.
- [112] X. Xi *et al.*, Phys. Rev. Lett. **105** (2010) 257006.
- [113] T.M. Shokair *et al.*, Int. J. Mod. Phys. A **29**, 1443004 (2014).
- [114] X. Xi, Conventional and time-resolved spectroscopy of magnetic properties of superconducting thin films, Ph.D. Thesis, Univ. of Flor., Gainesville FL (2011).
- [115] Performed by Seminole Metal Finishing, Inc., 967 Explorer Cove Altamonte Springs, FL 32701-7516, USA.
- [116] J. T. Rogers, Limits on the electromagnetic coupling and density of galactic axions, Ph.D. Thesis, The University of Rochester, Rochester, New York, (1967).
- [117] Supplied by Electro-Glo Distribution, Inc., P.O. Box 596, Princeton, IL 61356, USA.
- [118] J. Edwards, J. Electrochem. Soc. **100**, 223C (1953).
- [119] E. J. Casey, R. E. Bergeron, Can. J. Chem. **31**, 422 (1953).
- [120] H. Peng *et al.*, Nucl. Instrum. Methods A **444**, 569 (2000).
- [121] J. D. Verhoeven, *Fundamentals of Physical Metallurgy*, First Edition (John Wiley & Sons, New York, USA, 1975), p.329-334.
- [122] Supplied by Superior Electric, now operated Kollmorgen, 203A West Rock Road, Radford, VA 24141 USA.
- [123] Supplied by Cross Nail Laminates & Plastics, PO BOX 171, Shippensburg, PA 17257 USA.
- [124] Supplied by WM Berg, 5138 S. International Drive, Cudahy, WI 53110 USA.
- [125] Supplied by Microstock, Inc., P.O. Box 91, West Point, PA 19486-0091 USA.

[126] Supplied by Pasternack Enterprises, Inc., 17802 Fitch, Irvine, CA 92614 USA.

[127] Supplied by Stanford Research Systems Inc., 1290-D Reamwood Ave.,
Sunnyvale, CA 94089 USA.

[128] Supplied by Hewlett-Packard Company, now operated as Keysight Technologies
1400 Fountain Grove Pkwy., Santa Rosa, CA 95403-1799 USA.

[129] National Instruments Corporation, 11500 Mopac Expwy., Austin, TX, 78759-3504
USA.

[130] Supplied by Advantest America, Inc., 3061 Zanker Rd., San Jose, CA 95134 USA.

[131] H. E. Johns and J. O. Wilhelm, Can. J. Res. A **15**, 101 (1973).

[132] M. H. Edwards, Can. J. Res. **34**, 898 (1956).

BIOGRAPHICAL SKETCH

Ian P. Stern was awarded a US army commission at the New Mexico Military Institute at age 19. After earning a B.S. degree in aerospace engineering from Embry-Riddle Aeronautical University, he served three years on active duty as an infantry officer. He earned a M.S. degree in mechanical engineering from the University of Florida while serving as an Officer Candidate School instructor in the Florida National Guard. Prior to his Ph.D. pursuit, he worked in the space industry, developing deployable systems for satellites with Harris Corp. and Lockheed Martin Space System Co.